UCLA
UCLA Electronic Theses and Dissertations

Title

Freeze-thaw Damage of Hybrid Fiber-reinforced Concrete Containing Microencapsulated Phase Change Material

Permalink

Author

Chang, Tien-Shu

Publication Date

2021

Peer reviewed|Thesis/dissertation

UNIVERSITY OF CALIFORNIA

Los Angeles

Freeze-thaw Damage of Hybrid Fiber-reinforced Concrete Containing Microencapsulated

Phase Change Material

A dissertation submitted in partial satisfaction of the

requirements for the degree of Doctor of Philosophy

in Civil Engineering

by

Tien-Shu Chang

2021

ABSTRACT OF THE DISSERTATION

Freeze-thaw Damage of Hybrid Fiber-reinforced Concrete Containing Microencapsulated

Phase Change Material

by

Tien-Shu Chang

Doctor of Philosophy in Civil Engineering

University of California, Los Angeles, 2021

Professor Jiann-Wen Ju, Chair

This research is developed to investigate the influences of added phase change material (PCM) microcapsules on the freeze-thaw durability, the compressive behaviors, and the flexural behaviors of hybrid fiber-reinforced concrete. The concrete mix proportions are designed with the PCM volume fraction varying from 0 to 9%. The hybrid fiber, inclusive of steel fibers and polyvinyl alcohol microfibers, is added in a constant dosage of 1.1% by volume. Mechanical performance of the concrete is evaluated by performing uniaxial compression tests and three-point bending tests. Subsequently, the concrete specimens are weathered with a tailor-make freeze-thaw machine in a controlled environment. After the freeze-thaw cycles, the compressive strength, modulus of elasticity, fracture energy, equivalent flexural tensile strength, and residual flexural tensile strength are determined for each mixture design and compared with the values determined prior to the

cycles for the evaluation of freeze-thaw damage. The internal damage extent of concrete is monitored by ultrasonic pulse velocity tests over the freeze-thaw cycles. The experimental results show that the mechanical performance is considerably improved with the added hybrid fiber. The improvement on the compressive strength sufficiently compensates for the strength loss due to the incorporated PCM microcapsules; the additions of the hybrid fiber and the PCM contribute to different aspects of freeze-thaw durability (i.e., internally or superficially), at least to a different degree. A novel damage model, considering the beneficial and detrimental effects of adding PCM, is proposed to quantitatively describe damage extents observed in the experimental results. From this model, the optimized dosage of PCM is provided for hybrid fiber-reinforced concrete subjected to severe freeze-thaw cycles.

The dissertation of Tien-Shu Chang is approved.

Mathieu Bauchy

Ertugrul Taciroglu

Jenn-Ming Yang

Jiann-Wen Ju, Committee Chair

University of California, Los Angeles

2021

TABLE OF CONTENTS

LIST OF FIGURES

xiv

LIST OF TABELS

ACKNOWLEDGEMENTS

I would like to express my deepest gratitude to Professor Jiann-Wen Ju, my Ph.D. faculty advisor and my Ph.D. committee chair, for his inspiration, guidance and supports during the entirety of my graduate studies at UCLA. This dissertation is shaped by his invaluable and insightful advice.

I am grateful to the members in my doctorate committee: Professor Mathieu Bauchy, Professor Ertugrul Taciroglu, and Professor Jenn-Ming Yang. I would like to thank Professor Bauchy for his valuable discussion on the crystallization pressure; Professor Taciroglu for his structural damping project guidance; Professor Yang for his immerse inputs on my final defense presentation.

I am also grateful to my lab colleagues, Dr. Yinghui Zhu, Dr. Hao Zhang, Aiqing Xu, Xiaoyan Man, Jingxi Qin, Wenli Zhu, and Hang Su.

Lastly, I would like to thank my parents, my grandmother, my sister, and my wife for their generous supports and devotion.

VITA

2007-2011	B.S., Department of Civil Engineering
	National Cheng Kung University, Tainan, Taiwan
2011-2013	M.S., Department of Civil Engineering
	National Cheng Kung University, Tainan, Taiwan
2017-2021	Graduate Student Researcher and Teaching Fellow
	Civil and Environmental Engineering Department
	University of California, Los Angeles

PUBLICATIONS

1. Tien-Shu Chang and Jiann-Wen Woody Ju, "Investigations into the freeze-thaw damage and the compressive behavior of hybrid fiber-reinforced concrete containing microencapsulated phase change material", *Construction and Building Materials*, prepared for submission.

2. Kaihang Han, Jiann-Wen Woody Ju, Yinghui Zhu, Hao Zhang, Tien-Shu Chang and Zhengyao Wang, "Mechanical responses of microencapsulated self-healing cementitious composites under compressive loading based on a micromechanical damage-healing model", *International Journal of Damage Mechanics*, April 28, 2021.

3. Kaihang Han, Jiann-Wen Woody Ju, Hao Zhang, Yinghui Zhu, Tien-Shu Chang and Zhengyao Wang, "Mechanical response analysis of self-healing cementitious composites with microcapsules subjected to tensile loading based on a micromechanical damage-healing model", *Construction and Building Materials*, Vol. 280, April 19, 2021.

4. Yun-Che Wang, Chih-Chin Ko and Tien-Shu Chang, "Sensing mechanical properties of solid materials with bimorph piezotransducers", Key Engineering Materials, Vol. 543, pp 289-292, March 2013.

5. Yun-Che Wang, Chih-Chin Ko, Tien-Shu Chang and Chia-Min Wei, "Air damping induced from the interaction between a vibrating cantilever and its surroundings", Advances in Coupled System Mechanics, Seoul, Korea, August 26, 2012.

6. Yun-Che Wang, Chih-Chin Ko and Tien-Shu Chang, "Geometrically nonlinear cantilever beam under base excitation", the tenth conference on structure engineering, Taoyuan, Taiwan, December 1, 2010.

7. Tien-Shu Chang and Jiann-Wen Woody Ju, "Evaluation of freeze-thaw damage on hybrid fiber-reinforced concrete cylinders containing micro-encapsulated phase change material", 2021 ASCE Engineering Mechanics Institute Conference, Virtual on Zoom, May 26, 2021.

8. Tien-Shu Chang and Jiann-Wen Woody Ju, "Micromechanical damage formulation and experimental testing for internal freeze-thaw damage of porous concrete", 2019 ASCE Engineering Mechanics Institute Conference, Caltech, June 21, 2019.

Chapter 1 Introduction

1.1 Background and Motivation

Degradation of concrete materials due to freeze-thaw weathering often incurs significant repair costs for infrastructure in cold regions [1]. Without constant maintenance efforts, concrete structures may suffer from internal or surface damage. Researchers have indicated that these two types of damage could occur independently, and therefore could be thermally or mechanically prevented by using reinforcement in different scales [2], [3]. Phase change materials (PCMs) and microfibers are, individually, shown to be effective in enhancing the freeze-thaw durability of concrete.

Recent research has indicated that PCMs are potent to the thermal management in concrete structures, due to their remarkable heat storage capacity at the temperatures around their melting point [4]. If the incorporated PCM is designed with a transition temperature slightly above the freezing point of water, the number of freeze-thaw cycles experienced by the concrete components in cold climates can be decreased. Moreover, computer simulations conducted by Sakulich and Bentz [5] have demonstrated that a 4% by weight addition of the PCM could reduce the maintenance cost of bridge decks throughout the service lives under the freeze-thaw attack. The thermal robustness of the PCM in the concrete is dependent on the measure of incorporation. Farnam et al. [6] used the metal pipes containing PCMs in the slabs for melting the snow on the surface of concrete pavements. Microencapsulation is another approach to introduce PCMs into the matrix of concrete [7], [8]. The latter approach is favored, because the microscopic particle size leads to a higher overall surface area of PCM for efficient heat transmission. Yet, the

incorporation of PCM could decrease the compressive strength of concrete, and requires further reinforcement measures for use in practical construction [5].

Over the last few decades, the addition of steel fibers for improved strength and ductility of concrete has been extensively studied. The confining effect of steel fibers, which works similarly to stirrups in the reinforced concrete columns, primarily contributes to the increase of compressive strength. Nataraja et al. [9] reported that a 10% to 30% enhancement on the compressive strength could be achieved by adding steel fibers with a certain reinforcing index that is controlled by the fiber aspect ratio and the weight fraction of the fiber content. This degree of enhancement offers an opportunity to compensate for the strength loss due to the incorporation of soft particles like the PCM. Micromechanical models supported that the steel fibers, with appropriate aspect ratios, have positive effects on the compressive strength of concrete [10], [11]. Furthermore, the benefit of adding microfibers arises from their matching length scale to the microcracks, leading to a superior crack control performance upon scaling, spalling, and drying shrinkage of concrete [12], [13]. It appears possible, therefore, that by properly combining the PCM and the fibers in different scales, one can develop a structural concrete material with excellent freeze-thaw durability. Nevertheless, experimental investigations are needed to ensure the components retain their individual capacities in the hybrid form.

The present research is developed to investigate the influences of PCM dosage on the freeze-thaw durability and compressive behaviors of hybrid fiber-reinforced concrete. The concrete mix proportions are designed with varying the PCM volume fractions. The hybrid fiber, inclusive of the steel fiber and the polyvinyl alcohol microfiber, is mixed with a constant dosage. Uniaxial compression tests are performed on the concrete cylinders to evaluate the strengths at the age of 7 days and 28 days. The specimens are subjected to continuous freeze-thaw cycles with a

2

tailor-make freeze-thaw machine in a controlled environment. After the freeze-thaw weathering, the compressive strength and the static modulus of elasticity are determined for each specimen and compared with the values measured prior to the cycles for the freeze-thaw damage evaluation. Moreover, the changes in the relative dynamic modulus of elasticity, which is indicative of the internal damage extent of concrete, are obtained by ultrasonic pulse velocity tests over the freeze-thaw cycles. The experimental results will show that the added hybrid fiber considerably increases the compressive strength of concrete and sufficiently compensates for the strength loss due to the addition of PCM; the incorporation of the hybrid fiber and the PCM contribute to different aspects of the freeze-thaw durability (i.e., internal and superficial), at least to a different degree.

1.2 Scope of Research

Chapter 2 presents the literature review on the freeze-thaw damage of concrete. The surface damage and internal damage due to successive freeze-thaw cycles are reviewed. Air-entrained concrete, and high-performance fiber-reinforced concrete are introduced since they are the conventional methods to mitigate the freeze-thaw damage. The applications of phase change material are mentioned for a general understanding of the thermal buffering effect that can enhance the freeze-thaw durability of concrete. Reviews on thermodynamics theories are provided since the consequences of the theories are important in the field of continuum damage mechanics.

Chapter 3 presents the concrete mixture design details. The materials used to manufacture the concrete specimens are described. A custom-made freeze-thaw test machine and the corresponding mechanical design procedures are provided. Procedures and test setup for ultrasonic P-wave velocity test, uniaxial compression tests, and three-point bending tests are clearly described.

Chapter 4 provides the test results of the compressive behaviors and freeze-thaw durability of hybrid fiber-reinforced concrete, with varying volume fractions of PCM microcapsules. Test data analysis and discussion are carried out systematically. A novel damage model considering the beneficial effect and detrimental effect of adding PCM into fiber-reinforced concrete is proposed.

Chapter 5 offers the test results relative to the flexural behaviors and freeze-thaw damage of hybrid fiber-reinforced concrete, with distinct volume fractions of PCM microcapsules. Test data analysis is focused on the post-peak behaviors of concrete with hybrid fiber and PCM microcapsules.

Chapter 6 presents a temperature-dependent micromechanics damage model for hybrid-fiber-reinforced concrete containing phase change material. The crystallization pressure is considered with a volume-averaged procedure to quantify the stress exerted on the interior of concrete.

Chapter 2 Literature Review

2.1 Freeze-Thaw Damage of Concrete

In the cold region, concrete materials in a wide variety of structures can be prone to freeze-thaw damage. For example, a tunnel lining with a high degree of water saturation is likely to be influenced by freeze-thaw damage if the temperature is sufficiently low in tunneling structures, as shown in Figure 2-1. In fact, several theories have been proposed to explain the degradation of concrete exposed to freeze-thaw cycles. However, a theory that can explain all the observations in the laboratory or in real-world environments is not yet established.

To investigate the problem, it is convenient to classify the freeze-thaw damages of concrete into surface damage and internal damage, since these two types of damage can be prevented individually using reinforcement in different scales. This chapter is to conduct a literature review on the mechanisms and the preventive measures of freeze-thaw damage.
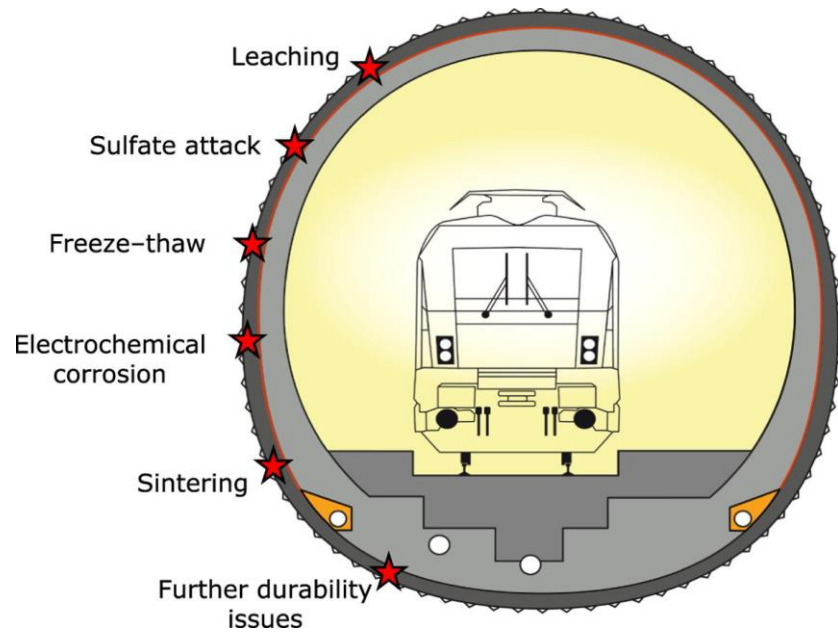
Figure 2-1. The concrete lining in a underground tunnel that would be prone to freeze-thaw

damage and other environmental attacks [14].

2.1.1 Surface Damage

The surface damage usually occurs at the concrete element that is covered by a layer of water in cold regions. It should be noted that salt scaling to the surface of concrete is due to a different mechanism and is controlled by different factors. For simplification, the salt scaling is excluded and not to be discussed by using non-saline solution in the experiments.

During an undercooling event, the adsorbed frozen water contracts more than the cement matrix because of the mismatch of their coefficients of thermal expansion. This activates the propagation of microcracks at the concrete skin by the glue-spalling mechanism [15]–[17]. In Figure 2-2, the glue-spalling mechanism, which is a technique used to decorate a glass surface, is applied to explain the surface damage mechanism of concrete when lowering the ambient temperature. Consequently, small chips flake off at the concrete surface, resulting in the increase of permeability of the concrete that would facilitate the ingress of harmful chemicals. Moreover, concrete with higher permeability is more vulnerable to the surface damage, and therefore the deterioration becomes faster, which can be explained by the cryogenic suction mechanism at the concrete surface [18]. In general, the water layer, the mismatch of thermal expansion coefficients, and temperature variations are the key factors in the surface damage of concrete.

For the evaluation purpose, ASTM C672 provides a visual rating chart to qualitatively determine the level of scaling damage by the exposure of coarse aggregates. A more rigorous methodology, however, needs to be established to quantify the extent of the surface damage in a more detailed manner.

(a)　Sandblasted Glass Surface

Glass

(b)　$T=T_0$

Epoxy

Glass

(c)　$T \ll T_0$

Scalloped Surface
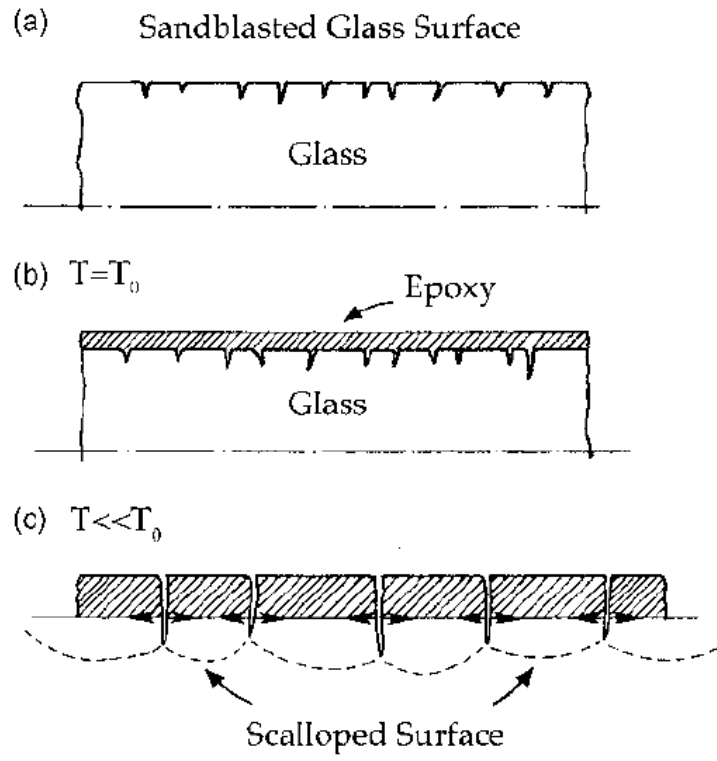
Figure 2-2. Schematic representation of the glue-spall mechanism [2].

2.1.2 Internal Damage

The internal damage is caused by the progressively built-up hydraulic pressure and crystallization pressure inside the concrete pore system that is sufficiently saturated during the recurring freezing and thawing cycles. In Figure 2-3, the crystallization pressure in the pore system of concrete can be estimated by the product of the curvature of crystal front and the specific interface energy between the ice and water. Although the mechanisms of the damage are not fully understood and therefore debatable, most researchers have confirmed that the freezing of water in the capillaries entirely contributes to the internal frost damage [19]–[21]. In general, the internal freeze-thaw cracking would cause subtle strength loss at the early exposure because the size of cracks is too small. The strength would drop significantly with a dozen of freeze-thaw cycles for concrete without appropriate protection. Therefore, a health monitoring system with high fidelity is desired for structural components. Among all available techniques, ultrasonic pulse velocity (UPV) testing is accurate, simple to use, and therefore widely adopted to evaluate the internal cracking and the strength loss of concrete [22], [23]. Thus, UPV testing is employed in this research to capture the damage evolution inside the concrete.
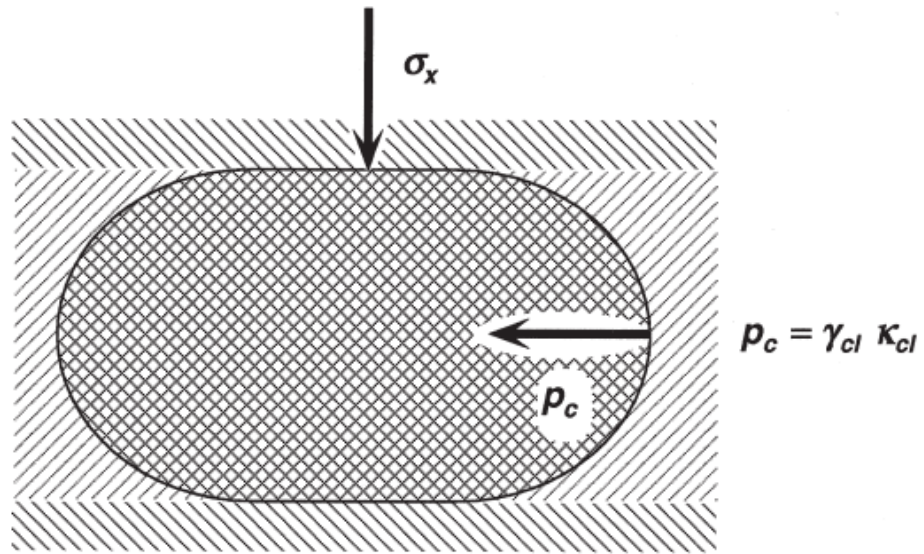
Figure 2-3. The crystallization pressure in the pore system of concrete [21].

2.2 Concrete Mixture Design to Mitigate Freeze-thaw Damage

2.2.1 Air-Entrained Concrete

Introducing a distributed network of small air voids with sizes between 10 microns and 1 mm into fresh concrete was shown to be an effective measure to mitigate the internal damage [24]. The extended pore system provides extra room for water migration and ice nucleation, relieving the hydraulic pressure exerted on the concrete skeleton.

While the air-entrained concrete has beneficial outcomes on the prevention of freeze-thaw damage, adverse consequences on mechanical properties have been reported in ACI 212.3R. For instance, a 7% of deliberately entrained air volume can lead to a 35% decrease in compressive strength. Figure 2-4 shows the effect of water-cement ratio on the compressive strength of concrete with air-entrainment. As the compressive strength is reduced significantly, the air-entrained concrete is less than ideal for structures requiring high load-carrying capacities, such as bridge footing, concrete dams, and underground tunnels.
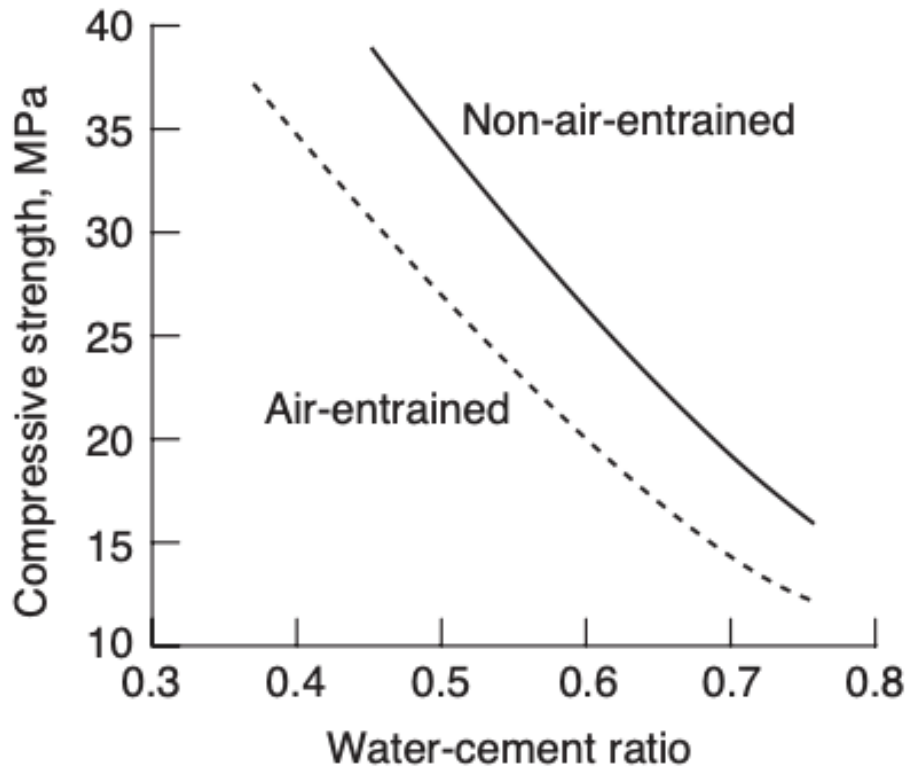
Figure 2-4. The relationships between compressive strength and water-cement ratio for concrete with and without air-entrainment [25].

2.2.2 Phase Change Materials in Concrete

Recently, the applications of phase change material (PCM) in freeze-thaw mitigation in concrete infrastructures has been studied by Bentz and Turpin [26], Yeon and Kim [27], Nayak et al. [28], Pilehvar et al. [8], and Jayalath et al. [7]. PCMs are regarded as an extremely efficient thermal energy storage methodology because of their remarkable heat capacity and latent heat that can be utilized to manage the concrete temperature in a comfort range [4]. With a selected PCM having a melting temperature slightly higher than the freezing point of water, a fraction of freeze-thaw cycles experienced by a concrete component can be reduced without extra energy consumption. Figure 2-5 illustrates practical methods used to contain PCMs in the concrete components. Sakulich and Bentz demonstrate that under the freeze-thaw weathering, a 50 kg/m^3 addition of the PCM in a bridge deck can extend the bridge service life by at least one year [5]. Farnam et al. embed metal pipes containing PCM into the concrete pavement to melt ice and snow [6]. Micro-encapsulation is a favored approach to carry PCMs in the concrete. The shell can prevent the leakage of liquid PCM. Meanwhile, the microscopic particle size can provoke a higher overall surface area for efficient heat transmission. Moreover, Šavija and Schlangen demonstrate that the early-age thermal cracking in mass concrete can be diminished by including the micro-encapsulated PCM [29]. On the contrary, Wei et al. find that the PCM micro-particles have little contribution to the drying shrinkage of cement mortar [30]. Norvell et al. reveal that the micro-encapsulated PCM in the concrete can significantly decrease the compressive strength of the structural element [31].
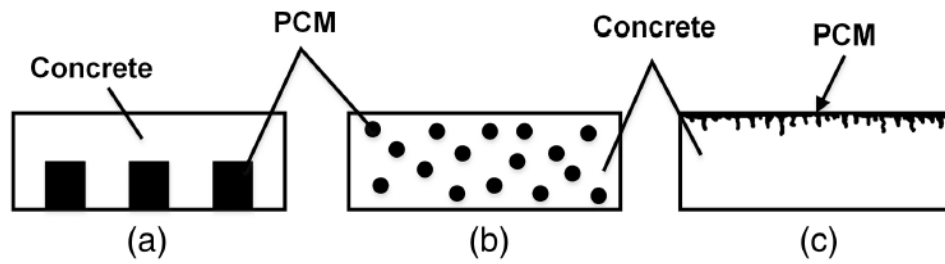
Figure 2-5. Methods of incorporating phase change materials (PCMs) into concrete. (a) Metal pipes containing PCM. (b) Microcapsules containing PCM. (c) Filing concrete surface voids via PCM absorption [32].

2.2.3 High-Performance Fiber-reinforced Concrete

Adding fibers into concrete elements for improved mechanical properties has been studied for many decades with fruitful results. Steel fibers, for instance, are widely used to enhance the strength and toughness of concrete composites. Nataraja et al. have reported that a 10 to 20% higher compressive strength can be achieved by the 0.5 to 1% by volume incorporation of undulated steel fibers with non-uniform lengths between 27.5 and 41 mm [9]. Similar findings are revealed by Song and Hwang who used hook-end steel fibers with a uniform length of 35 mm [33]. Micromechanical models proposed by Zhang et al. [10] and Moradi et al. [11] also support that the presence of steel fibers in such dimensions has positive effects on the compressive strength of concrete. In another study, Olivito and Zuccarello [34] indicate that the fracture mode of the concrete transforms from fragile to ductile when adding the steel fibers, and the specimens remain their integrity without crumbling during the testing.   Displays the distinct fracture modes of plain concrete and fiber-reinforced concrete. Moreover, steel fiber reinforcement with appropriate fiber dimensions is advantageous to the freeze-thaw resistance of concrete to a considerable degree. Experiments conducted by Sun et al. [35] and Mu et al. [36] show that the inclusion of steel fiber contains the internal cracking of the concrete, and the changes of dynamic modulus of elasticity are retained in 10% after 50 cycles of freezing and thawing. In general, the beneficial effect on maintaining the internal damage of concrete is found in studies that use steel fibers with similar dimensions for improving the compressive strengths of concrete [37]–[39]. Steel fibers, however, do not directly contribute to the surface damage of concrete [16]. Instead, the spalling or flaking due to freeze-thaw weathering can be controlled by adding synthetic microfibers, largely because of their microscale sizes and superior ductility. Şahmaran and Li show that the addition of polyvinyl alcohol fibers with a length of 8 mm shows a positive impact on the scaling resistance

[12]. Karahan and Duran indicate that the microfibers also have a beneficial effect on preventing the drying shrinkage of concrete [13]. Nevertheless, in the same study the influence of microfibers, with a dosage of 1.8 kg/m^3 or 0.2% by volume, is found insignificant on the compressive strength of concrete.

2.3 Primers on Thermo-Mechanical Continuum Damage Mechanics

The first law and the second law of thermodynamics provide important restrictions on the form of constitutive relations. These restrictions are described by Clausius-Duhem inequality and the consequential irreversible (or non-negative) energy dissipation equations.

2.3.1 Review of the First Law of Thermodynamics

Considering a closed system (i.e., no mass exchange) of a finite volume, the First Law of Thermodynamics states that there exists an internal energy function such that the following balance equation is satisfied:

$$\dot{U} + \dot{K} = P_{ext} + P_{cal} \tag{2-1}$$

which reads that the sum of the internal energy with the kinetic energy changes at a rate equal to the sum of the external power and the rate of heat supply. The kinetic energy is defined as

$$K = \frac{1}{2} \int_{\Omega} \rho \boldsymbol{v} \cdot \boldsymbol{v} \, dV \tag{2-2}$$

where ρ is the mass density and $\boldsymbol{v}$ is the velocity. The external power is given by

$$P_{ext} = \int_{\Omega} \boldsymbol{b} \cdot \boldsymbol{v} \, dV + \int_{\Gamma} \boldsymbol{t} \cdot \boldsymbol{v} \, dS \tag{2-3}$$

where $\boldsymbol{b}$ is a vector of body forces due to external force fields acting directly on the material particles, and $\boldsymbol{t}$ is a vector of the tractions acting on the boundary. The heat supply is expressed as

$$P_{cal} = \int_{\Omega} \rho \gamma \, dV - \int_{\Gamma} \boldsymbol{q} \cdot \boldsymbol{n} \, dS \tag{2-4}$$

17

where γ is the heat source (rate of heat per unit mass) coming from absorption of radiation, and $\boldsymbol{q}$ is the heat flux (rate of heat per unit area). If the heat flux is oriented in the same direction as the outward normal $\boldsymbol{n}$, the negative sign in the equation tells us the heat is flowing out of the body.

It should be noted that equation (2-1) is the global form of the first law. A local form is obtained by taking the limit for an infinitely small volume. To this end, converting all the surface integrals into volume integrals. In the external power expression

$$\int_\Gamma \boldsymbol{t} \cdot \boldsymbol{v} \, dS = \int_\Gamma t_i v_i \, dS \tag{2-5}$$

$$= \int_\Gamma v_i \sigma_{ij} n_j \, dS$$

$$= \int_\Omega \frac{\partial (v_i \sigma_{ij})}{\partial x_j} \, dV$$

$$= \int_\Omega \sigma_{ij} \frac{\partial v_i}{\partial x_j} \, dV + \int_\Omega v_i \frac{\partial \sigma_{ij}}{\partial x_j} \, dV$$

$$= \int_\Omega \boldsymbol{\sigma} : \dot{\boldsymbol{\epsilon}} \, dV + \int_\Omega \boldsymbol{v} \cdot (\boldsymbol{\sigma} \cdot \nabla) \, dV$$

The external power hence becomes

$$P_{ext} = \int_\Omega \boldsymbol{v} \cdot (\boldsymbol{b} + \boldsymbol{\sigma} \cdot \nabla) \, dV + \int_\Omega \boldsymbol{\sigma} : \dot{\boldsymbol{\epsilon}} \, dV \tag{2-6}$$

$$= \int_\Omega \boldsymbol{v} \cdot \rho \dot{\boldsymbol{v}} \, dV + \int_\Omega \boldsymbol{\sigma} : \dot{\boldsymbol{\epsilon}} \, dV$$

$$= \dot{K} + P_{int}$$

where P_{int} is called the internal power (stress power). Similar treatment to the heat power expression leads to

$$\int_\Gamma \boldsymbol{q} \cdot \boldsymbol{n} \, dS = \int_\Gamma q_i n_i \, dS \tag{2-7}$$

$$= \int_\Gamma \frac{\partial q_i}{\partial x_i} \, dV$$

$$= \int_\Gamma \boldsymbol{\nabla} \cdot \boldsymbol{q} \, dV$$

The heat power is rewritten as

$$P_{cal} = \int_\Omega (\rho\gamma - \boldsymbol{\nabla} \cdot \boldsymbol{q}) \, dV \tag{2-8}$$

Substitution of equation (2-6) and equation (2-8) into equation (2-1) results in the following expression for the internal energy function,

$$\dot{U} = \int_\Omega (\boldsymbol{\sigma} : \dot{\boldsymbol{\epsilon}} + \rho\gamma - \boldsymbol{\nabla} \cdot \boldsymbol{q}) \, dV \tag{2-9}$$

Subsequently, introducing specific internal energy, u, where $U = \int_\Omega \rho u \, dV$, to replace the U,

$$\int_\Omega (\rho\dot{u} - \boldsymbol{\sigma} : \dot{\boldsymbol{\epsilon}} - \rho\gamma + \boldsymbol{\nabla} \cdot \boldsymbol{q}) \, dV = 0 \tag{2-10}$$

If the integrand is continuous, the integral must vanish for any partial volume within the finite body. This argument leads to the local form of the first law,

$$\rho\dot{u} = \boldsymbol{\sigma} : \dot{\boldsymbol{\epsilon}} + \rho\gamma - \boldsymbol{\nabla} \cdot \boldsymbol{q} \tag{2-11}$$

Resulting from the local energy balance, this equation describes that the rate of increase of internal energy in an elementary volume is equal to the sum of: (1) the power of stress working on the

strain rate; (2) the heat supplied by an internal source of intensity γ; and (3) the negative divergence of the heat flux, which shows the net rate of heat entering the elementary volume through its boundary.

2.3.2 Review of the Second Law of Thermodynamics

Considering a closed system (no mass exchange) of a finite volume, the Second Law of Thermodynamics states that there exists a state function of entropy such that the following inequality is satisfied:

$$\dot{S} \geq \int_\Gamma \frac{\rho\gamma}{T} \, dV - \int_\Gamma \frac{q \cdot n}{T} \, dS \tag{2-12}$$

which reads that the rate of the entropy of the system is never less than the rate of the entropy due to the heat source and the heat flux. To obtain the local form of the second law, one should convert all the surface integral to the volume integral,

$$\int_\Gamma \frac{q \cdot n}{T} \, dS = \int_\Gamma \frac{q_i n_i}{T} \, dS \tag{2-13}$$

$$= \int_\Omega \frac{\partial}{\partial x_i} \left(\frac{q_i}{T}\right) dV$$

$$= \int_\Omega \nabla \cdot \left(\frac{q}{T}\right) dV$$

$$= \int_\Omega \left(\frac{\nabla \cdot q}{T} - \frac{q \cdot \nabla T}{T^2}\right) dV$$

Subsequently, introducing the specific entropy s, where $S = \int_\Omega \rho s \, dV$, to replace the entropy function S in the global form,

$$\int_{\Omega} \rho \dot{s} \, dV \geq \int_{\Omega} \left(\frac{\rho \gamma}{T} - \frac{\boldsymbol{\nabla} \cdot \boldsymbol{q}}{T} + \frac{\boldsymbol{q} \cdot \boldsymbol{\nabla} T}{T^2} \right) dV \qquad (2\text{-}14)$$

If the integrands are continuous, this inequality holds for any partial volume within the finite body. Therefore, the integrands themselves satisfy the inequality and it yields the local form of the second law as following,

$$\rho \dot{s} \geq \frac{\rho \gamma - \boldsymbol{\nabla} \cdot \boldsymbol{q}}{T} + \frac{\boldsymbol{q} \cdot \boldsymbol{\nabla} T}{T^2} \qquad (2\text{-}15)$$

The difference between two sides of this inequality is called the rate of internal entropy production, and physically it shows the complexity and disorder of the internal state of an elementary volume.

It is lately found convenient to introduce the density of energy dissipation rate, D, defined as the rate of internal entropy production per unit volume multiplied by the absolute temperature. Since the absolute temperature is always positive, the second law is equivalent to the condition of non-negative dissipation,

$$D \equiv T\rho \dot{s} - \rho \gamma + \boldsymbol{\nabla} \cdot \boldsymbol{q} - \frac{\boldsymbol{q} \cdot \boldsymbol{\nabla} T}{T} \geq 0 \qquad (2\text{-}16)$$

Based on the local form of the first law, one can replace $\boldsymbol{\nabla} \cdot \boldsymbol{q} - \rho \gamma$ by $\boldsymbol{\sigma} : \dot{\boldsymbol{\epsilon}} = \rho \dot{u}$ and arrive at the **Clausius-Duhem inequality**,

$$D = \boldsymbol{\sigma} : \dot{\boldsymbol{\epsilon}} - \rho(\dot{u} - T\dot{s}) - \frac{\boldsymbol{q} \cdot \boldsymbol{\nabla} T}{T} \geq 0 \qquad (2\text{-}17)$$

Let us define a set of state variable $(\boldsymbol{\epsilon}, \boldsymbol{\alpha}, T)$, which $\boldsymbol{\alpha}$ is the internal variables other than strain and temperature. It turns out to be useful to transform the internal energy function u into a new state function as following,

$$\Psi(\epsilon, \alpha, T) = u(\epsilon, \alpha, T) - Ts \tag{2-18}$$

which is usually called the Helmholtz free energy function. The time derivative is given by

$$\dot{\Psi} = \dot{u} - \dot{T}s - T\dot{s} \tag{2-19}$$

An alternative form of the Clausius-Duhem inequality can be read as

$$D = \boldsymbol{\sigma} : \dot{\boldsymbol{\epsilon}} - \rho(\dot{\Psi} + \dot{T}s) - \frac{q \cdot \nabla T}{T} \geq 0 \tag{2-20}$$

which is called the dissipation inequality.

For a general process with variable ϵ, T and $\boldsymbol{\alpha}$, the rate of the free energy function reads

$$\dot{\Psi} = \frac{\partial \Psi}{\partial \boldsymbol{\epsilon}} : \dot{\boldsymbol{\epsilon}} + \frac{\partial \Psi}{\partial T} \dot{T} + \frac{\partial \Psi}{\partial \boldsymbol{\alpha}} \circ \dot{\boldsymbol{\alpha}} \tag{2-21}$$

the operator "$\circ$" is reserved for the appropriate form of the tensor $\boldsymbol{\alpha}$ whose order is not yet specified.

Substitution of equation (2-21) into equation (2-20) yields

$$D = D_m + D_T + D_\alpha \geq 0 \tag{2-22}$$

where

$$D_m = \left(\boldsymbol{\sigma} - \rho \frac{\partial \Psi}{\partial \boldsymbol{\epsilon}}\right) : \dot{\boldsymbol{\epsilon}} \tag{2-23}$$

$$D_T = -\rho\left(s + \frac{\partial \Psi}{\partial T}\right)\dot{T} - \frac{\boldsymbol{q} \cdot \nabla T}{T} \tag{2-24}$$

$$D_\alpha = -\rho \frac{\partial \Psi}{\partial \boldsymbol{\alpha}} \circ \dot{\boldsymbol{\alpha}} \qquad\qquad (2\text{-}25)$$

The second law essentially requires that Eq. (2-22) must be non-negative. In 1960, Truesdell and Noll replaced this condition by a stronger one, namely that each of these three dissipation terms taken separately must be non-negative.

Chapter 3 Specimen Descriptions and Testing Methodology

3.1 Hybrid Fiber-reinforced Concrete Containing Microencapsulated Phase Change Material

3.1.1 Mixture Designs

The mixture design adopted for the present work was prepared to provide a freeze-thaw durable concrete material with a higher or comparable compressive strength to plain concrete without deliberate air entrainment. To tailor the physical properties of the structural material, the concept of fiber hybridization with a phase change material (PCM) was exploited in the design of mixtures. Microencapsulated paraffin was incorporated for thermal buffering to reduce the intensity of temperature variations in the material upon freeze-thaw cycles. Steel fiber was added to increase the strength and to compensate for the loss due to the addition of the soft microcapsules. Polyvinyl alcohol (PVA) fiber was used for improving ductility and durability upon cyclic freeze-thaw action. In this work, the focus has been put on the effects of the PCM dosage on the freeze-thaw durability and the compressive strength, while other factors (e.g., moisture content, type of cement, water-to-binder ratio, aggregate size and quality, fiber geometry and content, fly ash content, curing condition, etc.) are all considered and controlled to produce directly comparable results.

Three different mixtures with PCM and hybrid fiber were designed, varying the PCM volume fraction from 0% to 7%, in addition to one reference mix. Table 3-1 illustrates the designation and the fractions of the two fibers and PCM microcapsules for each concrete mixture. The individual fiber content is decisive to assure that the desired mechanical performance is

24

achieved. As a first approximation, adding 1% of the steel fiber should compensate for the compressive strength reduced by 5% of the PCM microcapsules. It should be noted that a higher steel fiber content may lead to a considerable decrease in the workability of fresh concrete slurry. Subsequentially, the concrete cannot be properly compacted, and its compressive strength can be reduced. The PVA fiber content was set at a low amount of 0.1% to contain the negative effect on the compressive strength while remaining the positive effect on the durability.

Table 3-2 shows the mixture proportions, following the design procedures described in ACI 211.1. A slump range of 3" to 4"and a maximum aggregate size of 1/2" were selected and executed in the design. Olivito and Zuccarello [34] suggested that the maximum aggregate size should not exceed 0.5 times the length of the steel fiber to attain a uniform fiber distribution. Consequently, the water-cementitious materials ratio was designed with the maximum aggregate size according to ACI 544.1R. The Class F fly ash was used to replace 15% of the cement by weight. To improve the workability affected by the presence of fibers, the superplasticizer equal to 0.3% of the cement weight was added in the mixtures. Based on our experience, even more water reducers are needed for the concrete mixtures with PCM to attain satisfactory workability. Moreover, the volume fraction of coarse aggregates, depending on the maximum aggregate size and the fineness modulus of the sand, was set equal to 50%. The weight of coarse aggregates and that of fine aggregates were determined by the absolute volume method described in ACI 211.1. The PCM microcapsules were added by replacing the fine aggregates on a volume basis.

Table 3-1. Volume fractions of the fibers and PCM microcapsules in the concrete mixtures.

Designation	PC	HFRC	M5-HFRC	M7-HFRC
Steel fiber (vol. %)	-	1	1	1
PVA fiber (vol. %)	-	0.1	0.1	0.1
PCM (vol. %)	-	-	5	7
PCM (wt. %)	-	-	1.9	2.7

Table 3-2. The concrete mixture proportions for cylinders.

Designation	PC	HFRC	M5-HFRC	M7-HFRC
Water (kg/m^3)	207.7	216.7	216.7	216.7
Cement (kg/m^3)	392.3	428.7	428.7	428.7
Fly ash (kg/m^3)	69.2	75.6	75.6	75.6
W/CM ratio [a]	0.45	0.43	0.43	0.43
Gravel (kg/m^3)	902	805	805	805
Sand (kg/m^3)	747	709	664	646
Steel fiber (kg/m^3)	-	78.5	78.5	78.5
PVA fiber (kg/m^3)	-	1.3	1.3	1.3
PCM (kg/m^3)	-	-	45	63
Superplasticizer (kg/m^3)	-	1.5	2	2

[a] Water-cementitious materials ratio = water/(cement + fly ash).

3.1.2 Materials

Portland cement type II/V and Class F fly ash from CalPortland were adopted. Natural river sand (with fineness modulus = 2.7, absorption capacity = 0.7%, and bulk specific gravity = 2.64), conforming to the grading requirements in ASTM C33, was purchased from Quikrete. The locally available coarse aggregates were composed of crushed stone and gravel (with absorption capacity = 0.5%, and bulk specific gravity = 2.68), provided by Caltrans without gradation. Mechanical sieving analysis was therefore performed to obtain continuously graded coarse aggregates in accordance with ASTM C33. Figure 3-1 illustrates the particle size distribution of the coarse aggregates.

The steel fibers (Dramix RC-65/35-BN), with a circular cross-section, hooked ends, and uniform size, were purchased from Bekaert. The monofilament PVA microfibers (RECS 15) were manufactured by Nycon. Table 3-3 summarizes the dimensions, physical and mechanical properties of the two fibers.

The PCM microcapsules (MPCM-6D) were obtained from Microtek. Table 3-4 exhibits the materials and physical properties of the PCM microcapsules. In Figure 3-3, the size of the PCM microcapsules was confirmed by scanning electron microscopy.
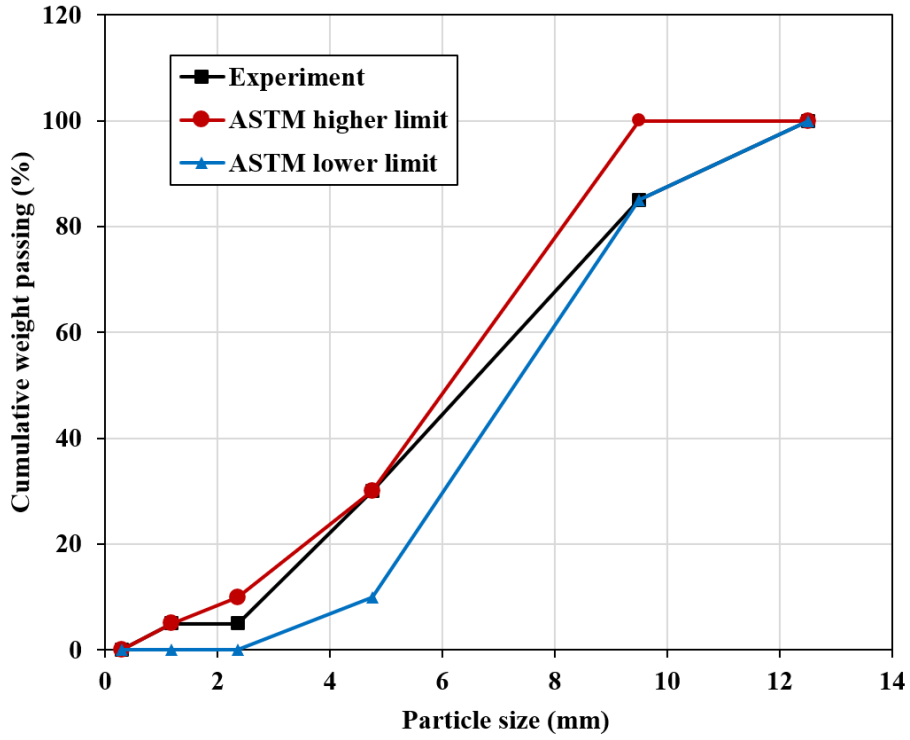
Figure 3-1. The comparison of particle size distribution of the coarse aggregates with the upper

and lower bounds in ASTM C33.
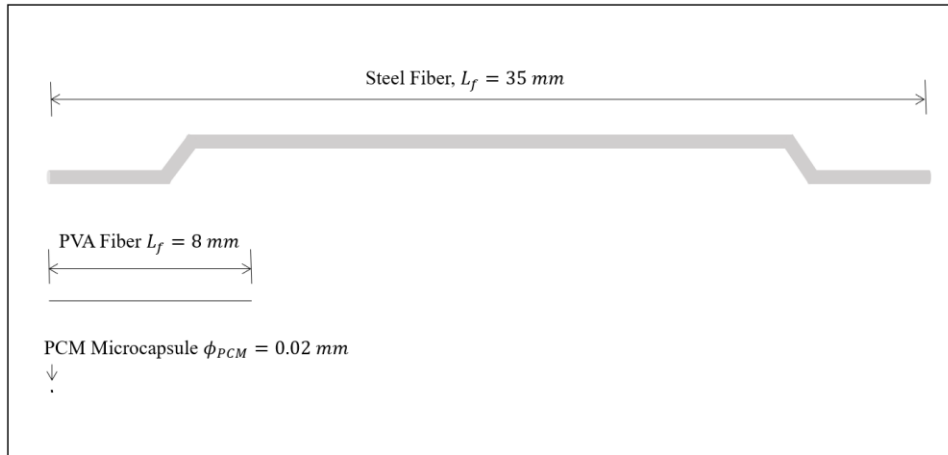
Figure 3-2. The length comparison of the steel fiber, the PVA fiber, and the PCM microcapsule.
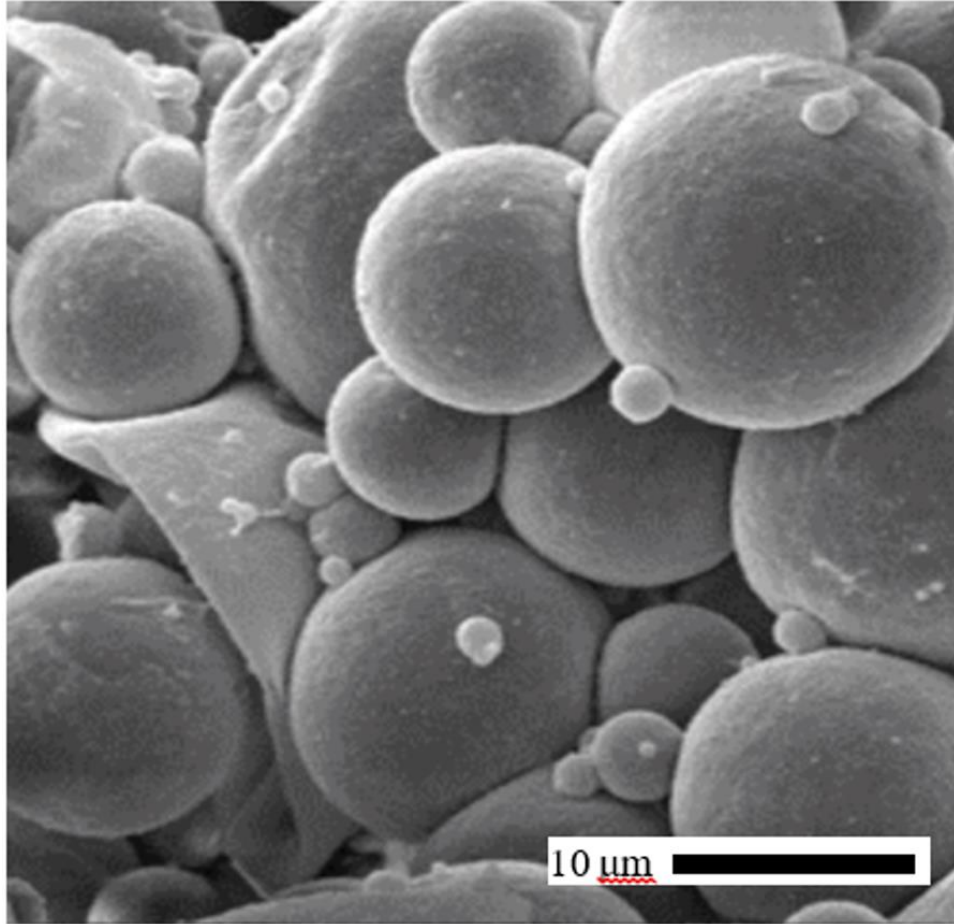
Figure 3-3. The PCM microcapsules under scanning electron microscopy.

Table 3-3. Dimensions, physical and mechanical properties of fibers.

Fiber type	Hooked-end steel	Monofilament polyvinyl alcohol
Length, L_f (mm)	35	8
Diameter, D (mm)	0.55	0.038
Aspect ratio (L/D)	65	210
Specific gravity	7.85	1.3
Melting point (°C)	1410	225
Tensile strength (GPa)	1.35	1.6
Modulus of elasticity (GPa)	210	23

Table 3-4. Materials and physical properties of the PCM microcapsules.

Appearance	White dry powder
Composition	85-90 wt.% PCM; 10-15 wt.% polymer shell
Core material	Alkane
Capsule shell	Melamine formaldehyde
Particle size (μm)	5-20
Melting point (°C)	6
Heat of fusion (J/g)	210
Specific gravity	0.9

3.1.3 Specimen Preparation

Fifty-two concrete cylinders of 101.6 mm in diameter and 203.2 mm in height were manufactured using the mixture proportions in Table 3-2 (i.e., thirteen specimens for each composition). The numbers of specimens, types of mixtures, types of tests and the test outputs for the cylindrical concrete specimens are provided in Table 3-5. The mixing and casting procedures were referenced to ASTM C94 and ASTM C192. The specimens were prepared using single-use molds with caps to prevent evaporation of water. To ensure the homogeneity of the concrete mixture, dry ingredients were blended by a mixer for a period until the fibers are dispersed equally in all directions. Subsequently, water and superplasticizer were gradually added into the mixture and mixed for another 7 mins. The fresh mixture was examined by slump test to ensure consistency, and then placed into the molds with minimal but effective mechanical agitation to reduce their influences on the distribution of fibers.

The cylindrical specimens were removed from the molds 24 hours after casting and cured in saturated limewater at a constant temperature of 23°C according to ASTM C192. The curing process was continued to the moments of compression test for determining the early-age strengths. Alternatively, some of the specimens were cured for 28 days and were properly stored in a controlled environment thereafter for approximately 5 years to allow any significant strength growth prior to the freeze-thaw experiment.

Eighteen notched concrete beams of 101.6 mm in depth, 101.6 mm in height, and 355.6 mm in length were prepared using the HFRC and M5-HFRC mixture proportions in Table 3-2, and a mixture design of 9% PCM for exploratory purposes, which will be clearly described in Chapter 5. The notch is 101.6 mm in depth and 25.4 mm in height. The numbers of specimens,

types of mixtures, types of tests and the test outputs for the prismatic concrete specimens are

provided in Table 3-6.

Table 3-5. Numbers of specimens, types of mixtures, types of tests, and the test outputs for the cylindrical concrete specimens.

Number of specimens	Mixture	Testing method	Output
4	PC	Compression test	7-day strength
4	HFRC	Compression test	7-day strength
4	M5-HFRC	Compression test	7-day strength
4	M7-HFRC	Compression test	7-day strength
4	PC	Compression test	28-day strength
4	HFRC	Compression test	28-day strength
4	M5-HFRC	Compression test	28-day strength
4	M7-HFRC	Compression test	28-day strength
2	PC	Compression test	Undamaged strength and stiffness
2	HFRC	Compression test	Undamaged strength and stiffness
2	M5-HFRC	Compression test	Undamaged strength and stiffness
2	M7-HFRC	Compression test	Undamaged strength and stiffness
3	PC	Freeze-thaw, ultrasonic, and compression tests	Damage variables
3	HFRC	Freeze-thaw, ultrasonic, and compression tests	Damage variables
3	M5-HFRC	Freeze-thaw, ultrasonic, and compression tests	Damage variables
3	M7-HFRC	Freeze-thaw, ultrasonic, and compression tests	Damage variables
1	Quikrete	Freeze-thaw test	Temperature profile

Table 3-6. Numbers of specimens, types of mixtures, types of tests, and the test outputs for the prismatic concrete specimens.

Number of specimens	Mixture	Testing method	Output
3	HFRC	Three-point test	Undamaged load-displacement curve
3	M5-HFRC	Three-point test	Undamaged load-displacement curve
3	M9-HFRC	Three-point test	Undamaged load-displacement curve
3	HFRC	Freeze-thaw, ultrasonic, and three-point test	Damaged load-displacement curve
3	M5-HFRC	Freeze-thaw, ultrasonic, and three-point test	Damaged load-displacement curve
3	M9-HFRC	Freeze-thaw, ultrasonic, and three-point test	Damaged load-displacement curve
1	Quikrete	Freeze-thaw test	Temperature profile

3.2 Freeze-thaw Test

The concrete specimens were exposed to successive freeze-thaw cycles to assess the freeze-thaw durability with the variations in their mechanical performance. In particular, the relative dynamic modulus of elasticity, the compressive strength, the static modulus of elasticity, the fracture energy, the flexural tensile strength, and the residual flexural tensile strength were individually obtained from ultrasonic and compression tests detailed in the next sections. The surface condition after the exposure of 30 freezing and thawing cycles was otherwise evaluated using a visual rating scale provided in ASTM C672.

In the freeze-thaw test, the specimens were subjected to 50 cycles of freeze-thaw action with a constant rate of 1 cycle/day. An Arduino-based computer-automated freeze-thaw machine, as exhibited in Figure 3-4, was a custom design by the authors to weather specimens with a cylindrical shape. It is worthy to mention that the cylinders provide more realistic compression test results compared with the cubes or the prisms. During the freeze-thaw tests, specimens were covered by a uniform 2.92 mm thin water layer on all surfaces and sealed individually inside a tailored chamber. The chambers for concrete specimens were purchased from VISPAK. The dimensions and material of the container are summarized in Table 3-7. To verify the specimen temperature with the pre-programmed temperature profile, thermocouples were instrumented both at the specimen chamber and at the center of a control specimen. Figure 3-5 shows the measured freeze-thaw temperature, alternating between +20℃ and -30℃, and the temperature measured at the center of the control specimen, varying between +14℃ and -23℃, for a prototypical cycle. After 30 freeze-thaw cycles, specimens were carefully taken out of the freeze-thaw machine for visual inspection on the surface condition and for ultrasonic testing to assess the internal damage

extent. Thereafter, the specimens were put back into the machine with identical temperature settings to continue the experiment until the completion of 50 freeze-thaw cycles.

It was worth mentioning that if the concrete was not sufficiently saturated (i.e., at least 90% saturation degree), the internal freeze-thaw damage would not occur. The reason was that the water in the pore structure was not fully confined during the cooling events. The non-saturated pores provided the room for volumetric expansion of the ice, and the hydraulic stress and the crystallization stress combined did not reach the critical threshold for the internal cracking of concrete. In the freeze-thaw test, the specimens were submerged in water during the cycles and therefore the required saturation degree was ensured.

In a previous study conducted by Chung [40], the freeze-thaw damage was not observed for concrete specimens subjected to over 300 freeze-thaw cycles. The freezing temperature was set to -23℃. The freezing and thawing periods were both 12 hours. The possible reason for the unexpected experimental results would be the excessive mass, including the mass of specimens and water, put into the freezer such that the concrete specimens were not frozen to a designated cooling temperature (see Figure 3.7 in [40]). Therefore, a temperature verification was performed in this dissertation, as detailed in Section 3.2.2, to ensure that the specimens were fully frozen.
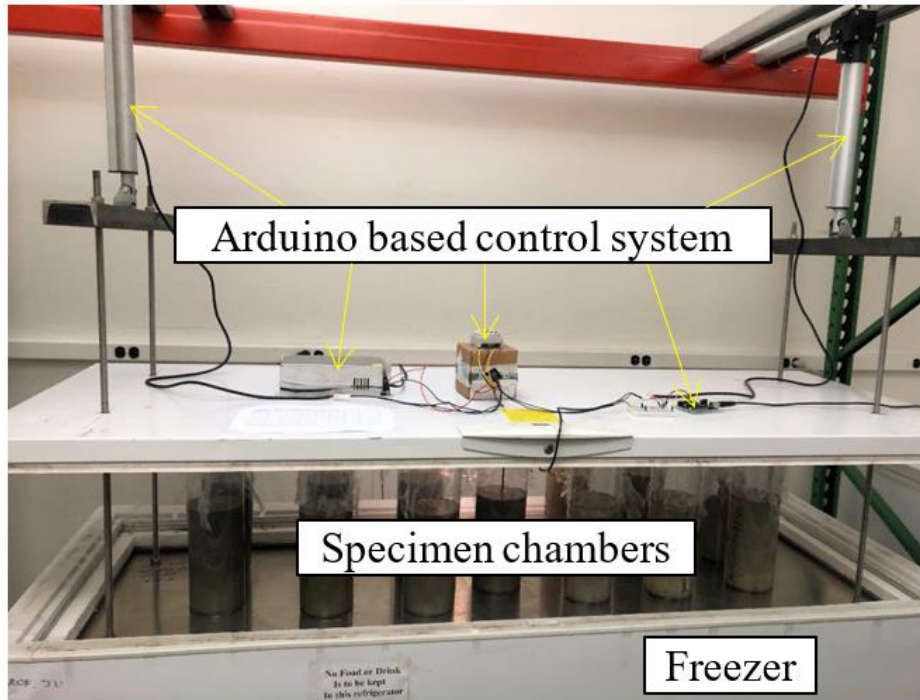
Figure 3-4. The computer-automated freeze-thaw machine with Arduino microcontroller for weathering cylindrical concrete specimens.
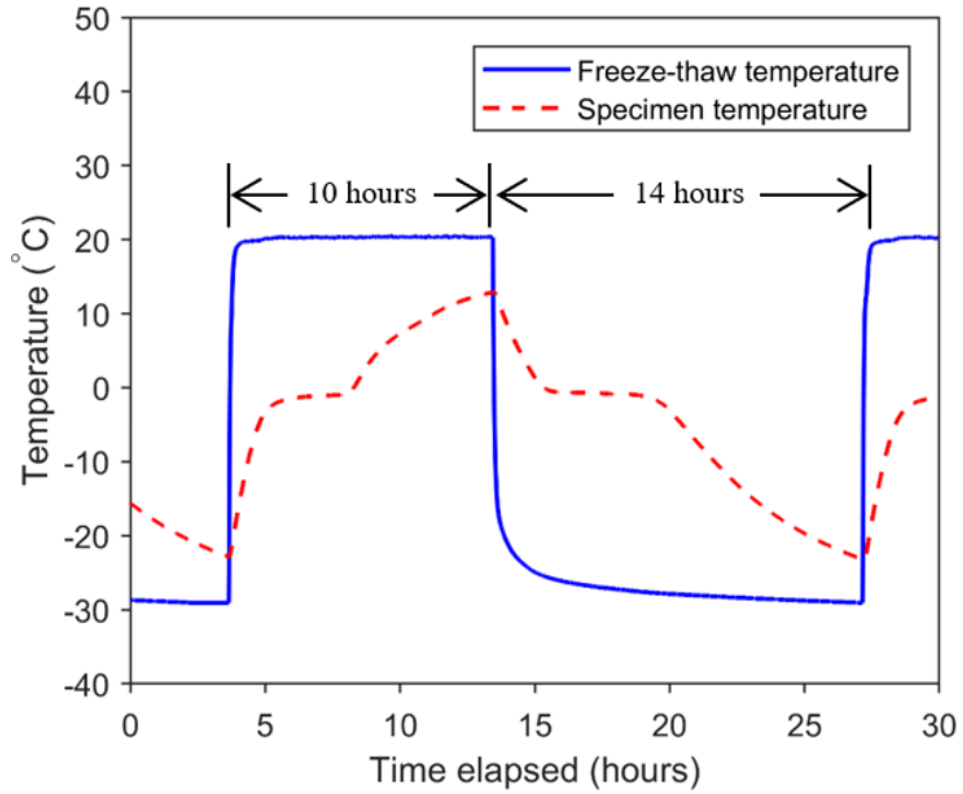
Figure 3-5. The temperature profile measured at the climate chamber and at the center of a control

cylindrical specimen for one freeze-thaw cycle.

Table 3-7. The specification of the cylindrical container used for the concrete cylinders in the freeze-thaw test.

Appearance	
Material	Cellulose acetate propionate
Inner diameter (in)	4.230
Outer diameter (in)	4.288
Thickness (in)	0.029
Height (in)	12

3.2.1 Computer-Automated Freeze-Thaw Climate Chamber

The motivation to build a new freeze-thaw climate chamber was mostly driven by the fact that there were few commercially available freeze-thaw machines in the market for testing concrete materials, and the limitations on the dimensions of specimen could not meet the requirements in standardized mechanical tests, such as the standardized testing method for compressive strength of concrete, ASTM C39. In fact, a commercial freeze-thaw machine would cost $24,000 at least, not including the containers used to maintain constant moisture for the specimens. Time-consuming was an issue in addition to the dimensional requirements of the specimen. In laboratory it was possible to accelerate the deterioration of mechanical properties of materials by applying more cycles in one day. Ideally, the process of freeze-thaw cycles should be automated to reduce the required human labor and to increase the reliability of the test. To this end, an automated freeze-thaw machine was designed and fabricated. As exhibited in Figure 3-6, a conceptual model was built using the software SolidWorks.

To validate the loading capacity of the main structural component in the machine design, a finite element analysis was performed on the sandwich plate, as shown in Figure 3-7 through Figure 3-12, using COMSOL. A uniformly distributed loading was applied on the plate to represent the weight of twenty pieces of 4" by 8" concrete cylinders. The result of finite element analysis is shown in Figure 3-13. The result indicates that the maximum von Mises stress is at the lower part of the rods. The value of the maximum stress is approximately 1,600 psi. Since most of the structural components is metal or alloy, von Mises yielding criterion is adopted to verify the mechanical design and to perform design trade on the structural components. Since the yield strength of the threaded stainless-steel rods, often 200 MPa or 29,000 psi, is eighteen times higher than the maximum von Mises stress, the margin is satisfied. The static analysis using finite element

software COMSOL ensures that the automated machine can undertake the dead loads from at least twenty-one pieces of standard 4" by 8" concrete cylinders.

The temperature measuring module used in this study is an integrated system with a programmable resolution 1-wire digital thermometer (model DS18B20) manufactured by Maxim Integrated, along with an Arduino UNO microcontroller. Figure 3-14 shows the electrical wiring of the integrated system. The thermometer is entirely waterproof and is placed at the center of a standard 4" by 8" concrete mold during the manufacturing process of the control specimen. After pouring the fresh concrete mixture into the mold, the thermometer is embedded in the control concrete specimen as shown in Figure 3-15. The thermometer is then connected to the Arduino microcontroller that receives the temperature profile of the control specimen for controlling the freezing and thawing cycles of the climate chamber. Figure 3-16 illustrates the electrical wiring in the freeze-thaw control module, consisting of an Arduino microcontroller, two relays, two linear actuators, and the power supply.
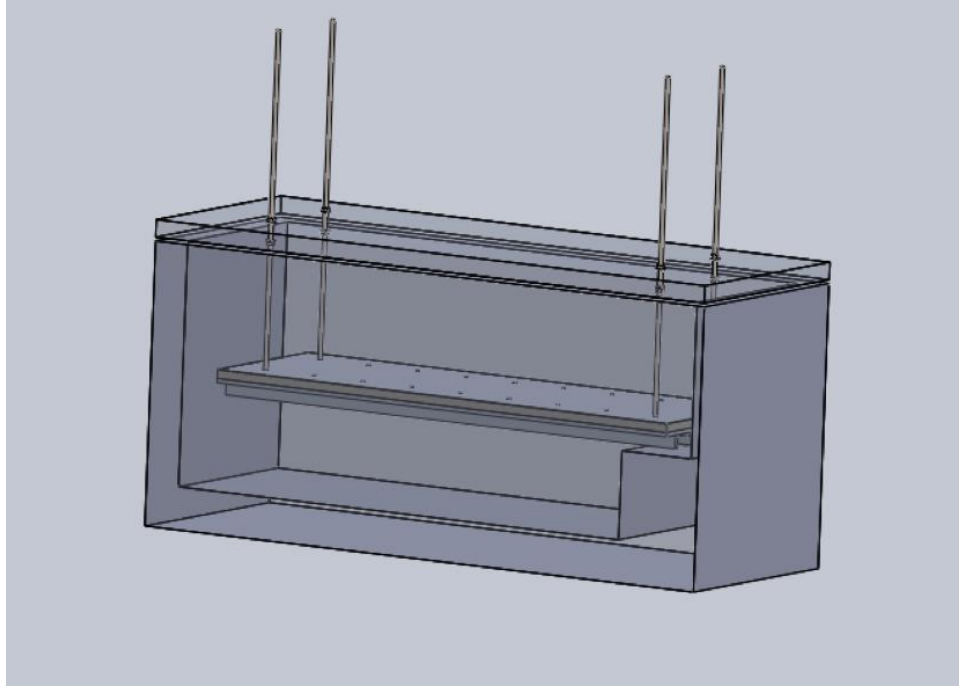
Figure 3-6. The conceptual model of freeze-thaw machine built in SolidWorks.
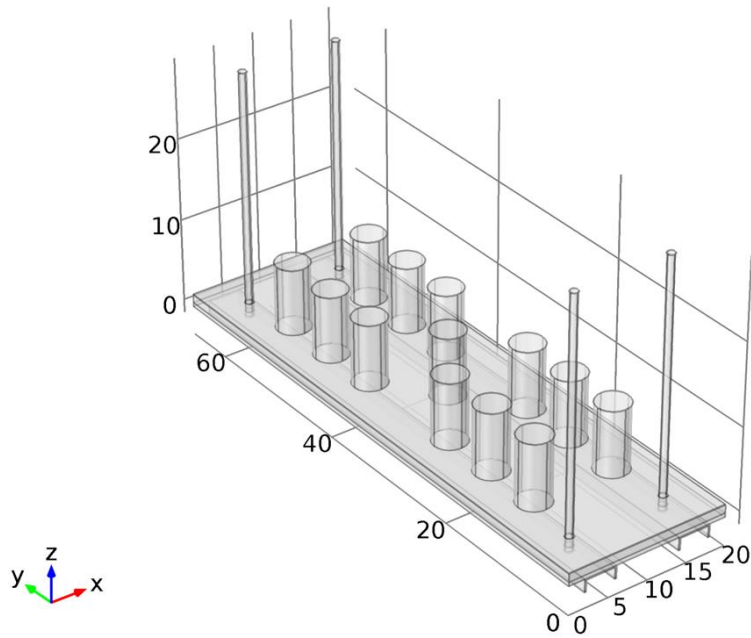
Figure 3-7. The specimen allocation on the sandwich plate in COMSOL.
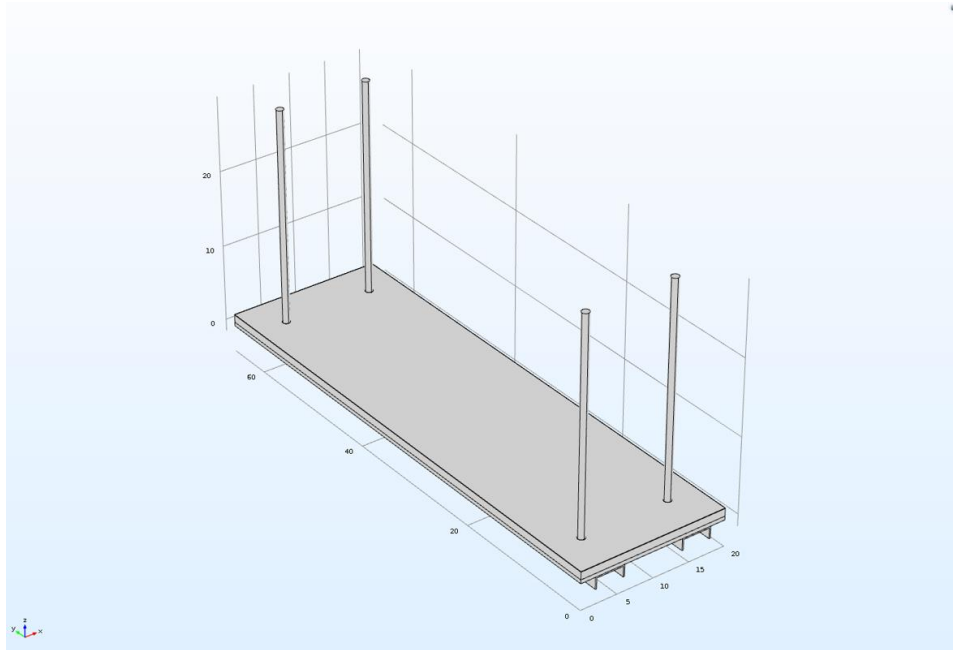
Figure 3-8. The finite element model of the sandwich plate in COMSOL.
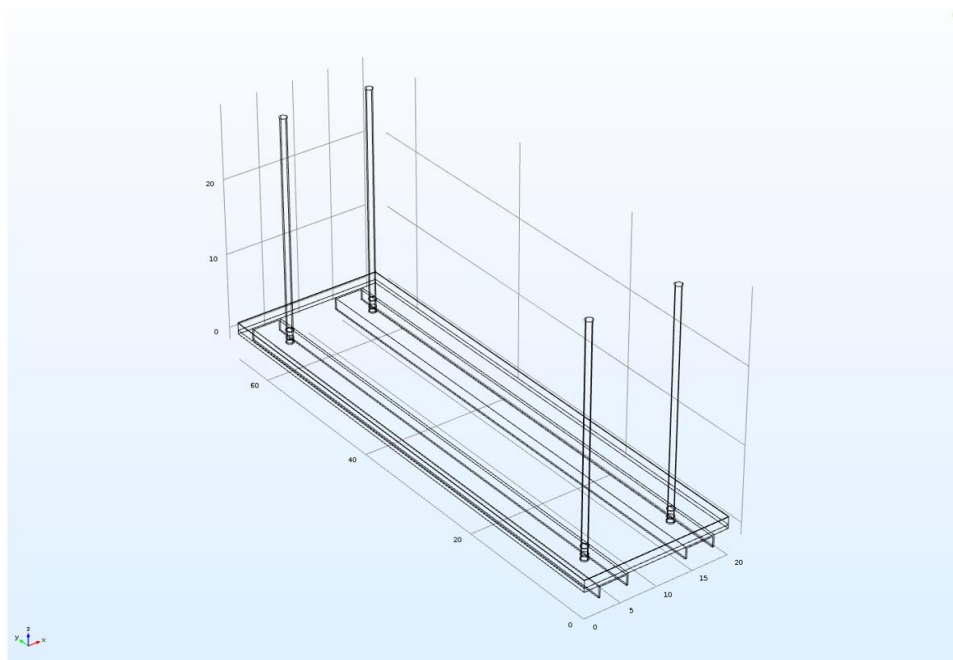
Figure 3-9. The wireframe view of the sandwich plate that are supported by two steel channels.
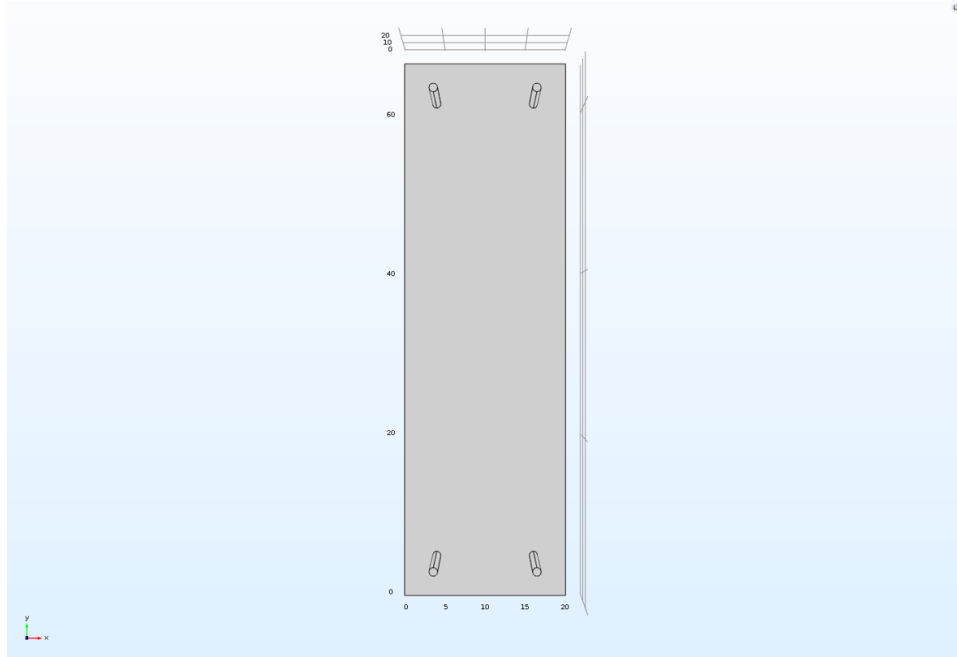
Figure 3-10. The top view of the sandwich plate in COMSOL.
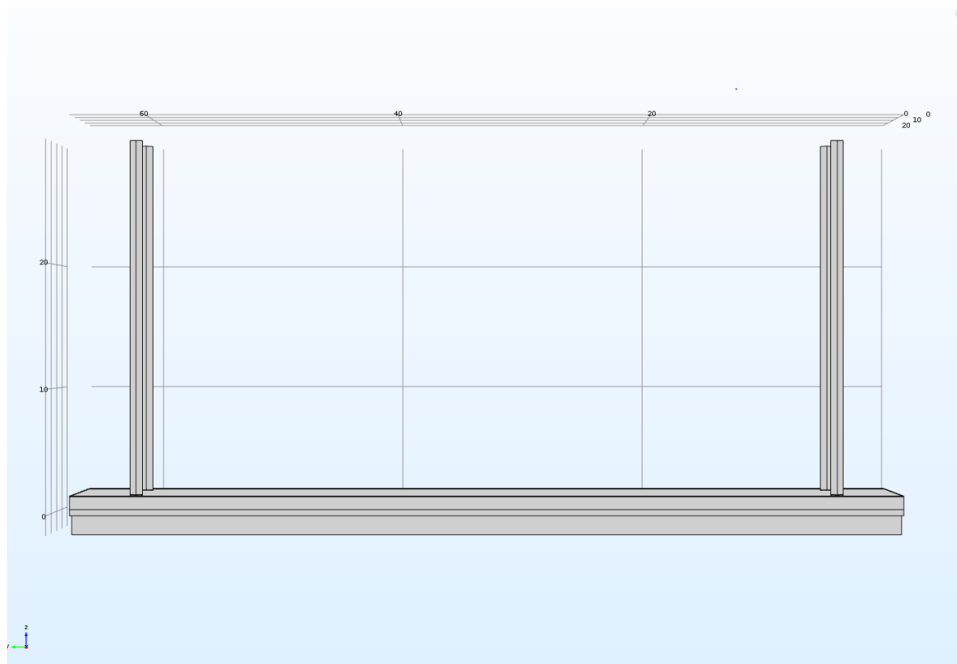
Figure 3-11. The side view of the sandwich plate of the freeze-thaw machine.
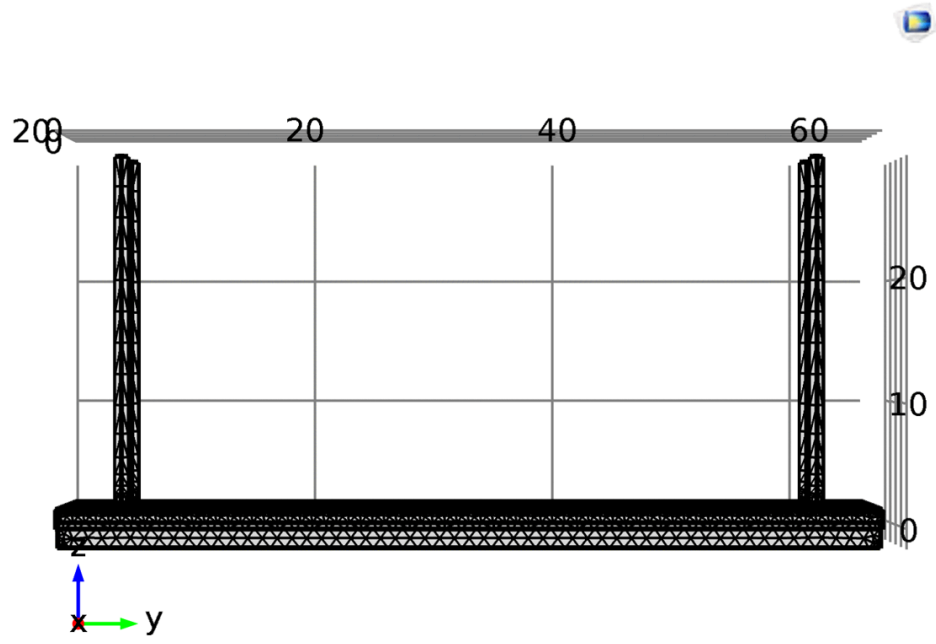
Figure 3-12. The mesh in finite element model of the sandwich plate.
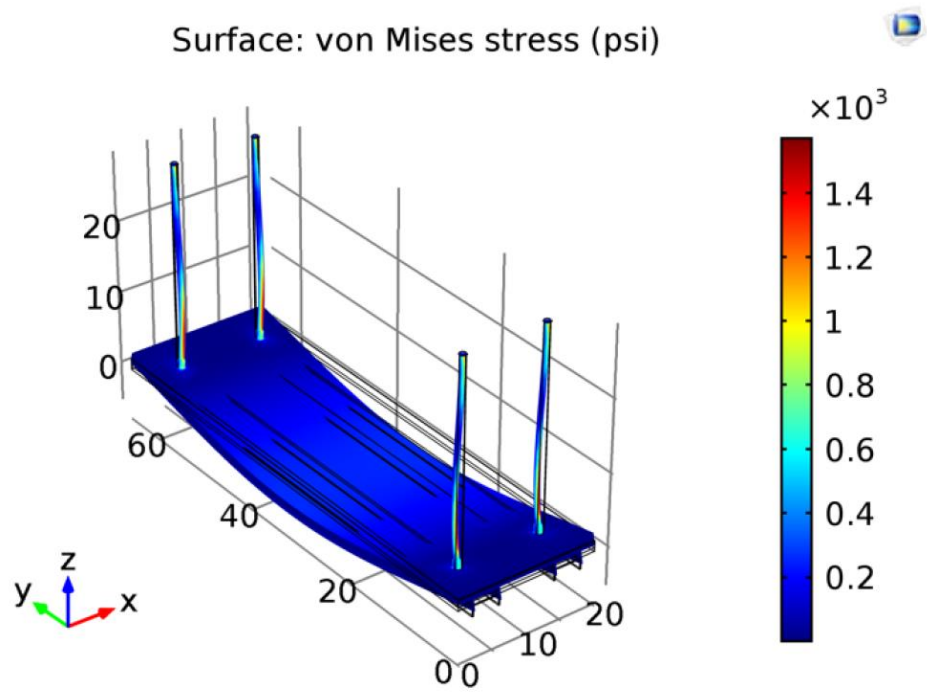
Figure 3-13. The static analysis on the sandwich plate under the dead loads of twenty-one

concrete cylinders. The color bar shows the level of von Mises stress in the structural

components.
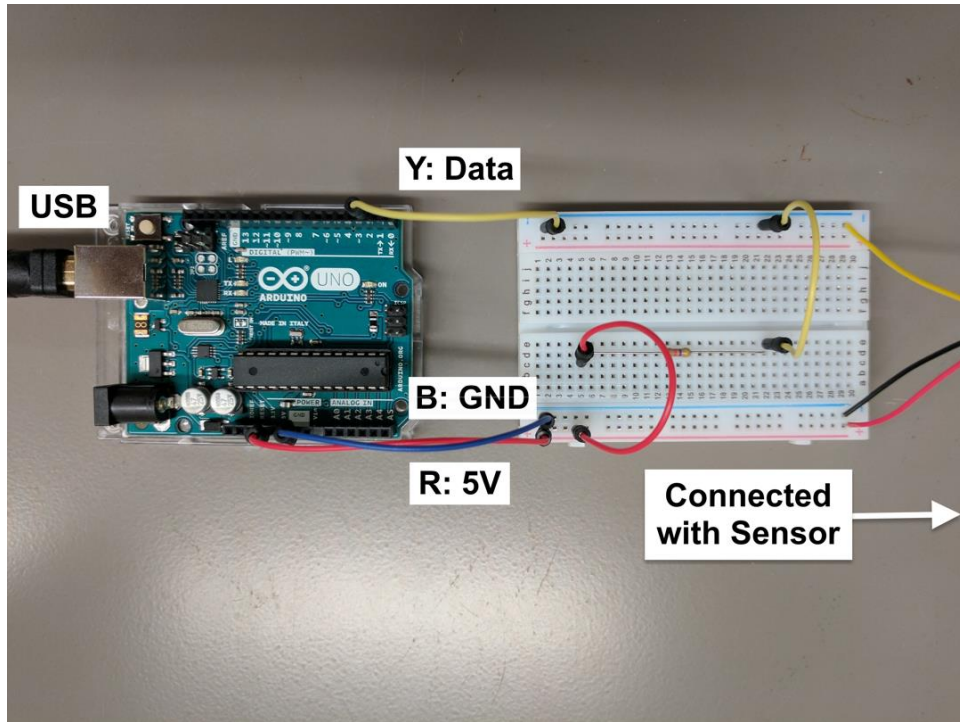
Figure 3-14. The wiring of the integrated thermometer, and the Arduino UNO microcontroller.
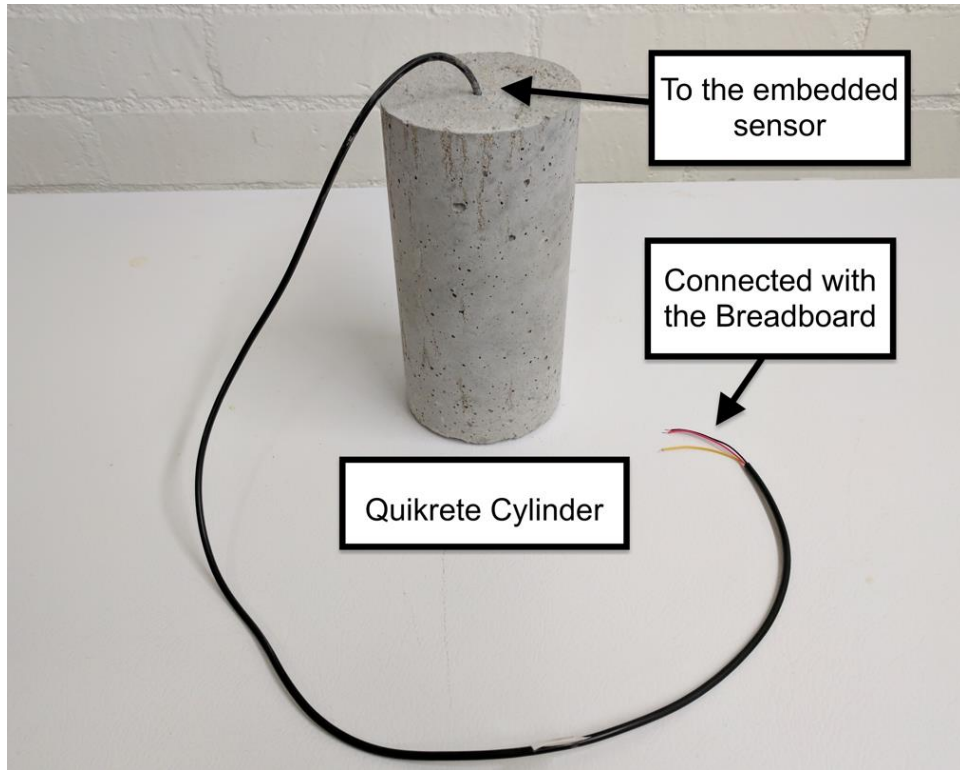
Figure 3-15. The control specimen made of Quikrete concrete mix. The thermometer is

embedded in the center of the specimen.
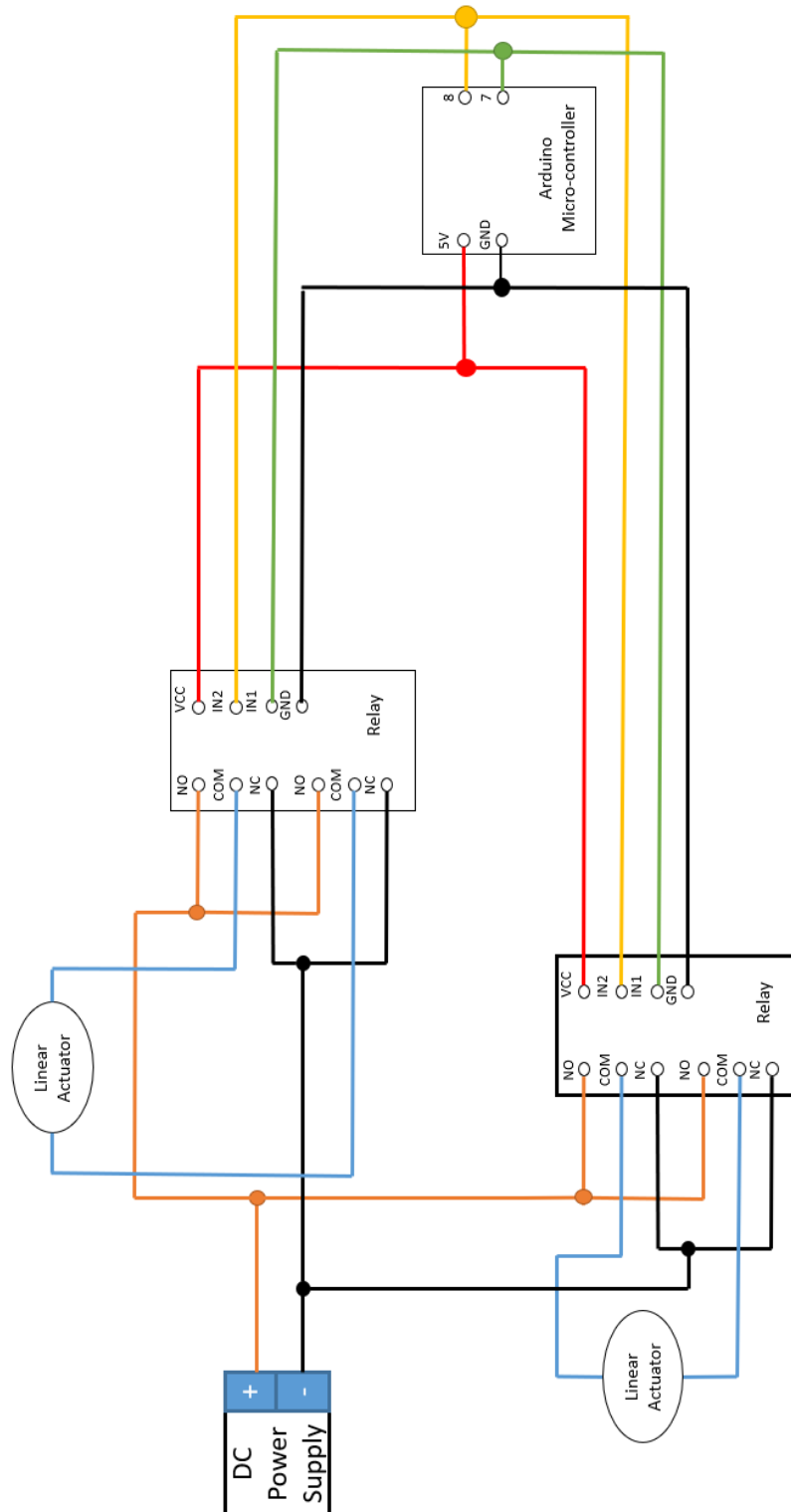
Figure 3-16. The electrical wiring of the freeze-thaw control module of the climate chamber.

3.2.2 Estimation of the Temperature Difference between the Center and the Surface of a Concrete Cylinder

After the freeze-thaw machine was built, it was important to ensure that the concrete specimens could be entirely frozen or, in other words, could reach the designed freezing temperature with the time and the intensity of the applied thermal cycling. It was observed that in the process of the thermal cycling, the surface temperature of a 4" by 8" concrete cylinder could noticeably differ from the temperature at the center of the cylinder at the same moment. Hence, an estimation based on heat conduction was performed to obtain the maximum temperature difference that would occur in the freezing and thawing experiments.

The temperature difference depends on the heat conductivity of the concrete, the cooling and heating rate of the thermal input and output, and the thickness of the concrete. Theoretically, the temperature difference can be approximated by the linear diffusion equation for heat conduction [41].

$$\Delta T = \frac{\dot{T} D^2 \rho}{4 C_0} \qquad (3\text{-}1)$$

where $\dot{T}$ denotes the cooling or heating rate ($°C/h$), D the distance from the center to the surface (m), ρ the specific gravity of the concrete ($\cdot$), C_0 the heat diffusivity (m^2/h). In the freeze-thaw test configuration, a concrete cylinder has the largest distance of 4 inches (or 0.1016 m) from the center to the top of the cylinder and has the highest thawing rate of 3.5°C/hr. Assuming $C_0 = 0.004$ (m^2/h) and $\rho = 3.1$, this would yield the largest temperature difference of 6.9°C in the thawing phase. This estimation shows that the temperature discrepancy can be significant with the

heating rate and the specimen size. A more detailed analysis should be conducted with transient

heat analysis using finite element software Abaqus.

3.3 Ultrasonic Pulse Velocity Test

Ultrasonic pulse velocity (UPV) test was employed to determine the internal damage extent of concrete over the 50 cycles of freeze-thaw action. The measurements were performed in accordance with ASTM C597. This non-destructive testing methodology allows the interrogation of microvoids and microcracks developed in the concrete specimens without permanent influences on their compressive strength. Moreover, this point-like inspection on concrete was adopted to verify the uniformity of the specimens in the presence of the fibers and the PCM particles.

Figure 3-17 (a) exhibits the UPV test apparatus that was used to measure the time taken by a longitudinal pulse wave (P-wave) travelling over a diametrical distance of the concrete cylinder. The source signal is composed of sinusoidal waves with an excitation frequency range from 80 kHz to 150 kHz and a peak amplitude of $10V_{p-p}$ driven by the function generator (SRS DS345). The power amplifier (UTA 3000) was employed to amplify the source signal sent to a piezoelectric transducer for exciting elastic waves in concrete over a considerable distance. In Figure 3-17 (b), the transducer (Digital Wave Corporation model B1025), was placed in contact with the concrete cylinder, pairing with an identical transducer to receive the signal on the other side of the cylinder. The transducers, with a modest size of 9.5 mm in diameter and 12.5 mm in height, have a relatively flat response in a frequency range from 50 kHz to 2 MHz. A special viscoelastic elastomer with excellent conductivity of ultrasonic waves was placed in between the transducers and the circumferential concrete surfaces to improve the local contact conditions. Moreover, a transducer-positioning frame with two load cells was adopted in precision control of the transducer locations and the local contact forces applied upon the transducers. The receiving signal was conditioned by the filter trigger module (FTM 4000) and recorded by a computer with a sampling rate of 6.25 MHz and an accuracy of 0.16 microseconds in the time domain. The transit time of the first arrival

wave was determined by the peak-to-peak time difference between the source and receiving signals, taking an average value from 16 independent measurements. It is worth mentioning that the time delay of the measurement system was accounted for by face-to-face calibration, as illustrated in Figure 3-18. The P-wave velocity can be calculated from the measured transit time by the following expression,

$$c_p = \frac{L_p}{t_p} \qquad (3\text{-}2)$$

where L_p denotes the diametrical length of the specimen, and t_p represents the wave transit time. Weng [42], Ohdaira and Masuzawa [43] have shown that a 1% increase in the moisture content can raise the measured wave velocity by 2%. To ensure consistency, each concrete specimen was air-dried in the laboratory over 4 weeks and was verified that a steady weight was obtained prior to each UPV measurement.

Due to the distributions of fibers and PCM particles, settlement of coarse aggregates, and bleeding effect, the P-wave velocity measured at different locations in a concrete cylinder can vary to a certain extent [44]. Heavier particles in the fresh concrete tend to move toward the bottom of the mold after the placing, thereby rendering a distributed density profile along the height. In addition, inadequate mixing procedures can cause fiber clumping or fiber segregation, which may lead to severe inhomogeneous behaviors of the test results. Therefore, as shown in Figure 3-17(b), the UPV measurements were taken at twenty-eight designated locations on the cylinder to assure the specimen is uniform as expected.

In addition to the P-wave velocity, the internal damage extent of a concrete sample, denoted by $d_{p,N}$, can be quantified by the reduction in the relative dynamic modulus of elasticity (RDM) written in the form:

$$RDM_N = \left(\frac{t_{p,0}}{t_{p,N}}\right)^2 \times 100\% \tag{3-3}$$

$$d_{p,N} = 1 - RDM_N = 1 - \left(\frac{t_{p,0}}{t_{p,N}}\right)^2 \times 100\% \ (0 \leq d_{p,N} < 1) \tag{3-4}$$

where $t_{p,N}$ denotes the P-wave transit time measured in the concrete specimen that has experienced N number of freeze-thaw cycles. Petersen et al. [22] and Hanjari et al. [23] have shown that Eq. (3-3) is sensitive and can be used for the evaluation of the damage inside the concrete elements subjected to successive freeze-thaw cycles.

Beyond 50 freeze-thaw cycles, the internal damage is severe enough that the receiving signal is highly attenuated, rendering UPV measurements unreliable. For concrete deteriorated in higher levels, damage characterization by wave frequency shift or wave attenuation is recommended [45]. Alternatives such as the forced resonance method (ASTM C215) or X-ray computed tomography (CT) [46] are viable. Despite that, UPV method is economic, relatively simple to operate, and works as needed within the current scope.
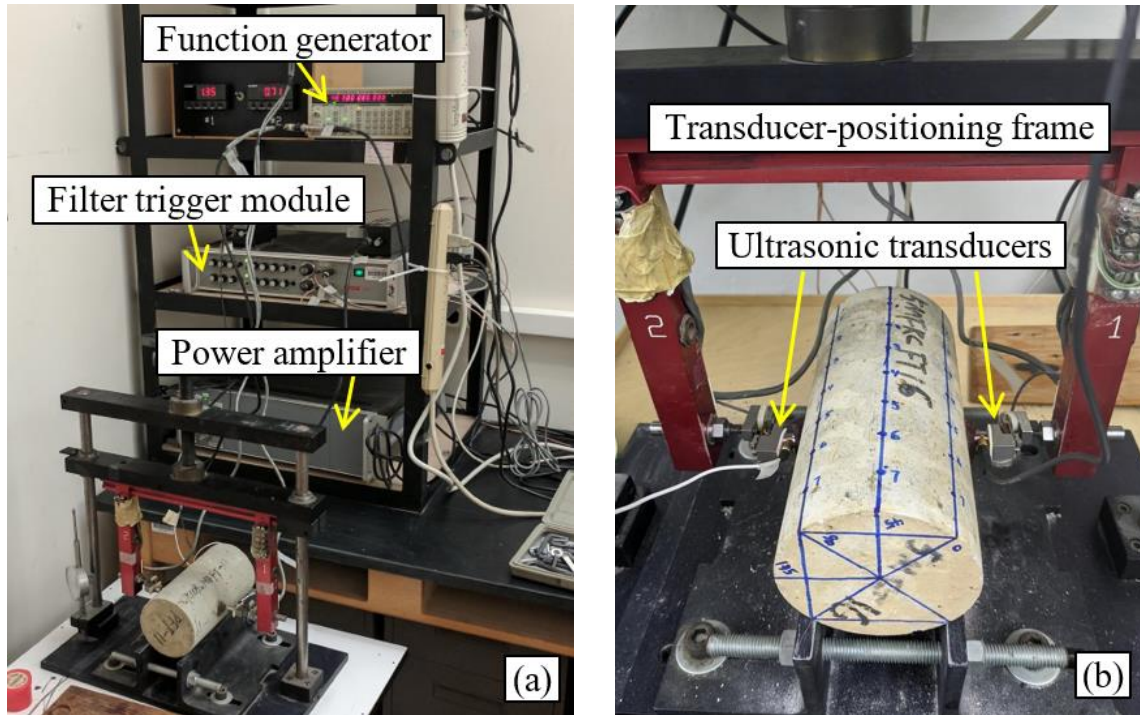
Figure 3-17. The ultrasonic pulse velocity testing program. (a) An overview of the ultrasonic experiment setup. (b) The ultrasonic transducers with the transducer-positioning frame performed accurate alignment to the points (or wave path) of interest on the concrete cylinder.
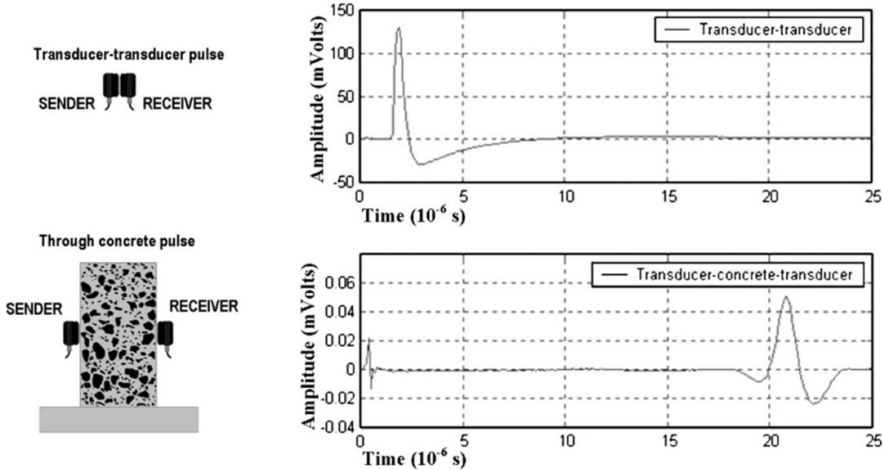
Figure 3-18. Schematic of the face-to-face calibration and the UPV measurment on concrete cylinder [47].

3.4 Uniaxial Compression Test

To investigate the influences of the PCM content on the compressive behaviors of the hybrid fiber-reinforced concrete, uniaxial compression tests were performed on concrete cylinders of 101.6 mm in diameter and 203.2 mm in height, according to ASTM C39. The specimens were manufactured using the mixture proportions in Table 3-2, moist cured at 23°C, capped with hydro-stone gypsum cement, as shown in Figure 3-21 and Figure 3-22,and then tested at the age of 7 days and 28 days. A servo-hydraulic test system with a capacity of 1,000 kN was employed to load the specimens at a steady rate of 0.0127 mm/s. A compressometer with a gauge length of 125.48 mm was instrumented, as illustrated in Figure 3-19, with a linear variable differential transducer (LVDT) in high precision and of excellent repeatability for measuring the displacement of the specimen between the two yokes of the compressometer. A LabVIEW-based data acquisition system was used to record the load-displacement data for determining static modulus of elasticity and compressive strength of the specimen. To consider the nonlinearity in the compressive stress-strain curve of concrete, the chord modulus of elasticity can be determined using the following relation (ASTM C469):

$$E = \frac{(\sigma_2 - \sigma_1)}{(\epsilon_2 - 0.00005)} \tag{3-5}$$

where σ_1 denotes the stress at 50 millionths of strain. σ_2 and ϵ_2 are the stress and strain corresponding to the 40% of compressive strength, respectively.

To assess the accumulated damage from the freeze-thaw test, the compressive strength and static modulus of elasticity were determined and compared for the specimens subjected to 50 freeze-thaw cycles and the specimens without weathering using the identical test setup. To account

for the strengthening effect of continuous hydration of cement, it is required for the non-weathered specimens to be submerged in water for an extended period of time to allow reliable comparisons. Since the hydration reactions primarily occur at temperatures above water freezing point, unlike previous researchers, only the thawing period of all cycles should be considered to estimate the effective submersion time for the control specimens:

$$t_s = \left(\frac{t_T}{t_T + t_F}\right) \cdot \left(\frac{N}{f_{FT}}\right) \tag{3-6}$$

where t_T and t_F are the thawing and freezing periods in one cycle, respectively. N is the number of the freeze-thaw cycles, and f_{FT} denotes the frequency of the applied freeze-thaw action. In this work, the concrete cylinders were subjected to freeze-thaw action at a steady rate of 1 cycle/day for 50 days. There was a 10-hour thawing and a 14-hour freezing in each cycle. Therefore, the control specimens were designed to be submerged in water for 21 days before compression test.

For the evaluation of the freeze-thaw damage on the concrete specimens, the damage variables representing the freeze-thaw damage to the compressive strength and the static modulus of elasticity can be individually determined by the following expressions:

$$d_{f,N} = 1 - \frac{f_{c,N}}{f_{c,0}} \quad (0 \leq d_{f,N} < 1) \tag{3-7}$$

$$d_{E,N} = 1 - \frac{E_{c,N}}{E_{c,0}} \quad (0 \leq d_{E,N} < 1) \tag{3-8}$$

where $f_{c,N}$ and $E_{c,N}$ denote the compressive strength and the chord modulus of elasticity, respectively, for the concrete specimen that have experienced N number of freeze-thaw cycles. In

Figure 3-20, the two damage variables are related to the damaged and undamaged stress-strain

curves to articulate the concepts.
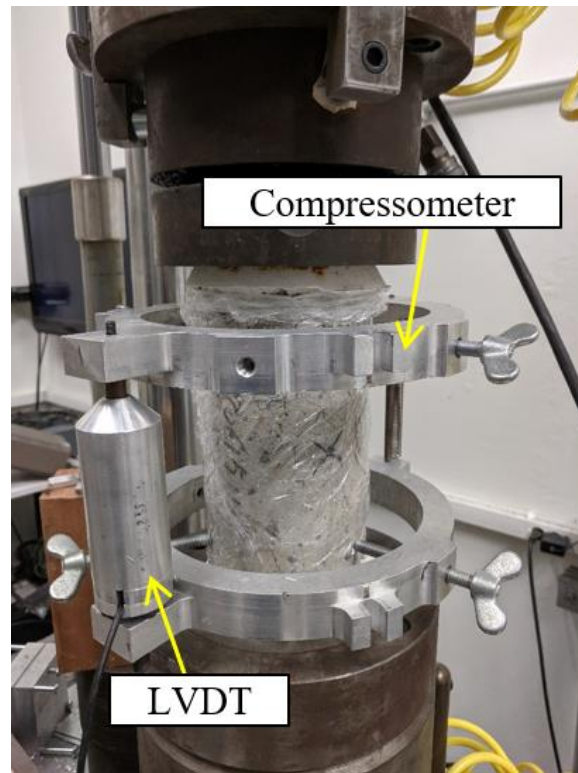
Figure 3-19. Instrumentation of the compressometer with a linear variable differential transducer

(LVDT) for a direct measurement of the axial deformation of the cylindrical specimen.
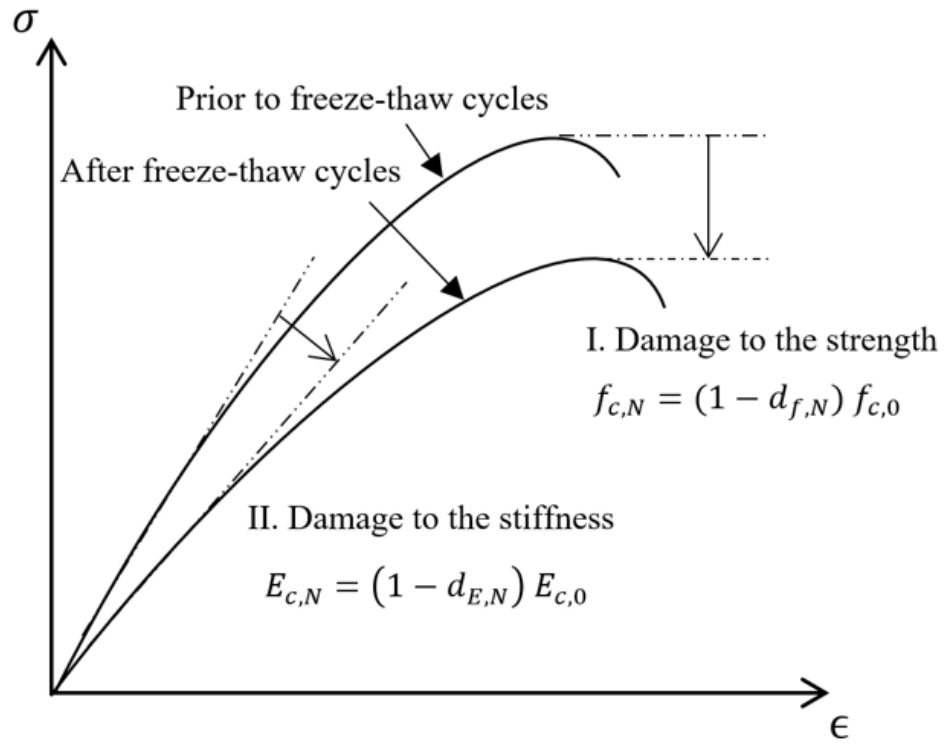
Figure 3-20. Schematic of the relations between the two damage variables and the damaged and undamaged compressive stress-strain curves.

Figure 3-21. The capping of concrete cylinders using hydro-stone gypsum cement.

Figure 3-22. The capping process in the structural laboratory.

3.5 Three-point Bending Test

3.5.1 Flexural Tensile Behaviors of Fiber-reinforced Concrete

To evaluate the effects of adding the phase change material (PCM) on the concrete flexural behaviors, three-point bending tests were conducted on prismatic specimens of dimensions in 4 x 4 x 14 in^3 (or 101.6 x 101.6 x 355.6 mm^3) with a notch in 4 x 1 x ½ in^3 (or 101.6 x 25.4 x 12.7 mm^3) at the midspan, using the servo-hydraulic test system with a capacity of 1,000 kN. Figure 3-23 exhibits the three-point bending test setup. Two rollers were placed 12 inches apart under the prismatic specimen. The loading was applied at the midspan with a steady rate of 0.0015 in/s (or 0.0381 mm/s). A linear variable displacement transducer (LVDT) is instrumented at the notch tip to measure the crack tip opening distance (CTOD) as illustrated in Figure 3-24. A LabVIEW-based data acquisition system was used to record the load-midspan deflection data and the load-CTOD data for determining the peak load, the fracture energy, the equivalent flexural tensile strength, and the residual flexural tensile strength of the hybrid fiber-reinforced concrete beams with distinct PCM dosages.

3.5.2 Fracture Energy

According to RILEM TC 50-FMC and Malvar and Warren [48] the fracture energy of a prismatic beam can be determined by the following expression,

$$G_f = \frac{U_0 + mgd_0}{A} \tag{3-9}$$

where U_0 is the area under the load-midspan deflection curve. mg denotes the weight of the specimen. d_0 is the midspan deflection at fracture, and A is the cross-sectional area of the

specimen at the notch. It appears that the mgd_0 term is to remove the energy in lifting the specimen. It has been verified that the gravitational effect is not pronounced in the fracture energy for the specimens tested in this study. Therefore, the gravitational term in the expression is not considered in the following context.

3.5.3 Equivalent and Residual Flexural Tensile Strength

The flexural behaviors of concrete can be considerably affected by the addition of fibers and the phase change material (PCM). For instance, the flexural tensile strength is significantly increased by the fibers, because of the crack bridging capability of the fibers. The fibers obstruct the propagation of microcracks in the harden cement paste, thereby hindering the formation of macrocracks. After the first crack, which is the onset failure of the harden cement paste, the fibers carry most of the tensile stress in the concrete and play an important role in the post-peak behaviors. Therefore, it is crucial to determine the residual strengths at various deflections after the peak load to characterize the capability of the added fibers on resisting the flexural tensile stress. In RILEM TC 162-TDF, the residual flexural tensile strength can be obtained using the following formula,

$$f_{R,i} = \frac{3}{2} F_{R,i} \left(\frac{L}{b\, h_{sp}^2} \right)$$
(3-10)

where h_{sp} is the height of the beam excluding the length of the notch. L is the span between two rollers in the three-point bending test (mm). b denotes the width of the specimen (mm). $F_{R,i}$ signifies the load at a specific crack mouth opening distance (CMOD).

Alternatively, the equivalent flexural tensile strength gives an averaged flexural tensile strength up to a specified deflection. Assuming a linearly distributed bending stress across the depth of the beam, the equivalent flexural tensile strength can be expressed as:

$$f_{eq,i} = \frac{3}{2}\left(\frac{D_{BZ,i}^f}{\delta_i}\right)\left(\frac{L}{b\,h_{sp}^2}\right) \tag{3-11}$$

Where δ_i is the midspan deflection of a specific point. D_{BZ}^f denotes the energy absorption capacity up to the midspan deflection of δ_t.

3.5.4 Relationship between CTOD and CMOD

The measurement of the crack mouth opening distance (CMOD) requires a displacement sensor instrumented below the beam. Since the CMOD is larger than CTOD when the beam is under three-point bending, it often requires a LVDT with a larger capacity, and the risk to break the LVDT during the test is much higher. Therefore, the CTOD measurements are taken and the results are converted to the CMOD.

To obtain the equivalent flexural strength, a relationship between the crack mouth opening distance (CMOD) and the CTOD is needed. This relationship can be found in RILEM TC 162-TDF, and is provided in the following,

$$\text{CTOD} = \text{CMOD}\frac{(H - h_{notch})}{H} \tag{3-12}$$

where H is the height of the beam, and h_{notch} is the height of the notch.

3.5.5 Reinforcing Index

The capability of fibers to enhance the flexural tensile behaviors of concrete is dependent on the aspect ratio, fiber content, and the tensile strength of the fiber [49]. The beneficial effect of adding fibers can be attributed to the anchorage force provided by the fibers and the bond strength between the harden cement matrix and the fibers. To extend this concept for the hybrid fiber-reinforced concrete containing phase change material (PCM), the following reinforce index is proposed,

$$RI_i = (1 - V_{f_{PCM}}) \frac{V_{fi} k_i l_i}{di} \left(\frac{f_{ti}}{f_{ts}}\right)^a \tag{3-13}$$

$$RI = \sum RI_i \tag{3-14}$$

where $V_{f_{PCM}}$ is the volume fraction of the added PCM. The suffix i denotes the i type of the added fiber. V_{fi} is the volume fraction of the fiber. k_i is the bond factor of the fiber. l_i is the length of the fiber. di is the diameter of the fiber. f_{ti} is the tensile strength of the fiber. f_{ts} is the tensile strength of the steel fiber. a is the tension stiffness parameter, which can be taken as 0.5 [49].

Figure 3-23. The three-point bending test setup with the servo-hydraulic machine and the prismatic

concrete specimen.
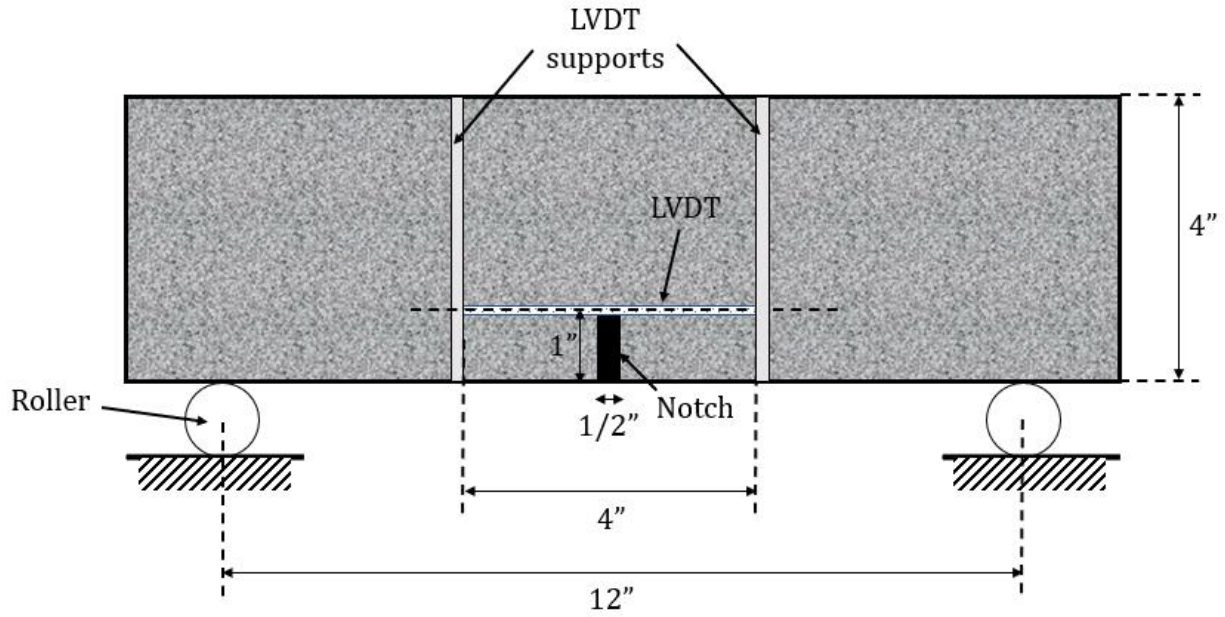
Figure 3-24. The illustration of three-point bending test for the notched beam specimen.
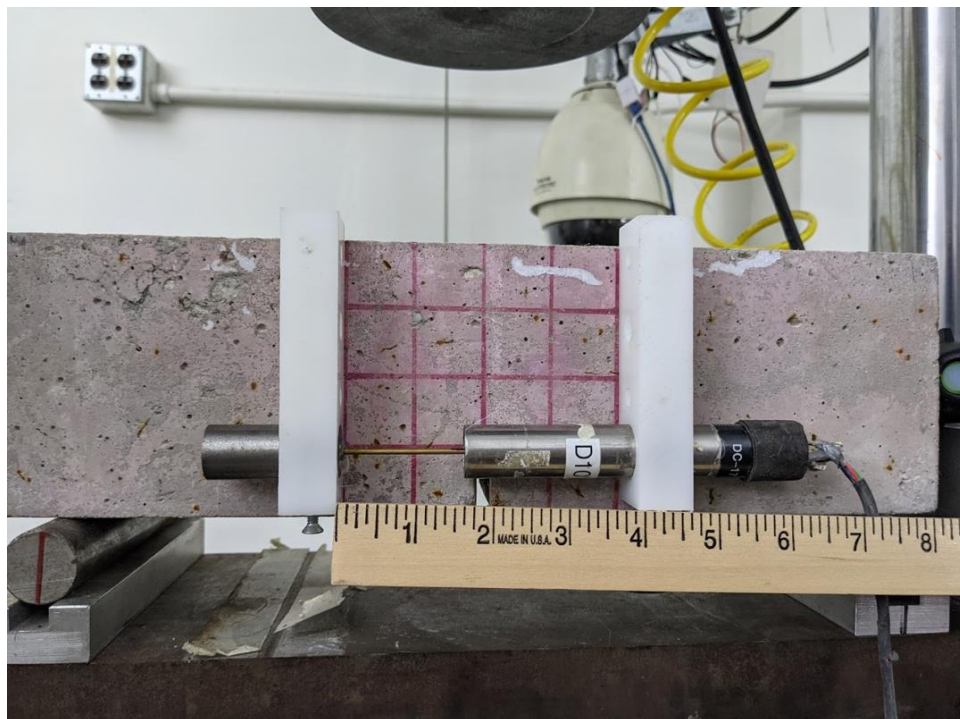
Figure 3-25. The instrumentation of LVDT to measure the crack tip opening distance.

3.6 Digital Image Correlation Technique

The digital image correlation (DIC) technique is an exploratory displacement measuring approach for capturing the crack propagation process during the three-point bending test. A reliable and reproducible DIC results should include deploying a speckle pattern that is of randomness, in a reasonable pattern feature size and consistent density for each specimen. A variation coefficient of 0.75 is selected for a satisfactory efficiency to accuracy ratio. The pattern feature size is 0.013" (or 0.336 mm), which is equivalent to 5 pixels in the equipment and the specimen settings. The speckle pattern is transferred to the concrete by using film-free decal sheets with proper setting solution. Figure 3-26 illustrates the speckle pattern on the side of the notched beam specimen. The camera on Pixel 4XL is used to take images in the ratio of 4 by 3, with a resolution of 4032 x 3024. The camera is fixed on a 5.1" height tripod stand with a remote controller for taking photos without touching the camera. The camera is set approximately 12 and ½" apart from the specimen. The image scale is approximately 380 pixels per inch (or 15 pixels/mm).

Ncorr [50], the open source 2D-DIC MATLAB software, is adopted to control the parameters of the speckle pattern and to generate the image of the speckle pattern. Figure 3-27 displays the parameters used in the software. The subset radius is set as small as possible without causing noisy displacement data. The subset radius requires some iterations to find an optimal value since mostly it is based on heuristics and observations. The subset spacing directly affects the computational cost and the resolution of the results. The high strain analysis feature is turned on to avoid distorted displacement field around the crack tip. The elapsed time for analyzing 1 image with current setting is approximately 75 seconds in a mock test with hydro-stone plate. The strain radius is the radius of a circle formed by a group of displacement data points to fit a plane

using least square method. This plane is used to find the displacement gradients and compute the

Lagrangian/Eulerian strain of the representative circle. After some iterations, a strain radius of 15

is used to balance the resolution and noises in the strain results. In Figure 3-28, a mock test has

shown satisfactory bonding between the speckle pattern and the cement-like surface (hydro-stone).
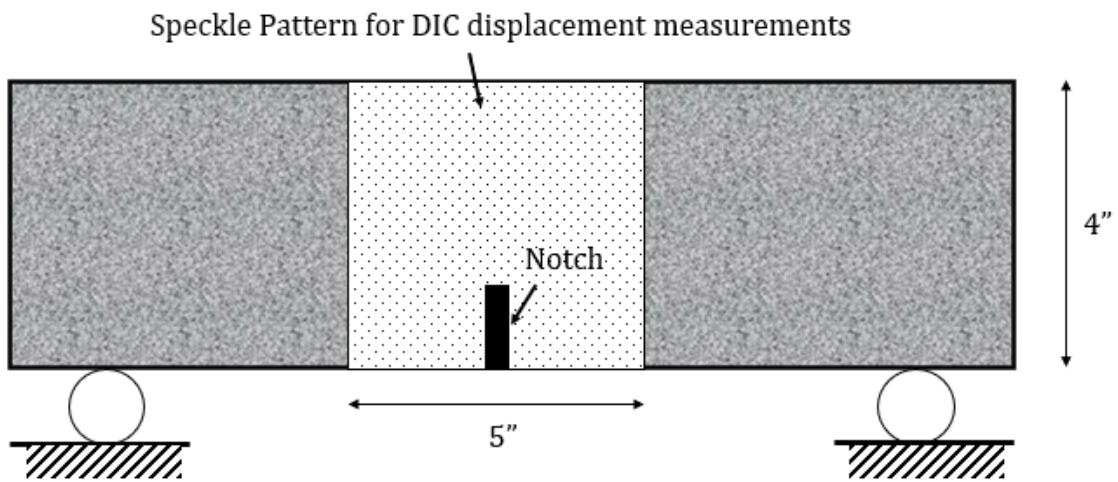
Figure 3-26. The illustration of the DIC speckle pattern on a side of the prismatic specimen.
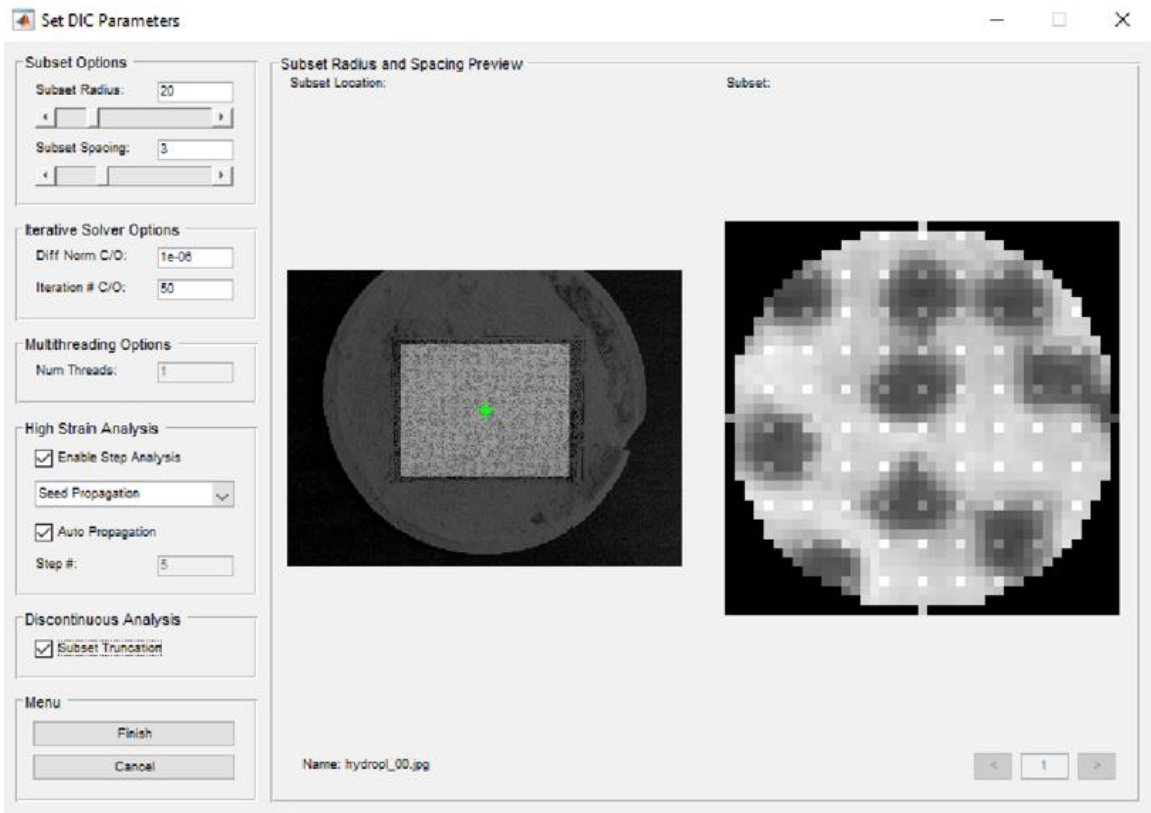
Figure 3-27. The DIC parameters setup in Ncorr software.
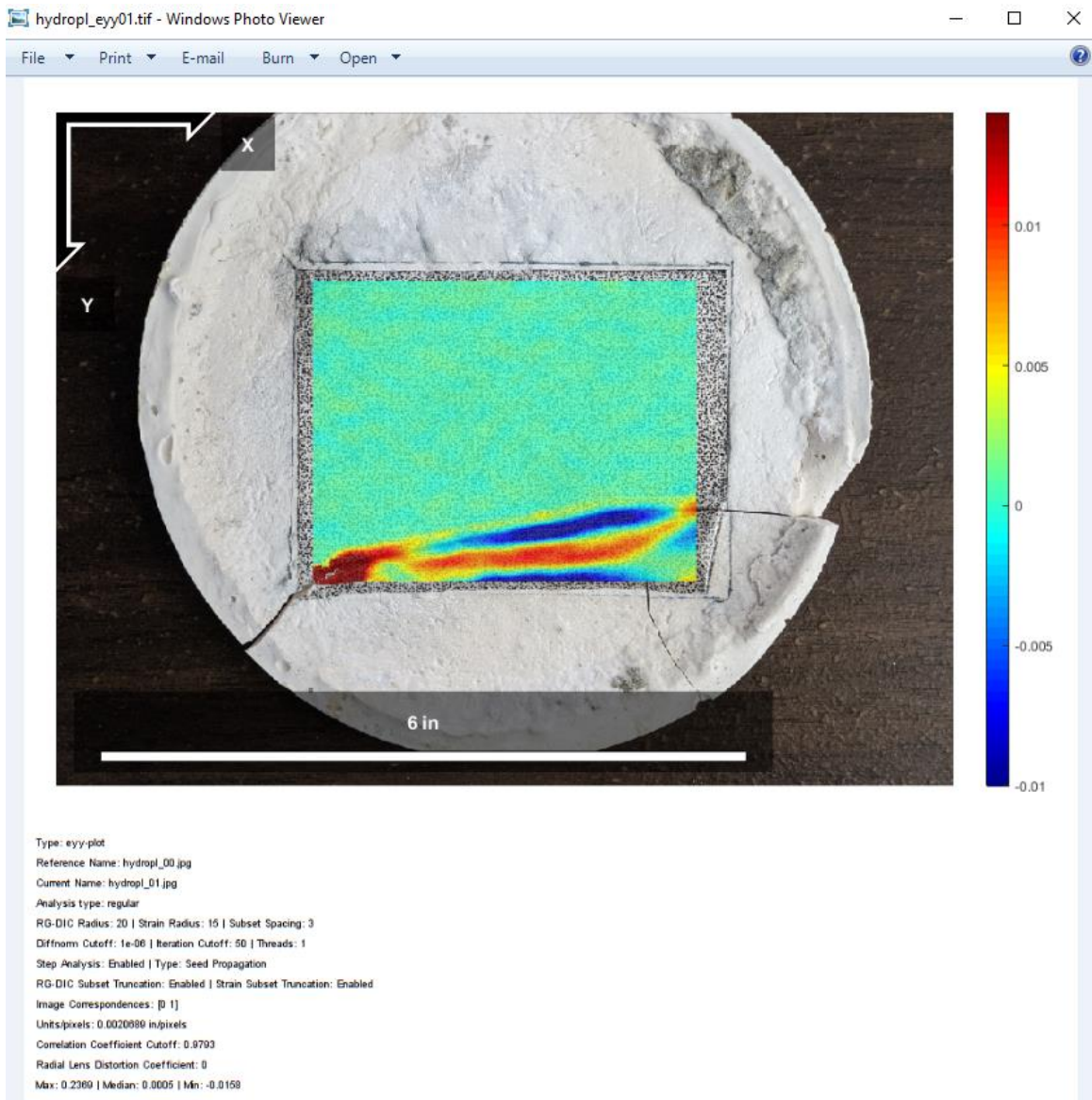
Figure 3-28. A trial test of the digital image correlation (DIC) on a hydro-stone plate.

Chapter 4 Investigations into the Freeze-thaw Damage and the Compressive Behavior of Hybrid Fiber-reinforced Concrete Containing Phase Change Material

4.1 Test Procedures

The present research is developed to investigate the impacts of PCM dosage on the freeze-thaw durability and compressive behaviors of concrete. The complete testing program and the outcomes to be reported are summarized in Figure 4-1. The concrete mix proportions are designed with varying volume fractions of PCM. The hybrid fiber, inclusive of the steel fiber and the polyvinyl alcohol microfiber, is mixed with a constant dosage. Uniaxial compression tests are performed on the concrete cylinders to evaluate the strengths at the age of 7 days and 28 days. The specimens are subjected to continuous freeze-thaw cycles with a tailor-make freeze-thaw machine in a controlled environment. After the freeze-thaw weathering, the compressive strength and the static modulus of elasticity are determined for each specimen and compared with the values measured prior to the cycles for the freeze-thaw damage evaluation. Moreover, the changes in the relative dynamic modulus of elasticity, which is indicative of the internal damage extent of concrete, are obtained by ultrasonic pulse velocity tests over the freeze-thaw cycles. The experimental results will show that the added hybrid fiber considerably increases the compressive strength of concrete and sufficiently compensates for the strength loss due to the addition of PCM; the incorporation of the hybrid fiber and the PCM contribute to different aspects of the freeze-thaw durability (i.e., internal and superficial), at least to a different degree.

.

Figure 4-1. The flow chart of the complete test program with cylindrical specimens.

4.2 Surface Conditions after Freeze-thaw Weathering

To investigate the influence of adding phase change material (PCM) microcapsules on the surface durability of concrete under freezing and thawing, the concrete specimens with a PCM dosage varying from 0 to 7% by volume are subjected to 30 freezing and thawing cycles. The surface durability is considerably affected by the presence of microcracks. The micro-scale cracking on the surface of concrete can cause the removal of a layer of concrete skin, and thus facilitates the ingress of aggressive chemicals resulting in various types of concrete deterioration. It is worthwhile to mention that the freezing and thawing tests are performed without using any saline solutions. Therefore, freeze-thaw weathering is the sole contribution to the micro-scale cracking on the surfaces of the concrete specimens.

Figure 4-2 illustrates the surface conditions of the concrete specimens after 30 cycles of freezing and thawing. Since there is no substantial difference for the specimens in the same composition, one specimen in each type of mixture is reported. It is observed that the plain concrete is severely damaged, with the coarse aggregates mostly visible over the entire surface. The concrete specimens with the hybrid fiber, as shown in Figure 4-2 from (b) to (d), exhibit superior surface durability compared with the plain concrete.

Table 4-1 provides the qualitative assessment of the surface damages using the visual rating in ASTM C672, giving the damage scales from 0 (without cracking) to 5 (with coarse aggregate mostly visible over the entire surface). The damage scale 1 denotes the cracking is less than 3 mm in depth from the surface. The observations for the concrete specimens without PCM microcapsules are consistent with the findings for fiber-reinforced concrete using one type of

microfibers [12], [13], [51]. In this study, it is confirmed that the added polyvinyl alcohol (PVA) microfiber retains its capacity in the hybrid form with the steel fiber.

Furthermore, as can be seen in Figure 4-2 (c) and Figure 4-2 (d), a detrimental effect of adding PCM on the surface durability is noted within 30 cycles of freezing and thawing. Two effects are potentially responsible for the observed surface damage. First, adding PCM microcapsules evidently increases the porosity of concrete [7], [52]. Pigeon et al. [53] have shown that the surface damage of concrete due to freeze-thaw weathering is strongly connected with the porosity at the surface layer of concrete. Second, the presence of the PCM microcapsules can be detrimental to the proper functioning of the added PVA microfibers. Since the PVA microfibers and the PCM microcapsules have matching scales in diameter, the impact of PCM particles on the microfibers is non-negligible if they are in contact. Furthermore, since the PVA microfibers and the PCM microcapsules are both hydrophobic, there is no appreciable cohesion between the two materials. The microfibers are, therefore, fail to fully carry the loading from the cement matrix, leading to the freeze-thaw cracking on the surface of the hybrid fiber-reinforced concrete after 30 cycles.

Figure 4-2. Surface conditions after the 30 cycles of freeze-thaw exposure: (a) plain concrete, (b) hybrid fiber-reinforced concrete, (c) hybrid fiber-reinforced concrete with a 5% PCM content, and (d) hybrid fiber-reinforced concrete with a 7% PCM content.

Table 4-1. The visual ratings on the surface damages of concrete after 30 freezing and thaw cycles.

Mixture type	PC	HFRC	M5-HFRC	M7-HFRC
Surface damage scale	5	0	1	1

4.3 Ultrasonic Pulse Velocity Test Results

4.3.1 Verification of Specimen Uniformity with P-wave Velocities

This verification of uniformity is made on a concrete cylinder containing 1% of steel fibers, 0.1% of PVA fibers, and 5% of PCM microcapsules (M5-HFRC), using the ultrasonic P-wave velocities calculated from Eq. (3-2). Figure 4-3 shows the specimen and the experiment setup of UPV test. The homogeneity of the specimen is critical for the concrete to achieve the desired mechanical performance. As illustrated in Figure 4-4 (a), twenty-eight sets of ultrasonic measurements are taken on the curved side of the cylinder, including four diametrical measurements, approximately 45 degrees apart, at each height. It is worth to mention that reversing the wave propagation direction yields a negligible difference in the wave velocity.

Figure 4-4 (b) shows the variations of P-wave velocity through the concrete specimen (D = 101.6 mm; L = 203.2 mm). It is observed that the change in wave velocity over the height is less than 6.7%. In fact, Popovics et al. [44] reported that the velocities would differ by as much as 25% between the top and bottom layer for a typical concrete cylinder with internal segregation. Therefore, the gravitational effect on the distributions of the fibers, the PCM particles, and the aggregates is marginal in the M5-HFRC specimen. Moreover, there is no appreciable changes in wave velocity at any measuring angles. The concrete specimen appears to be uniform to a satisfactory degree. The fiber clumping is not detected in the specimen. In addition, the P-wave velocities measured at the middle circumference of the cylinder appear to be more consistent, and close to the average of measured wave velocities. Therefore, the measurement at the middle circumference is employed as the reference points for the internal damage detection in the

(a)

following context.

81
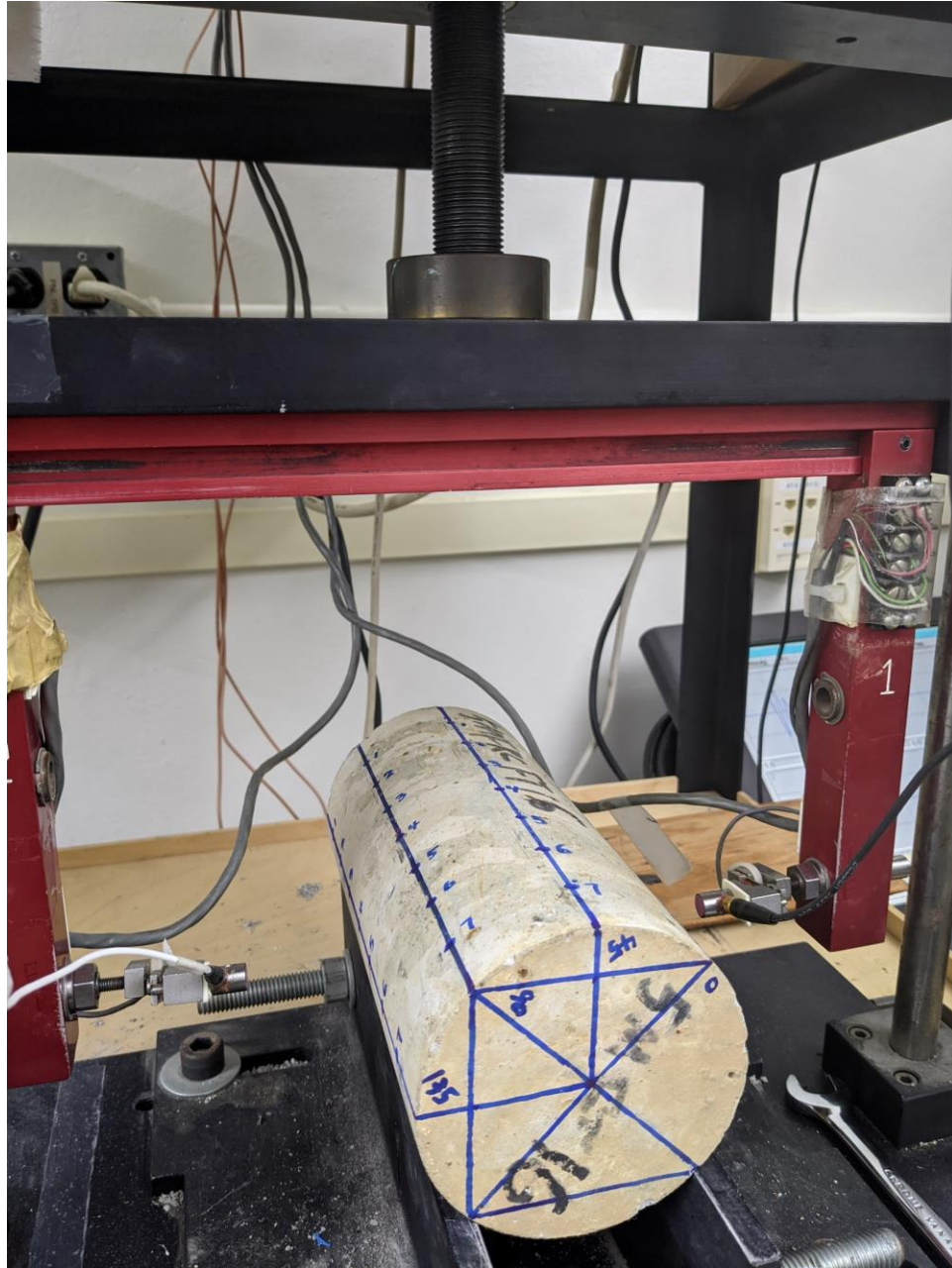
Figure 4-3. The M5-HFRC specimen and ultrasonic pulse velocity test setup.
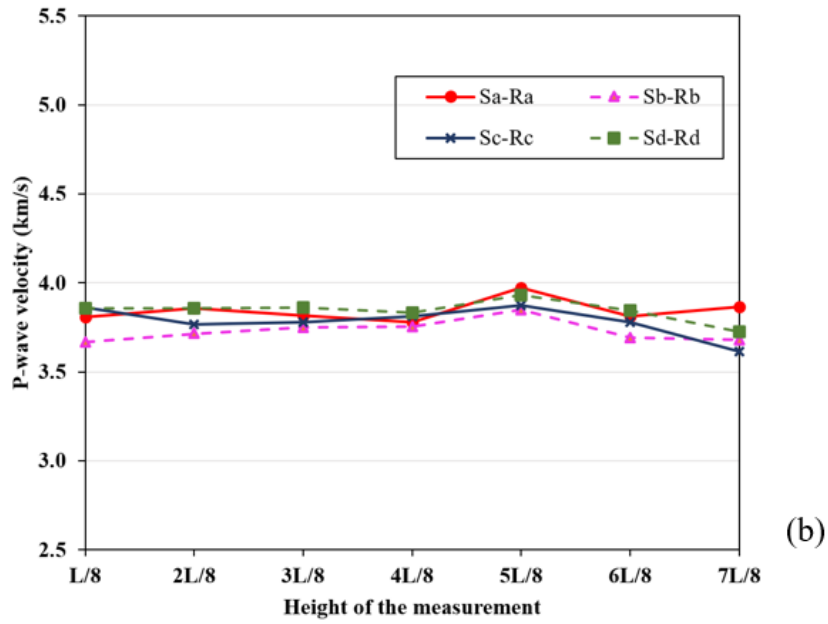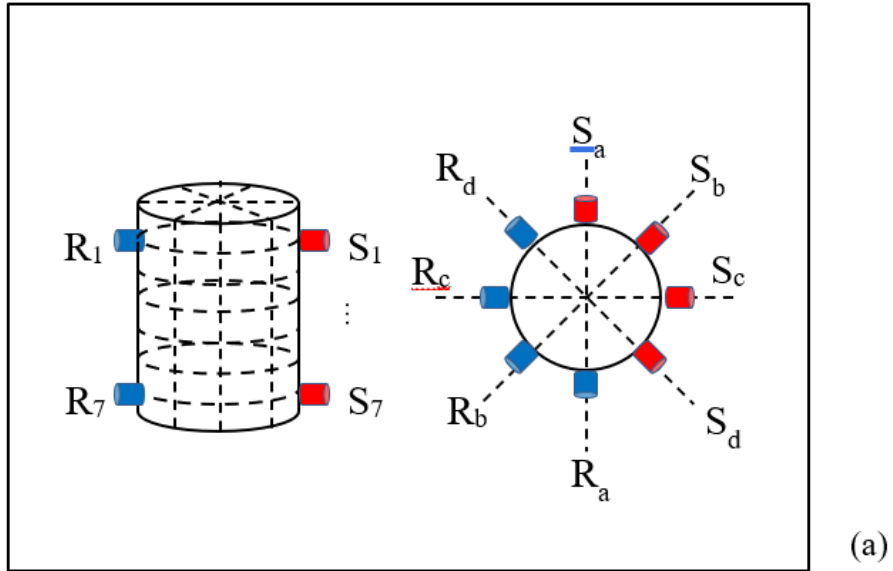
Figure 4-4. Verification of the uniformity of the M5-HFRC cylinder (d = 101.6 mm; L = 203.2 mm) with UPV tests. (a) Schematic of the transducer locations on the specimen. (b) Variations of P-wave velocity over the height of the specimen.

4.3.2 Relative Dynamic Modulus of Elasticity

Table 4-2 provides a summary on the P-wave velocities in the plain concrete and the fiber-reinforced concrete specimens with varying PCM contents, as presented in Table 3-1, prior to the freeze-thaw weathering. The P-wave velocities are individually obtained from the average of sixteen independent measurements at the middle circumference of the specimens. For each composition, three specimens are tested. It can be observed that the P-wave velocities are substantially higher for the concretes with the hybrid fiber. Since the wave speed is proportional to the square root of the stiffness, the higher wave speed can be mainly attributed to the high stiffness of the added steel fibers. On the contrary, the effective stiffness of the PCM microcapsules, composed of 90% paraffine and 10% melamine formaldehyde, is considerably lower than the replaced fine aggregates. Therefore, the P-wave velocity is decreased with the increased PCM content. It should be noted that the measuring locations on each specimen are marked for the positioning of subsequent measurements that monitor the change in wave transit time in the concrete over 50 freeze-thaw cycles.

Figure 4-5 reveals the influence of successive freeze-thaw cycles on the relative dynamic modulus of elasticity (RDM) for the fiber-reinforced concrete specimens with distinct PCM contents, varying from 0, 5, to 7% by total volume. It is not feasible to obtain the result for the damaged PC due to specimen disintegration after 30 freeze-thaw cycles; see Figure 4-2 (a). Under this damage extent, the receiving ultrasonic signal is highly attenuated. RILEM TC 167 [54] has referred this degree of damage to failure. From the results of Figure 4-5, no damage up to slight damage can be observed for concrete with the added hybrid fiber and the PCM. In particular, the 5% addition of PCM yields the highest freeze-thaw durability up to 7% PCM content. The scatter of the results is higher for freeze-thaw damaged concrete than for the undamaged concrete. This

can be noted from the standard deviations in the plot. For M5-HFRC and M7-HFRC, the increased RDM percentage is attributable to the water intake of the concrete specimens during the freeze-thaw experiment, which will gradually vanish as the experiment proceeds with more freeze-thaw cycles [23]. In addition, a 5.2% decrease in RDM is observed for M7-HFRC after subjected to 50 freeze-thaw cycles. This can be related to the increased initial damage associated with the addition of PCM microcapsules. Since a similar trend is observed in the compression test results, this adverse effect on freeze-thaw durability will be systematically discussed in the Section 4.4.

Table 4-2. P-wave velocities measured in the four types of concrete composites prior to the freeze-thaw weathering.

Mix	P-wave velocity (km/s)				
	Specimen 1	Specimen 2	Specimen 3	Mean	SD
PC	3.602	3.465	3.591	3.553	0.062
HFRC	3.960	4.178	4.062	4.067	0.089
M5-HFRC	3.872	3.920	3.994	3.929	0.050
M7-HFRC	3.814	3.944	3.849	3.869	0.055
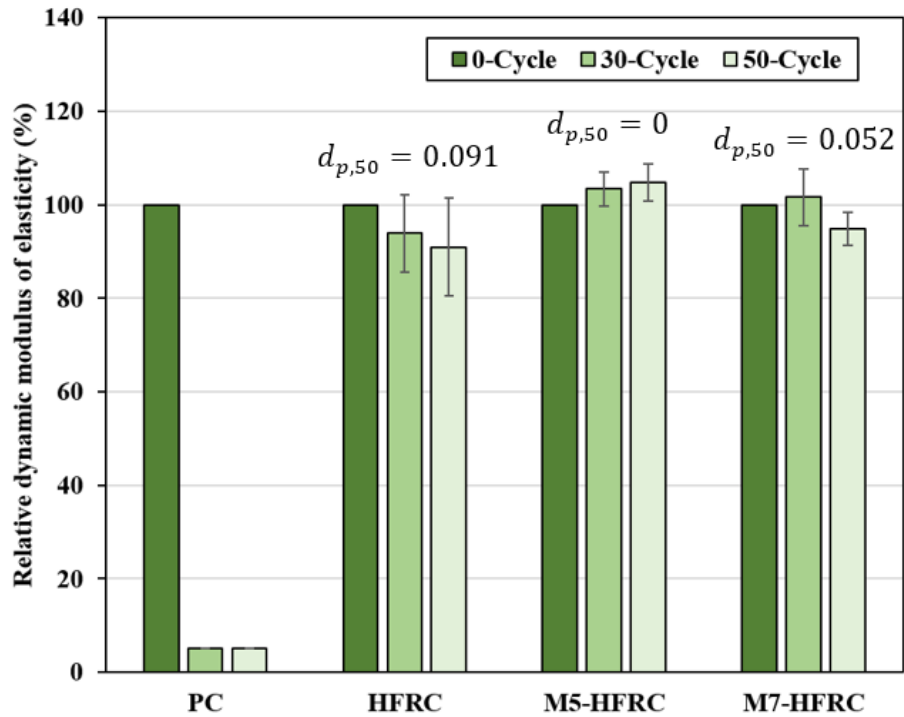
Figure 4-5. Influence of the freeze-thaw cycles on the relative dynamic modulus of the plain concrete and the fiber-reinforced concrete with distinct PCM contents, varying from 0, 5, to 7% by total volume.

4.4 Uniaxial Compression Test Results

4.4.1 Compressive Strength

To evaluate the influence of PCM content on the compressive strength of fibrous concrete, uniaxial compression tests are performed on cylindrical specimens. The values of compressive strength are independently derived from the average of four specimens. Again, the concrete design adopted for the present work is aimed to provide a freeze-thaw durable concrete material with a satisfactory compressive strength.

Figure 4-6 displays the compressive strength measured at the age of 7 days and 28 days for the plain concrete and the fiber-reinforced concrete with distinct PCM contents. It is clearly shown that the compressive strengths are considerably affected by the additions of hybrid fiber and PCM. The positive effect of adding hybrid fiber is evident from the elevated strength at both 7 and 28 days between PC and HFRC. In particular, compressive strength at 28 days is increased by 33% (12.18 MPa) with the hybrid fiber addition. The steel fiber, providing a lateral confinement against the axial compressive loading, is mainly attributable to the reinforced strength. The degree of enhancement at 28 days is consistent with the results of Nataraja et al. [9], who use steel fibers to improve the mechanical performance of concrete. In fact, a higher degree is obtained in this study, which may be contributed to the higher aspect ratio of the added steel fibers.

As revealed in Figure 4-7, the compressive strength of the hybrid fiber-reinforced concrete decreases by 3.6% at 7 days and 4.8% at 28 days, respectively, for each additional weight percentage of PCM. This trend is in good agreement with the findings reported by Hunger et al.[52], and Gürbüz and Erdem [55]. The reason for the strength reduction is that the PCM microcapsules have a considerably lower strength than other constituents in the concrete.

Moreover, increasing the PCM content may cause difficulties in dispersing the PCM particles in concrete mixture during the mixing, and subsequentially reduce the workability of the fresh concrete. The PCM clustering would induce more initial microvoids and microcracks, which reduces the distance between two nearest cracks in the concrete matrix, resulting in a lower compressive strength of the concrete. To investigate this effect, debris of the concrete specimens from compression test is examined by the scanning electron microscopy. In Figure 4-8, the PCM particles are well dispersed in the concrete sample of a 5% PCM content. On the contrary, the clustering of PCM particles can be seen in multiple locations in the concrete sample of a 7% PCM content. Moreover, it is observed that most PCM particles have been removed from the concrete matrix, indicating a weak bond strength between the PCM particle and the concrete matrix.

From the results in Figure 4-6 and Figure 4-7, it can furthermore expect that lowering the PCM content to 3.8% by volume would provide a compressive strength grade of 40 MPa at the age of 28 days for the fiber-reinforced concrete containing PCM microcapsules.

The fracture pattern of a plain concrete is shown in Figure 4-9. For comparison purpose, the fracture pattern of the fiber-reinforced concrete specimens are shown in Figure 4-10 through Figure 4-12.
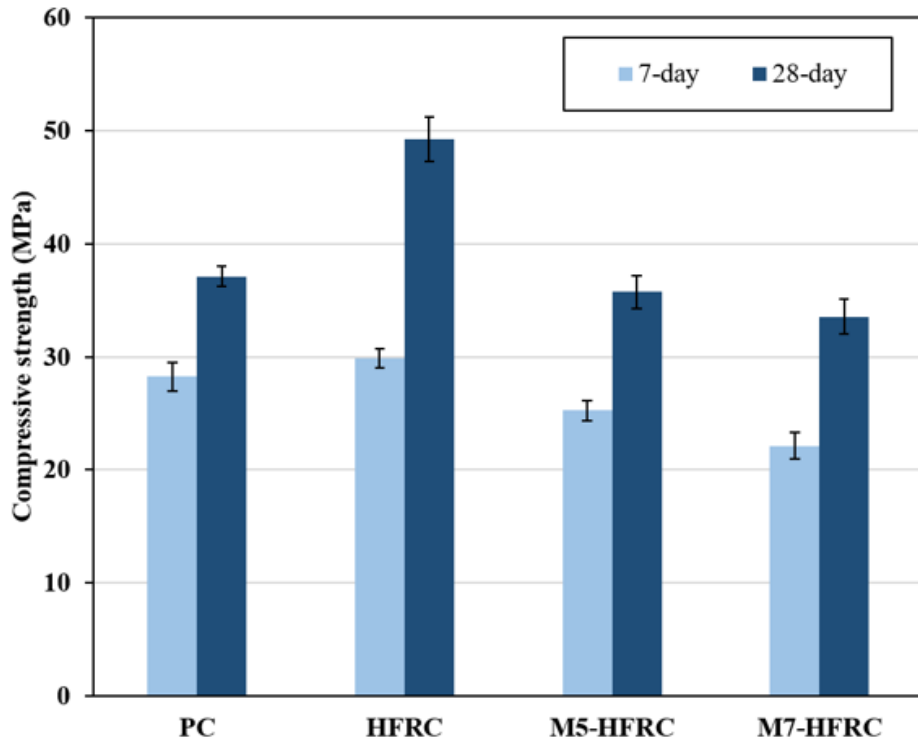
Figure 4-6. Compressive strengths at the age of 7 days and 28 days for the plain concrete and the hybrid fiber-reinforced concrete with distinct PCM contents, varying from 0, 5, to 7% by total volume.
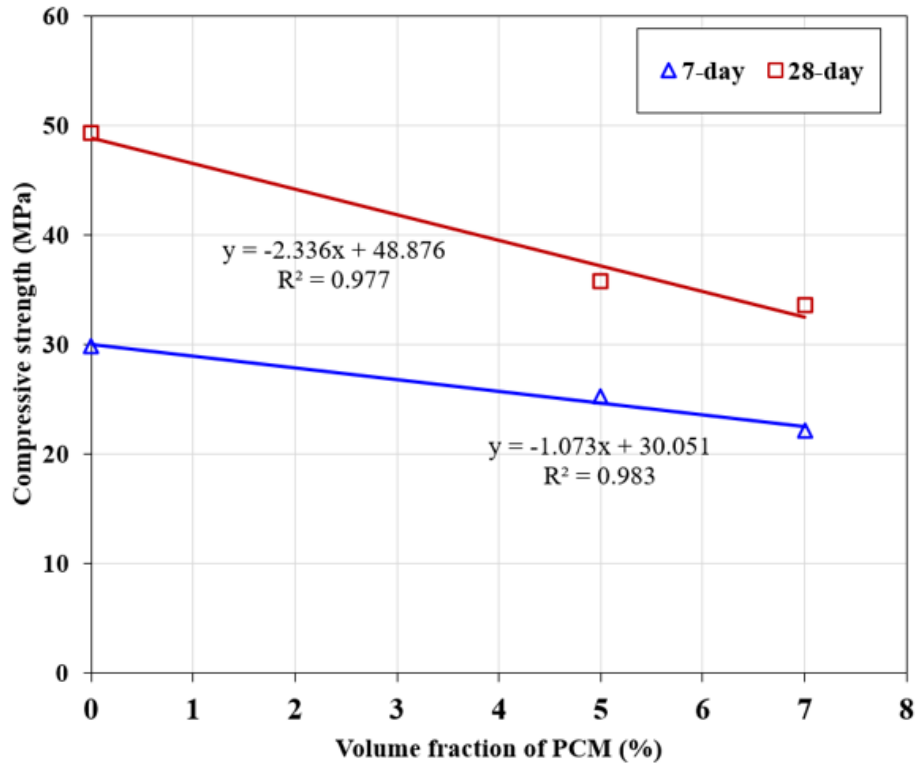
Figure 4-7. Influences of the PCM content on the compressive strength of concrete at the age of

7 days and 28 days.
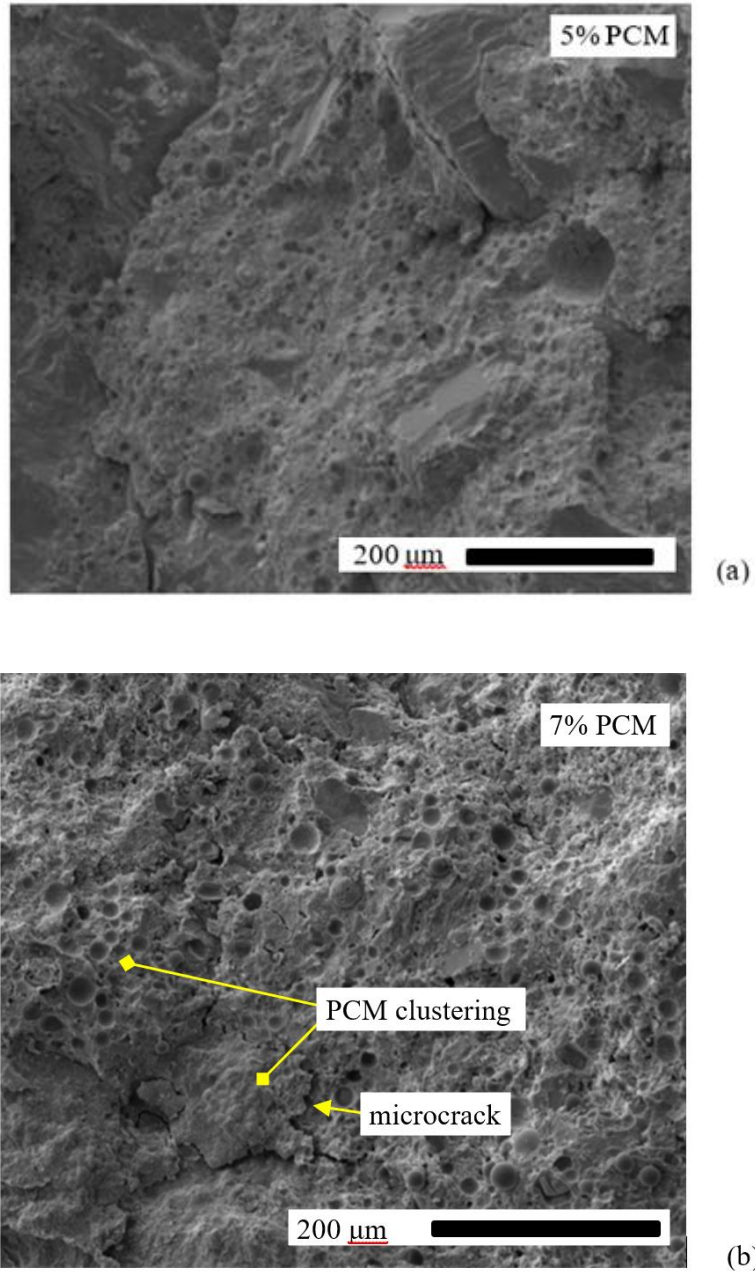
Figure 4-8. The distributions of PCM microcapsules in concrete matrix under a scanning electron microscopy. (a) The concrete contains 5% by volume of the PCM (M5-HFRC). (b) the concrete contains 7% by volume of the PCM (M7-HFRC). The arrow highlights the microcrack resulting from the clustering of the PCM microcapsules.

Figure 4-9. The fracture pattern for a plain concrete after compression test.

Figure 4-10. The fracture pattern for a fiber-reinforced concrete after compression test.

Figure 4-11. The fracture surface for a fiber-reinforced concrete after compression test.

Figure 4-12. The fracture pattern for a fiber-reinforced concrete with 7% PCM after compression

test.

4.4.2 Freeze-Thaw Damage Assessment on the Compressive Behaviors of Concrete

To characterize accumulated freeze-thaw damage on concrete, compressive strength and static modulus of elasticity were determined for the specimens subjected to 50 freeze-thaw cycles and the control specimens without weathering. Note that the influences arising from the continuing hydration during freeze-thaw cycles are considered by the submersion in water for the control specimens using Eq. (3-6). Thus, the freeze-thaw damage associated with the strength, as defined in Eq. (3-7), can be directly determined by the difference in the averaged compressive strength between the control and the freeze-thaw specimens for each concrete mixture. The freeze-thaw damage associated with the modulus is obtained in the same manner. For each concrete mixture in a specific weathering condition, at least two stress-strain curves are derived. exhibits the initial and damaged compressive stress-strain relations for each concrete mixture. For the sake of conciseness, only one curve for each mixture is reported.

As shown in Figure 4-14, the averaged compressive strength for each concrete mixture is decreased after subjected to 50 freeze-thaw cycles. It can be observed that d_f is reduced by the additions of PCM microcapsules, with the 5% PCM being the lowest. In Figure 4-15, d_E also indicates the trend compared with Figure 4-14. Moreover, d_E is larger than d_f for HFRC, which is consistent to the results reported by Hanjari et al. [23]. An opposite behavior is observed for M5-HFRC and M7-HFRC. The reduction in stiffness of concrete is mainly attributed to the debonding of fibers and aggregates, which prevents the stress transfer under loading. Since the presence of the PCM considerably reduce the microcracking on exposure to freeze-thaw cycles, there is no appreciable debonding of fibers and aggregates in the concrete with PCM. Thus, the stiffness of the concrete is not significantly affected.

Overall, the damage can be fully attributed to the solidification of water in pore system of concrete. Crystallization and hydraulic pressure build up during the freezing and thawing cycles, causing microcracking in the concrete matrix. The freeze-thaw cycling progressively deteriorates mechanical performance of concrete, as shown in the UPV results in Section 4.3.2. In fact, this type of damage has a strong connection with the temperature experienced by the concrete. The added PCM microcapsules reduce the freeze-thaw cycles by releasing heat energy in the form of latent heat at the temperature around 6°C upon cooling events. If the heat release from the PCM is insufficient to prevent freezing of water, the porosity associated to the PCM microcapsules acts as initial microcracks and thus increases the damage when crystallization and hydraulic pressure build up. Therefore, a higher PCM content would increase the initial microcrack density that accelerates crack propagation during freeze-thaw cycles. This is the reason for the increased values of damage variables for 7% PCM addition compared with 5% PCM addition in Figure 4-5, Figure 4-14, and Figure 4-15.
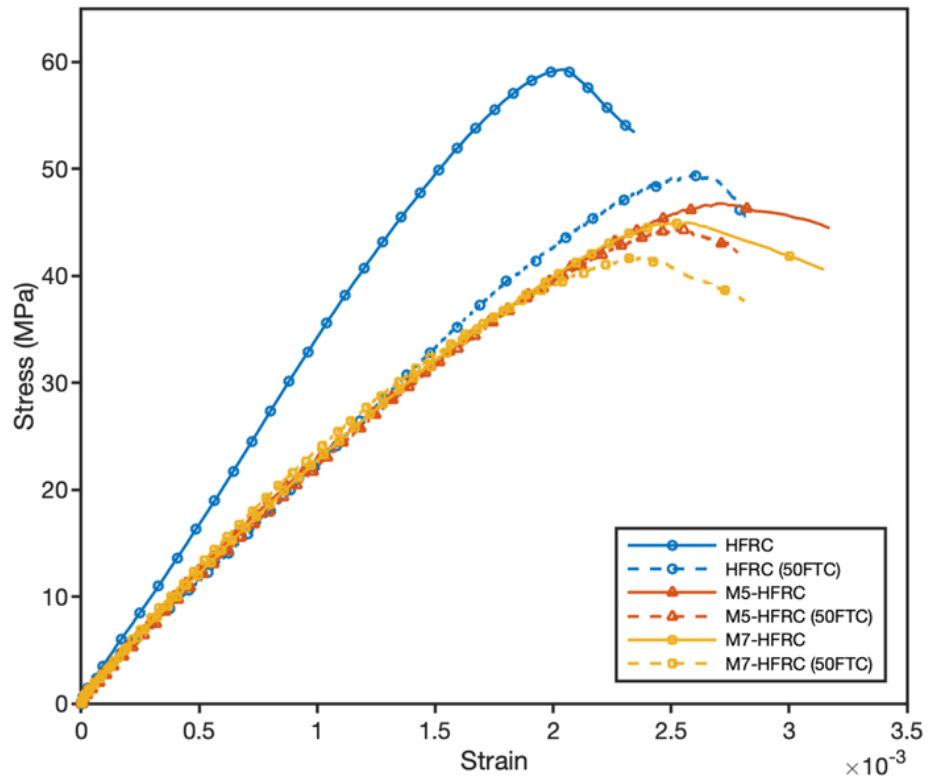
Figure 4-13. Compressive stress-strain relations for concrete specimens subjected to 50 freeze-

thaw cycles and without freeze-thaw weathering.
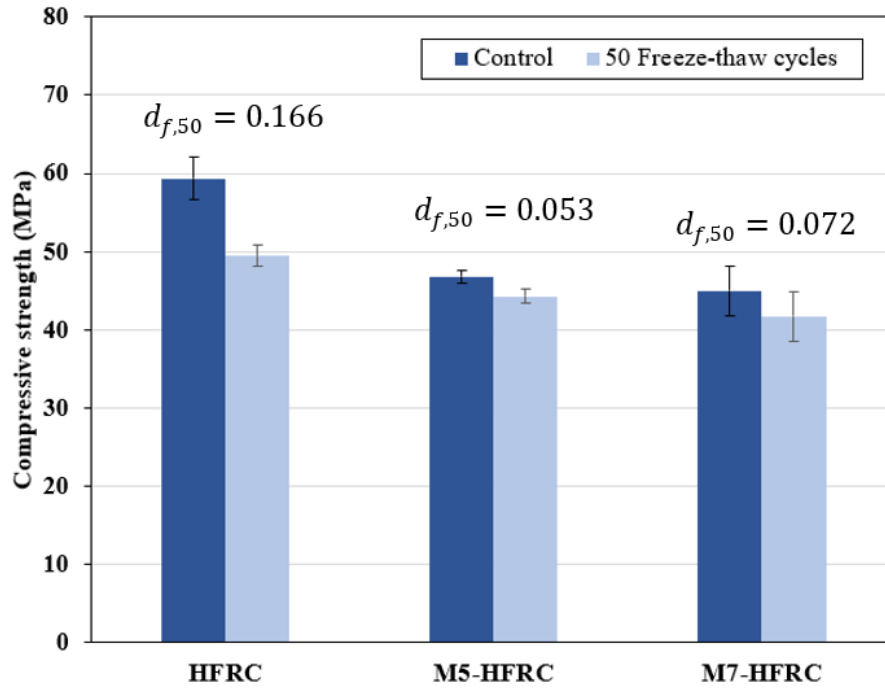
Figure 4-14. The influences of the 50 freeze-thaw cycles on the compressive strengths of the hybrid fiber-reinforced concrete with distinct PCM contents, varying from 0, 5, to 7% by total volume.
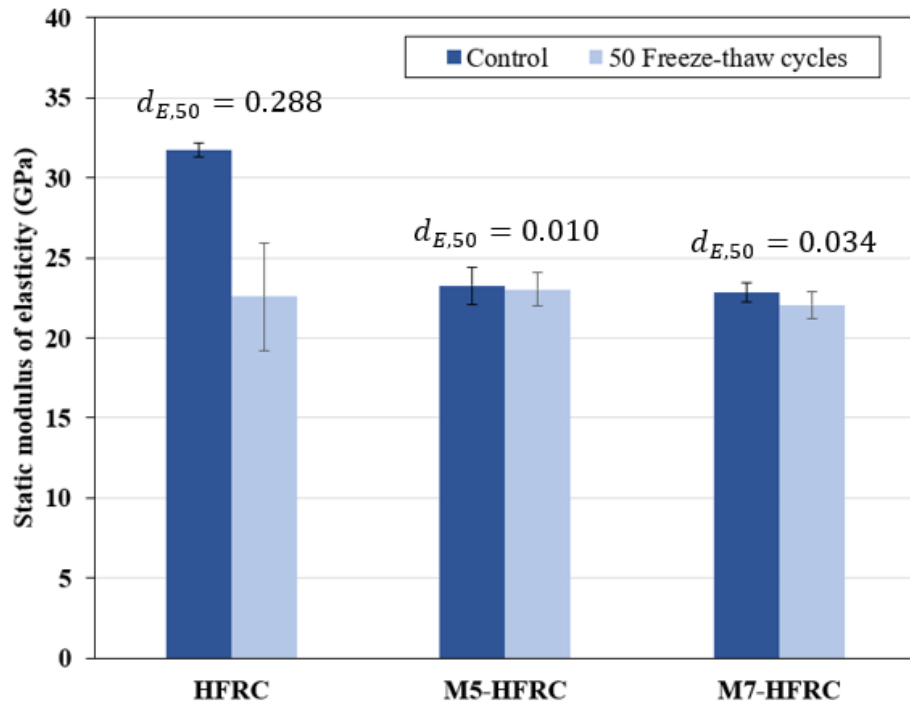
Figure 4-15. The influence of the 50 freeze-thaw cycles on the static moduli of elasticity for the hybrid fiber-reinforced concrete with distinct PCM contents, varying from 0, 5, to 7% by total volume.

4.5 Damage Model for Hybrid Fiber-reinforced Concrete Containing PCM

From the previous sections, it is observed that the freeze-thaw damage variables do not decrease monotonically with the increase of PCM content due to the beneficial and detrimental effects. To qualitatively describe the influences of thermal buffering and initial damage, it is assumed that these two effects are additive, characterized by coefficients A and B, respectively. Furthermore, since the damage reduction due to thermal buffering is related to the heat energy release, the total amount of energy could be released is proportional to the amount of PCM. Thus, the damage variable is written in the following form:

$$d = -A(V_{f_{PCM}}) + B(\bar{n})$$

(4-1)

where $V_{f_{PCM}}$ denotes the volume fraction of the added PCM. $\bar{n}$ is related to the initial microcrack density for a specific concrete design. A and B must be positive and can be obtained from experiments detailed below. To determine $\bar{n}$, each constituent is considered. For plain concrete, the initial microcrack density can be estimated by [45]:

$$n_{\widehat{0}} = \frac{12 f_{ag}(1-\eta)}{D_{max}^3(1-\eta^4)}$$

(4-2)

where $\eta = D_{min}/D_{max}$. D_{min} and D_{max} are the minimum and maximum aggregate size, respectively. f_{ag} represents the volume fraction of coarse aggregates. For fiber-reinforced concrete, the initial microcrack density, n_0, is related to that of the plain concrete, $n_{\widehat{0}}$, in the following form [10]:

$$n_0 = n_{\widehat{0}} e^{k_1 V_{f1}\frac{L_{f1}}{D_{f1}} + k_2 V_{f2}\frac{L_{f2}}{D_{f2}}}$$

(4-3)

where k_1 and k_2 are related to the bond strength of steel fibers and PVA fibers, respectively. V_{f1} and V_{f2} are the volume fractions of the fibers. L_{f1}/D_{f1} and L_{f2}/D_{f2} denote the aspect ratios of the fibers. However, such microcrack density relation does not consider the PCM content. Therefore, the microcrack density for concrete with microencapsulated PCM and the hybrid fiber can be extended to the following form:

$$n = n_0 e^{k_3 V_{f\,PCM}} \tag{4-4}$$

where k_3 is a parameter related to the mixing quality and PCM particle size distribution. k_3 can be obtained from SEM images or CT. It is worth to note that the actual values of k_1 and k_2 are not needed when a comparison is made relative to the fiber-reinforced concrete if a parameter $\bar{n} = n/n_0$ is defined. A parameter sensitivity of k_3 is shown in Figure 4-16. In this case, k_3 is approximated to be 20, which implies the microcrack density parameter for a 5% PCM volume fraction is approximately equal to 2.7. For other concrete design, k_3 is to be determined by SEM images or CT. Since n is the cumulative effect of fiber and PCM addition, the equation is normalized with n_0 such that linear regression can be performed to determine A and B. For the three damage variables defined in Chapter 4, Eq. (4-1) is adopted to establish the relations between the damage variables and the PCM content. The linear regression results of A and B for each damage variable is shown in Figure 4-17 through Figure 4-19.
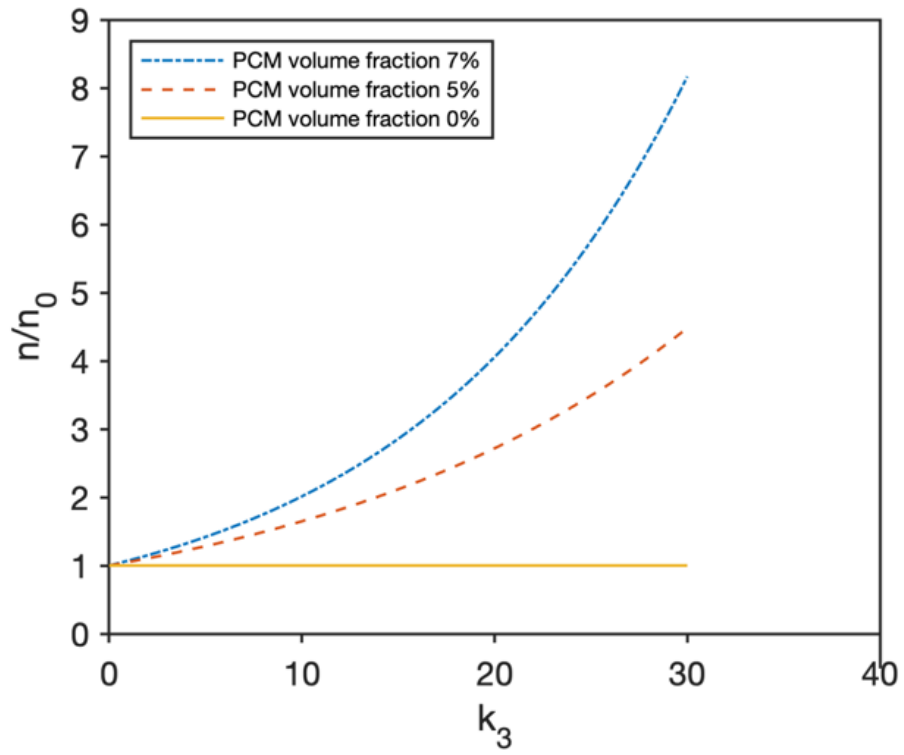
Figure 4-16. Parameter sensitivity of parameter k_3.
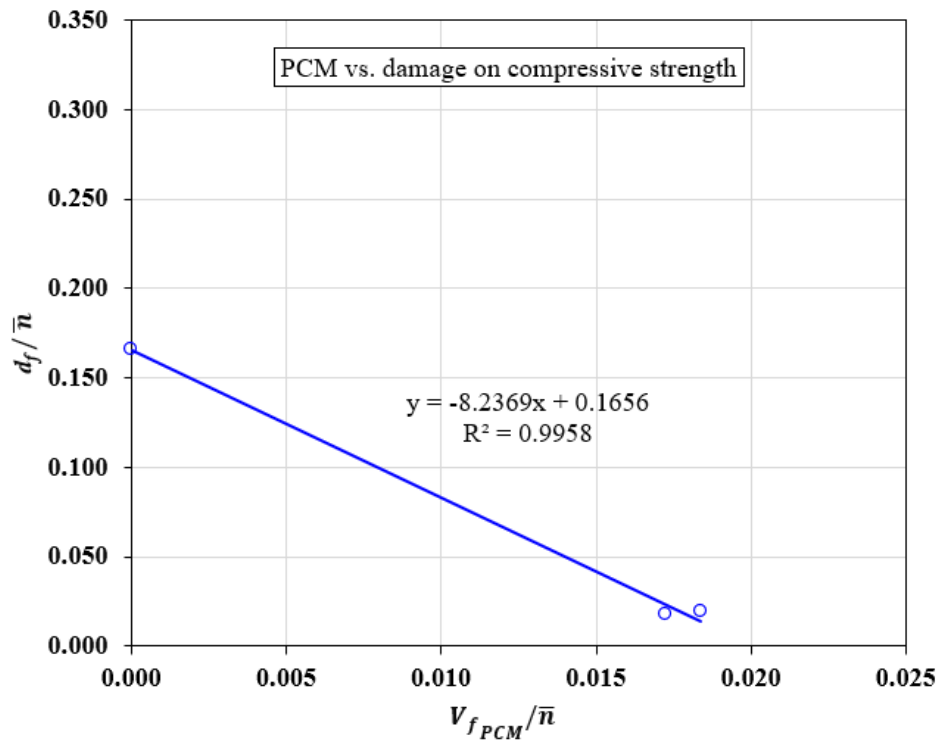
Figure 4-17. Linear regression results of coefficient A and B for d_f.
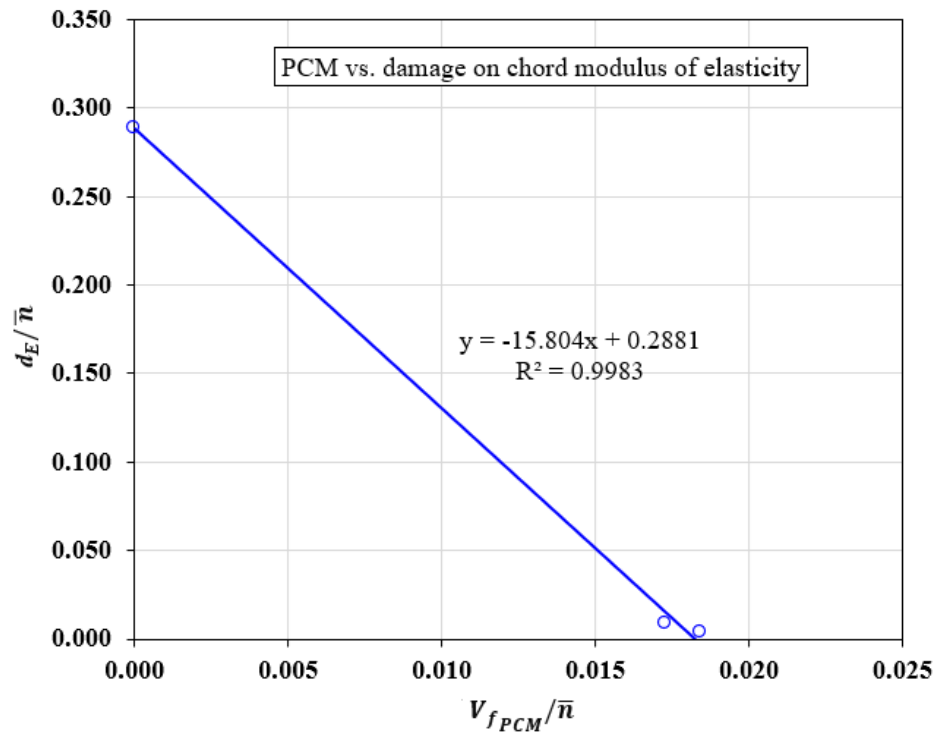
Figure 4-18. Linear regression results of coefficient A and B for d_E.
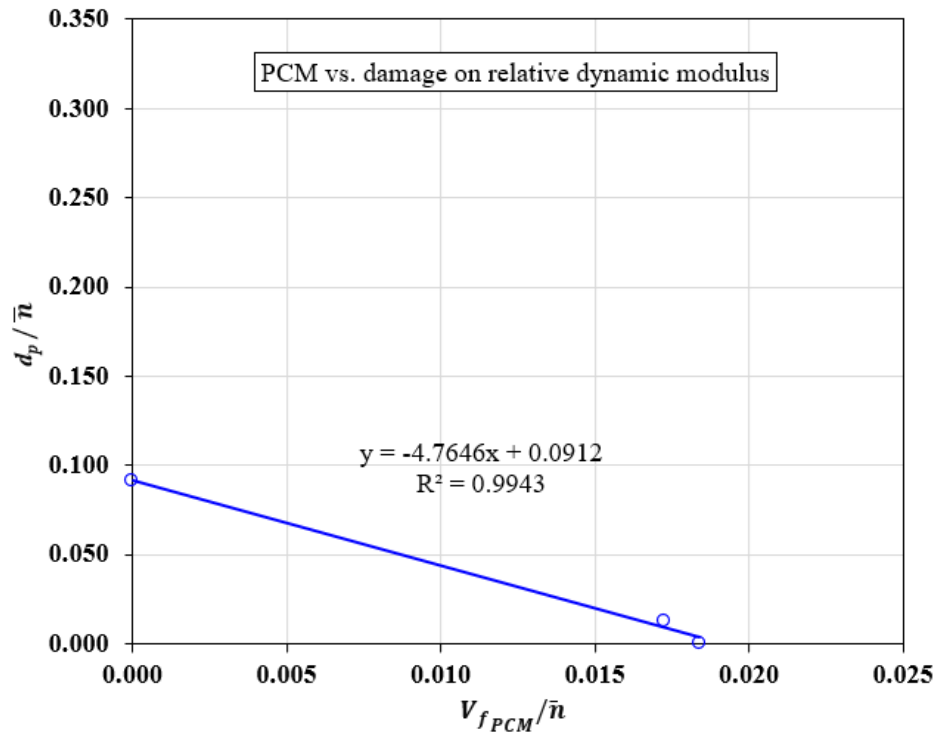
Figure 4-19. Linear regression results of coefficient A and B for d_p.

4.6 Quantitative assessment of beneficial and detrimental effects of adding PCM

Figure 4-20 through Figure 4-22 present the comparisons of predicted damage variables and the experimental results obtained from compression tests and ultrasonic tests. It clearly shows that the models recover the damage variables without the addition of PCM, because the value is controlled by the coefficient B when $V_{f_{PCM}} = 0$. Since freeze-thaw cycles do not heal the concrete, $d \geq 0$ must be satisfied. Moreover, compressive strength, elastic modulus, and RDM are all positive, and therefore $d < 1$ is required. These requirements on damage variables lead to the following confinements on coefficients A and B of the damage model:

$$d \geq 0; \quad \ln\left(\frac{A}{Bk_3}\right) \leq 1 \tag{4-5}$$

$$\frac{d}{dx}(d) = 0 ; \quad \left(V_{f_{PCM}}\right)_{opt} = \frac{1}{k_3}\ln\left(\frac{A}{Bk_3}\right) \tag{4-6}$$

$$d < 1; \quad -Ax + Be^{k_3 V_{f_{PCM}}} < 1; \; solve \; \left(V_{f_{PCM}}\right)_{max} \; by \; numerical \; method \tag{4-7}$$

$$\left(V_{f_{PCM}}\right)_{opt} = \frac{1}{k_3}\ln\left(\frac{A}{Bk_3}\right) \; and \; V_{f_{PCM}} \geq 0; \; \ln\left(\frac{A}{Bk_3}\right) \geq 0 \tag{4-8}$$

The proposed damage model is summarized as following:

$$d = -A \times V_{f_{PCM}} + B \times e^{\left(k_3 \times V_{f_{PCM}}\right)} \tag{4-9}$$

with the confinements on the coefficients A and B:

$$0 \leq \ln\left(\frac{A}{Bk_3}\right) \leq 1 \tag{4-10}$$

and the optimum dosage of PCM can be expressed as:

$$\left(V_{f_{PCM}}\right)_{opt} = \frac{1}{k_3}\ln\left(\frac{A}{Bk_3}\right) \tag{4-11}$$
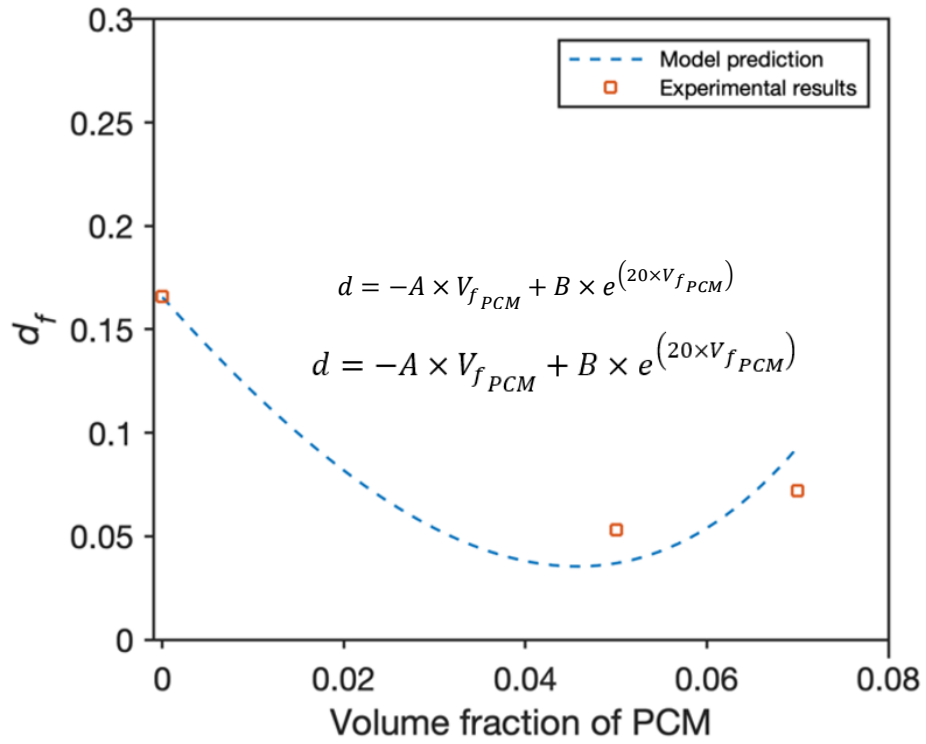
Figure 4-20. The influence of PCM content on the freeze-thaw damage variable d_f. A = 8.264, B

= 0.166.
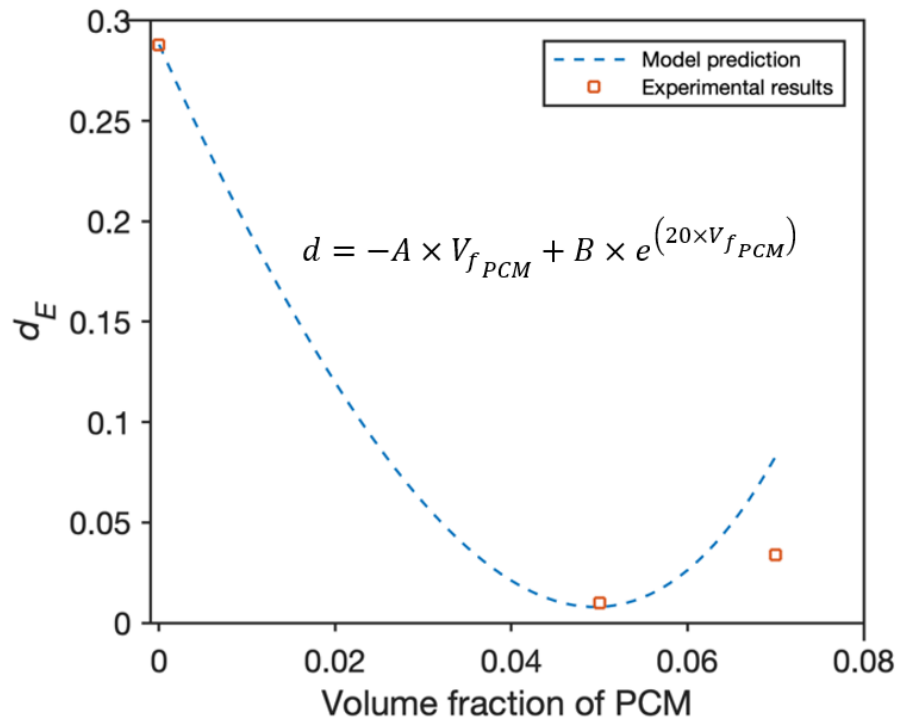
Figure 4-21. The influence of PCM content on the freeze-thaw damage variable d_E. A = 15.504, B = 0.288.
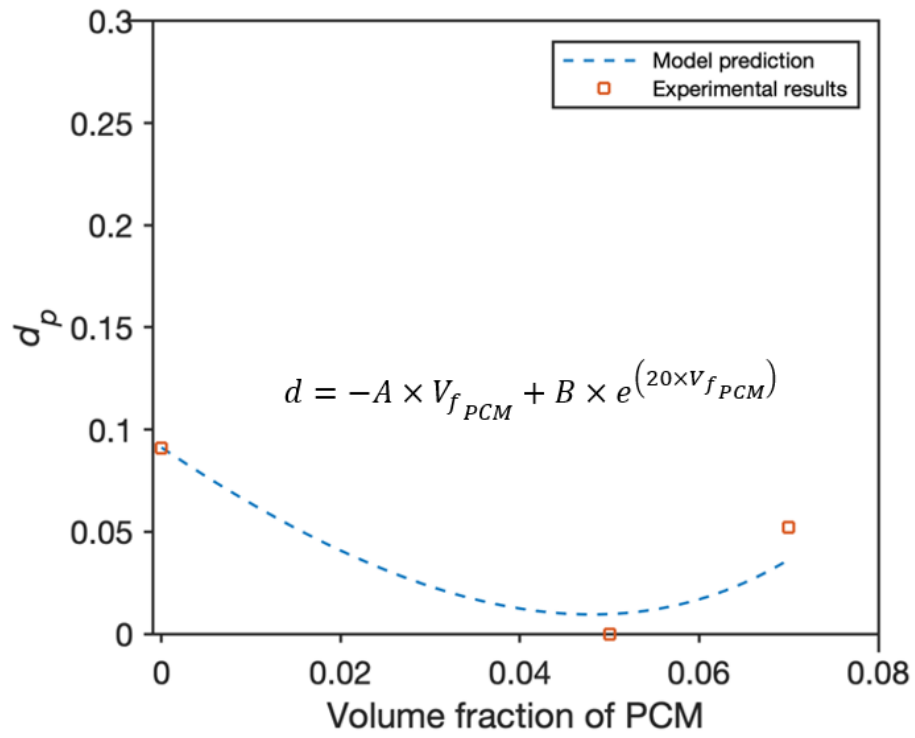
Figure 4-22. The influence of PCM content on the freeze-thaw damage variable d_p. A=4.765, B=0.091.

4.7 Concluding Remarks

In this chapter, the influences of PCM dosage on the freeze-thaw durability and compressive behaviors of fiber-reinforced concrete are investigated. The concrete specimens made with the newly proposed mix proportions are subjected to 50 freeze-thaw cycles, with the temperature range of -30℃ to 20℃ in each cycle. Uniaxial compression tests and UPV tests are performed on the cylindrical concrete specimens to assess the damage extents due to the thermal cycling. The most important findings are summarized as follows:

1) The steel and PVA fibers retain their individual capacities in the hybrid form. The compressive strength at the age of 28 days is increased by 33% with the hybrid fiber addition, compared with the plain concrete. The surface freeze-thaw durability is also considerably improved by the hybrid fiber addition within the 50 freeze-thaw cycles.

2) Damage variables associated with RDM, compressive strength, and elastic modulus are determined for the hybrid fiber-reinforced concrete subjected to 50 freeze-thaw cycles. While the beneficial effect of adding PCM on retarding the damage growth is confirmed, an adverse effect of increasing PCM microcapsules dosage on the freeze-thaw durability of concrete is revealed.

3) The beneficial effect and the detrimental effect of PCM on reducing freeze-thaw damage on concrete are quantified and modeled. The damage model makes good agreements with the test results obtained in this research. An explicit expression for predicting the optimized PCM dosage is provided.

4) To minimize the negative effect of PCM on the freeze-thaw durability, the freezing temperature for weathering the concrete is reduced from -30℃ to -20℃, and the maximum

PCM dosage is increased from 7% to 9% such that the heat release from the PCM should be sufficient to prevent the freezing of water in the concrete. These are the adjustments for the research described in the next chapter.

Chapter 5 Investigations into the Freeze-thaw Damage and the Flexural Behavior of Hybrid Fiber-reinforced Concrete Containing Phase Change Material

5.1 Test procedures

The present research is developed to investigate the impacts of phase change material (PCM) incorporation on the freeze-thaw durability and the flexural behavior of concrete. The complete testing program and the outcomes to be reported are summarized in Figure 5-1. The concrete mix proportions are designed with a PCM volume fraction varying from 0% to 9%. The hybrid fiber, consisting of the steel fiber and the polyvinyl alcohol microfiber, is added in a constant dosage of 1.1%. The three-point bending test is performed on notched concrete beams to obtain the load-crack tip opening distance (P-CTOD) relationship, and the load-midspan displacement relationship for hybrid fiber-reinforced concrete containing distinct dosages of PCM prior to the process of freezing and thawing cycles. The three-point bending test setup with the notched prismatic concrete specimen can be seen in Figure 3-23.

Another group of prismatic specimens is subjected to continuous freeze-thaw cycles with the tailor-make freeze-thaw machine in a controlled environment. Since the dimensions and the shape of the specimens has changed from 4" by 8" cylinders to 4" x 4" x 14" beams, box containers are fabricated using acrylic plates in 1/2" thickness obtained from Santa Monica Plastics, a local plastics supplier. Figure 5-3 and Figure 5-4 display the box container in two directions. The conclusive results in Chapter 4 have shown that the intensity, the freezing and thawing periods, and the recursive number of the thermal cycling can damage the fiber-reinforced concrete

specimens with a 7% volume fraction of PCM. Therefore, the magnitude of the freezing temperature is reduced from -30°C to -20°C. The duration of the freezing phases is truncated from 14 hours to 8 hours. The number of freeze-thaw cycles in the thermal cycling test is decreased from 50 to 40 cycles. Figure 5-5 displays the temperature profile of a control prismatic specimen and the four freeze-thaw cycles, which is recorded using the temperature measuring module in Section 3.2.1. From this figure, the registered thermal cycles alternate between +22°C and -20°C, and the temperature at the center of the control prismatic specimen varies between +8°C and -5°C.

After the freeze-thaw weathering, the three-point bending test is performed and the flexure characteristics of the flexural load-displacement curves are compared with the values measured prior to the cycles for the freeze-thaw damage evaluation. Moreover, the changes in the relative dynamic modulus of elasticity, which is indicative of the internal damage extent of concrete, are obtained by ultrasonic pulse velocity (UPV) tests in the vicinity of the notch over the freeze-thaw cycles. Figure 5-7 displays the test setup of UPV test for the prismatic specimens. The changes in absorption capacity and the mass loss during the freeze-thaw cycles are recorded over the thermal cycling. The procedures to prepare the prismatic specimens for UPV tests and the weight measurements are illustrated in Figure 5-8.

It is worth mentioning that the concrete specimens were stored in the control environment for over 5 years before the freeze-thaw tests were performed. The appearance of the specimens prior to the tests is shown in Figure 5-9. It is possible that the micro-cracks or micro-voids have been generated in the specimens between the manufacturing of the specimens and the moment of the first thermal cycling test. Therefore, the test results are aimed for providing qualitative assessment on the freeze-thaw damage. The experimental results will show that the added PCM considerably affect the flexural behaviors of the hybrid fiber-reinforced concrete.

116
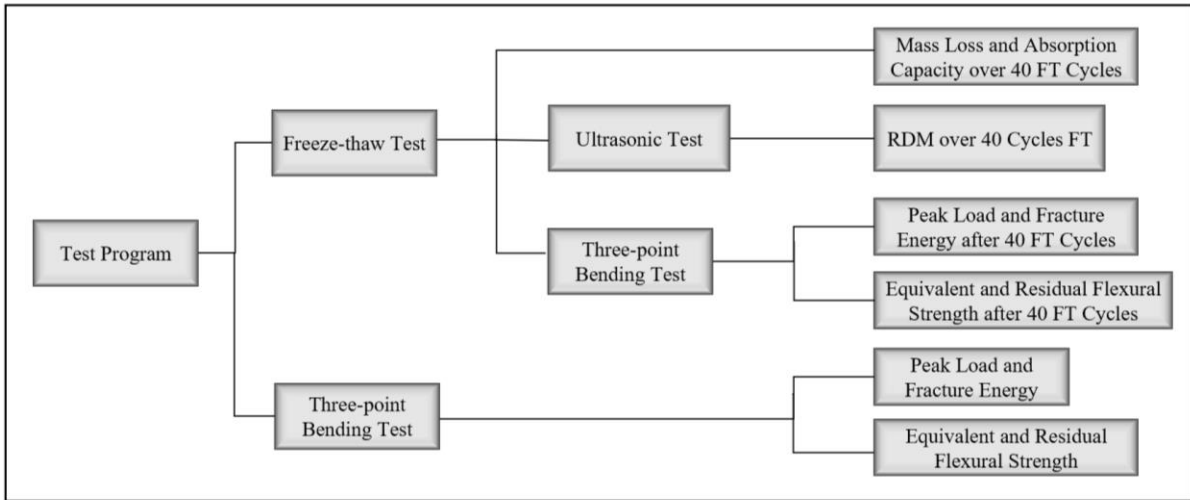
Figure 5-1. The flow chart of the complete testing program with prismatic specimens.
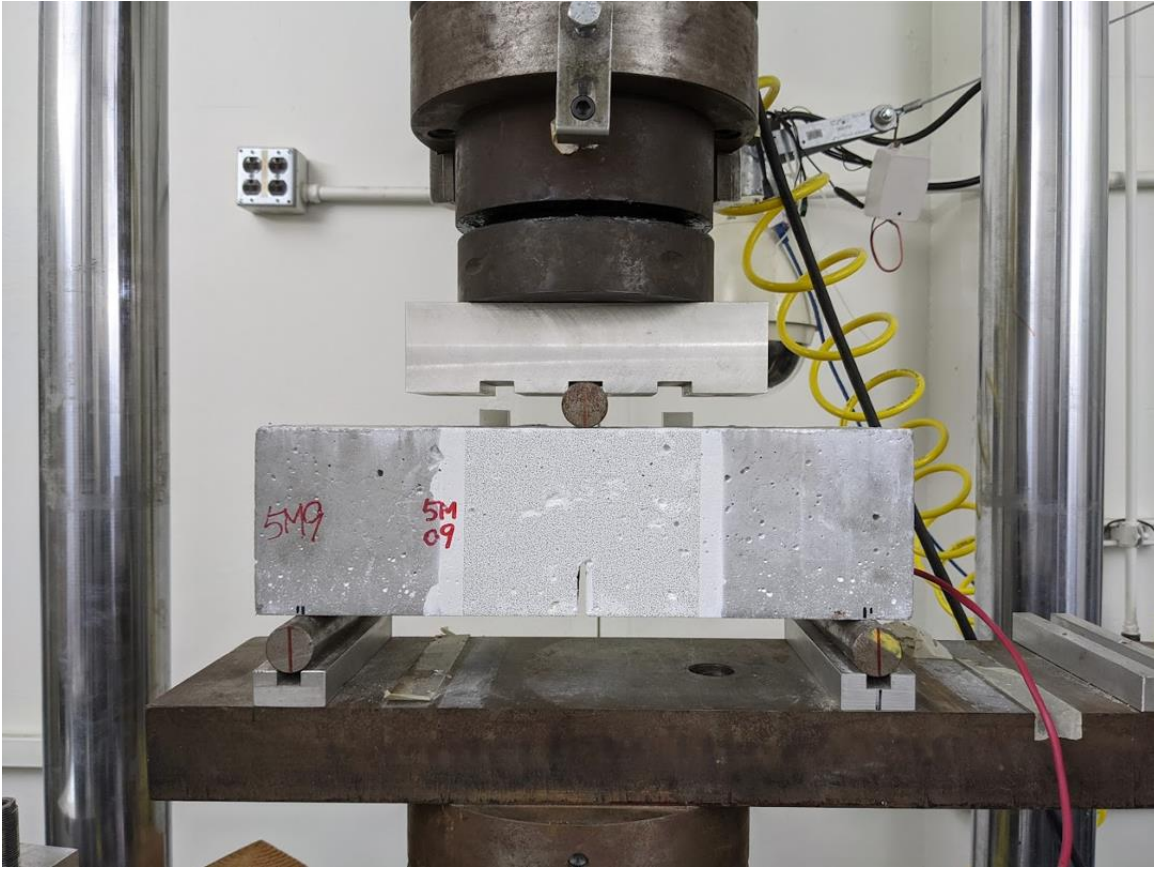
Figure 5-2. The three-point bending test setup with the servo-hydraulic machine and the

prismatic concrete specimen.
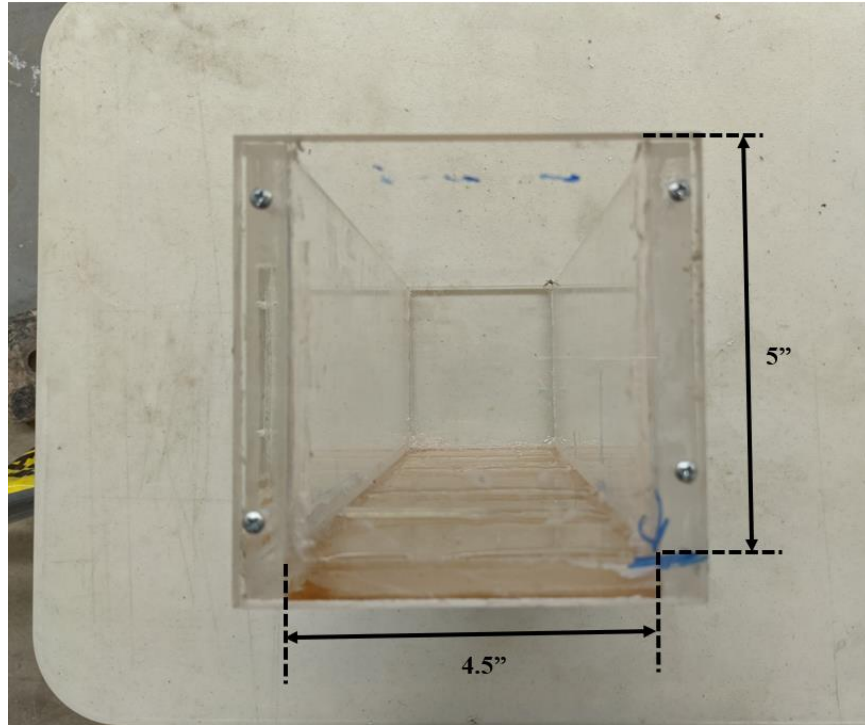
Figure 5-3. The box container adopted for the concrete beams in the freeze-thaw test.
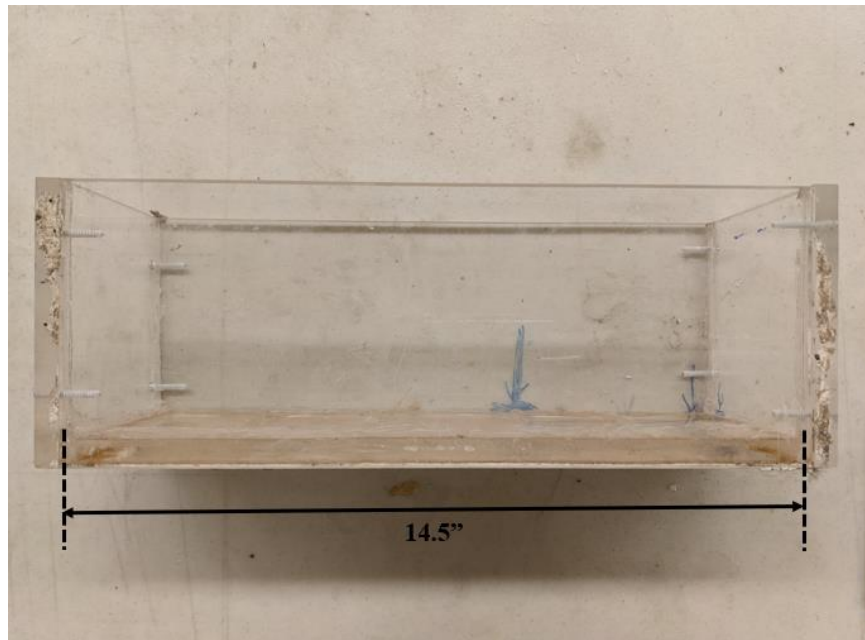
Figure 5-4. The side view of the box container adopted for the concrete beams in the freeze-thaw.
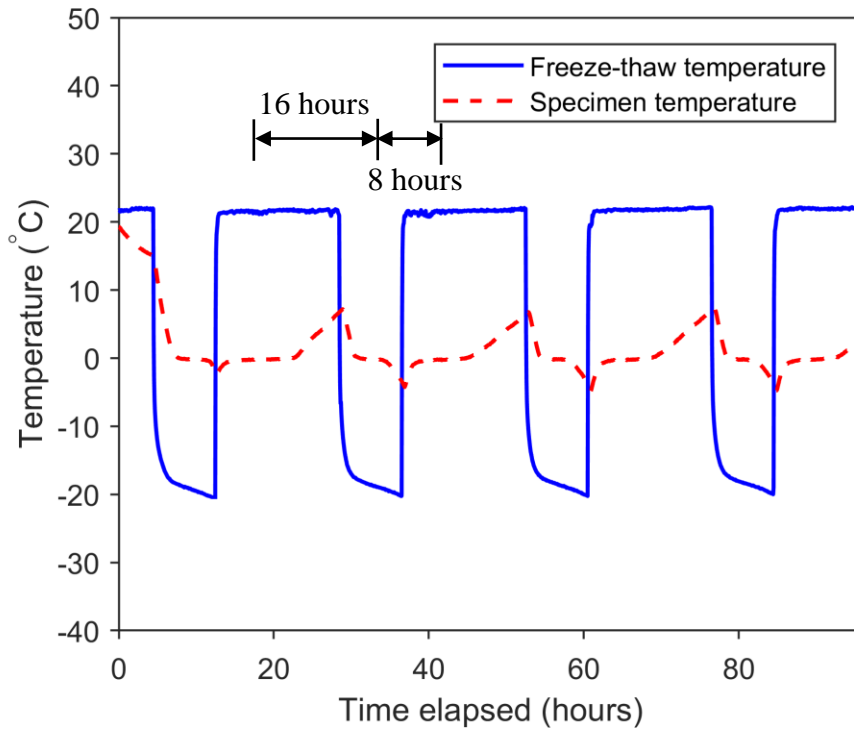
Figure 5-5. The temperature profile measured at the climate chamber and at the center of a

control prismatic specimen for four freeze-thaw cycles.
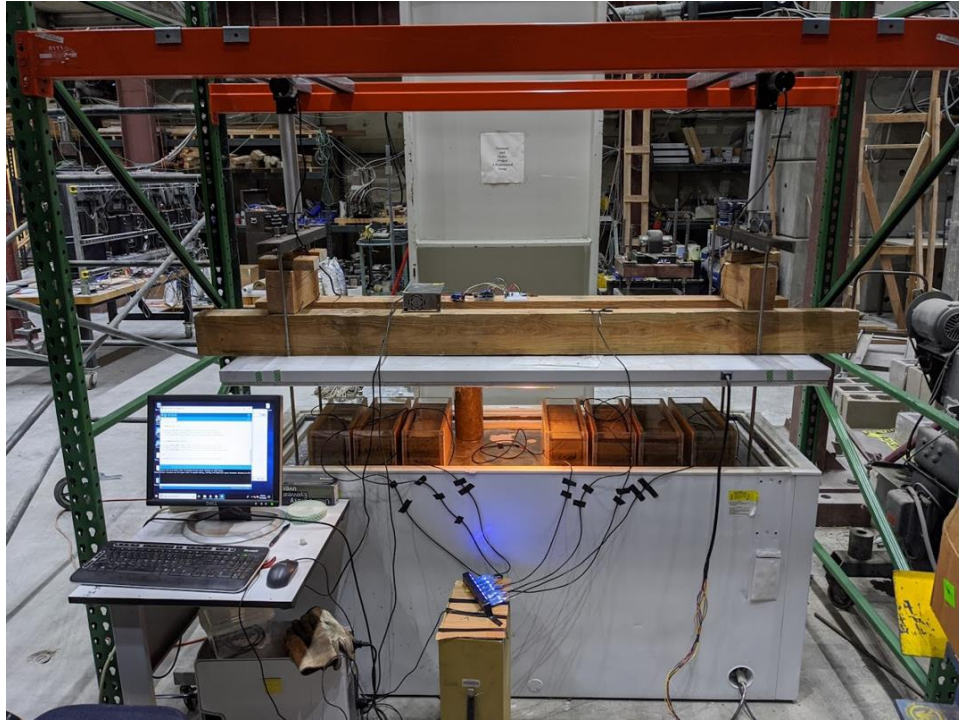
Figure 5-6. The computer-automated freeze-thaw machine with Arduino microcontroller for

weathering prismatic concrete specimens.
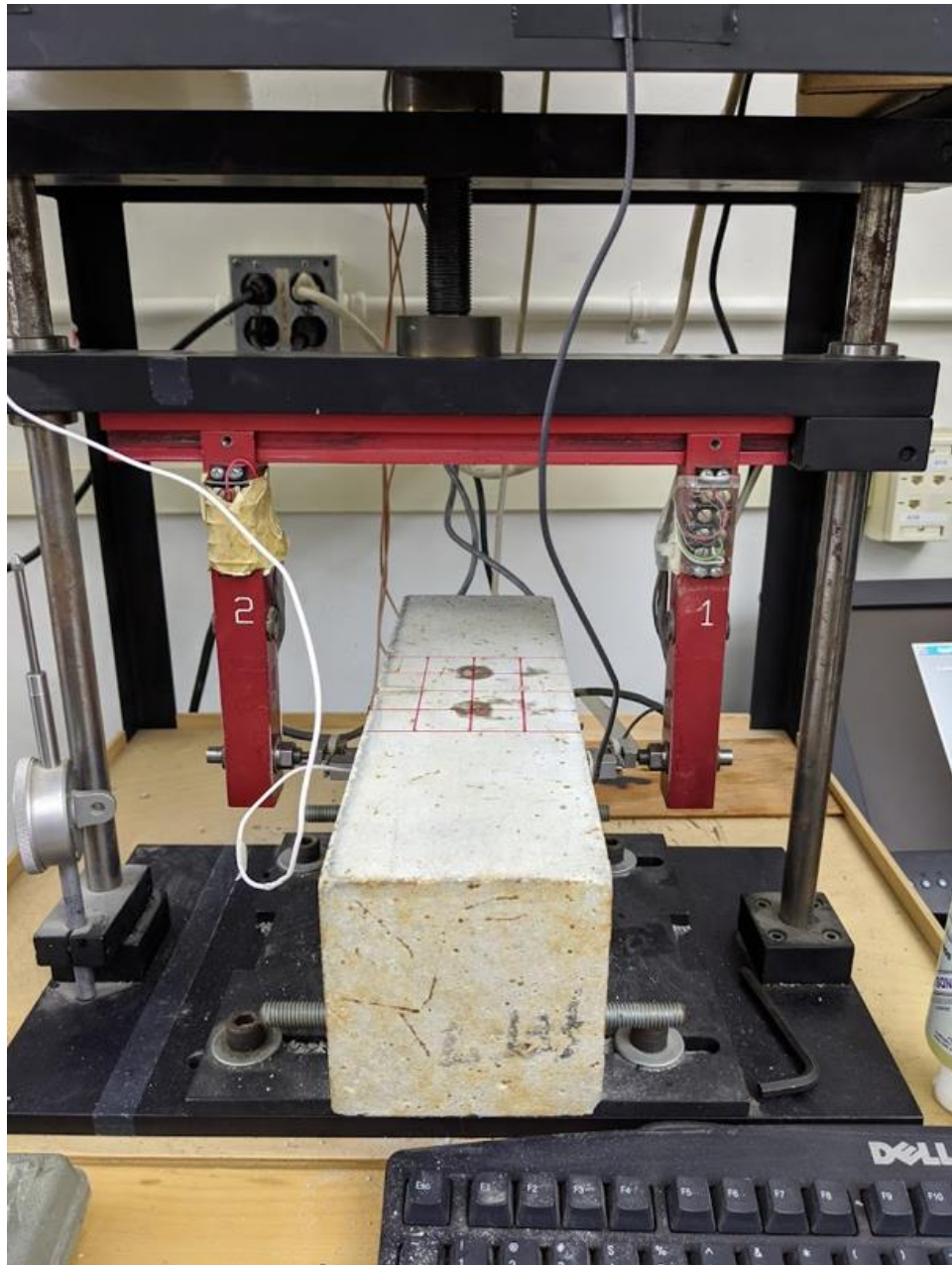
Figure 5-7. The ultrasonic pulse velocity test setup for the prismatic specimen.
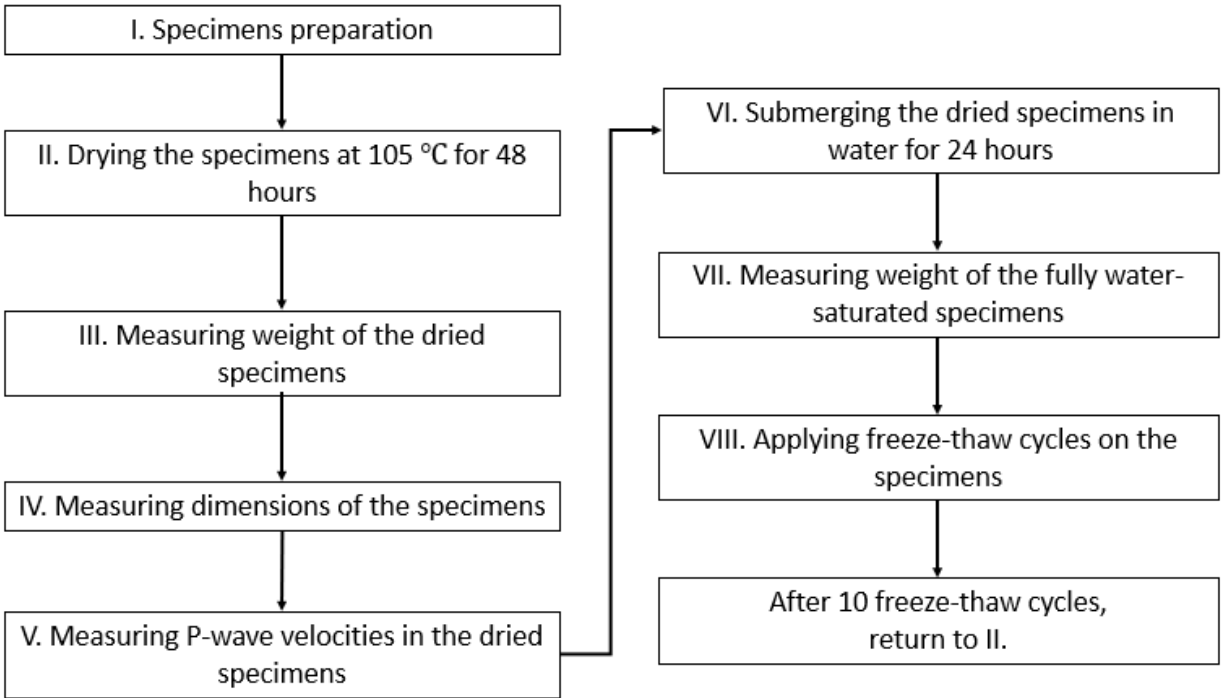
Figure 5-8. The flow chart of testing procedures for mass loss, water absorption capacity, and the

P-wave velocity in concrete.
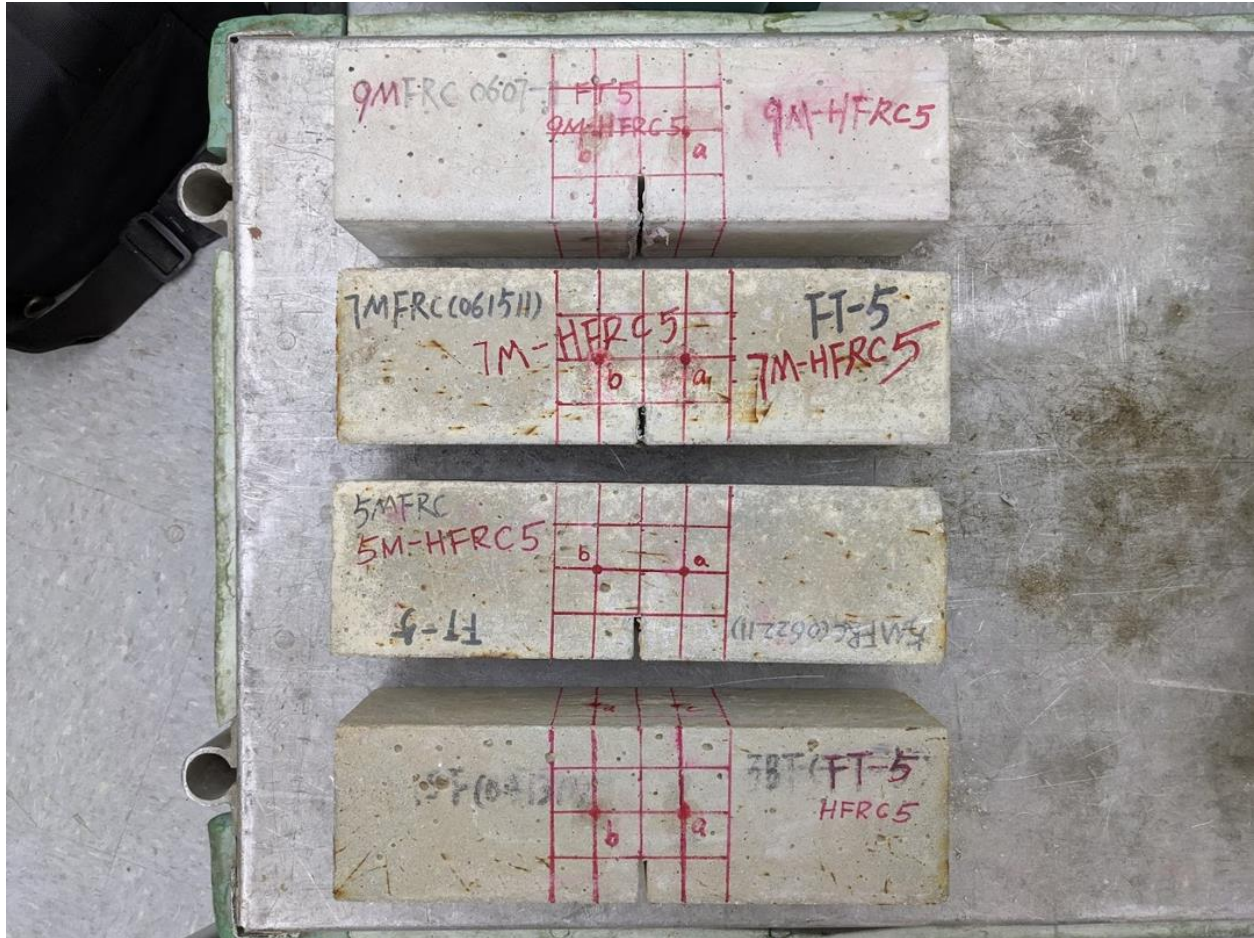
Figure 5-9. The premade concrete beams before freeze-thaw weathering. The 9M-HFRC (at top)

and the HFRC (at bottom) beams are used in the testing program.

5.2 Mass Loss and Absorption Capacity after Freeze-thaw Weathering

The results of mass loss and the increase of water absorption capacity are two indicators of the freeze-thaw damage of concrete. The loss of mass may be attributed to the scaling of the damaged concrete surfaces, or the micro-cracks and micro-voids that are generated inside the concrete during the freezing and thawing cycles. The absorption capacity is determined by the following relationship,

$$Absorption\ capacity\ = \left(\frac{m_{wet} - m_{dry}}{m_{dry}} \right) \tag{5-1}$$

where m_{wet} is the weight of concrete measured in the saturated-surface dry condition, and m_{dry} denotes the weight of concrete measured after drying in an oven at 105°C for 48 hours. To attain the saturated-surface dry condition for the concrete, the prismatic specimens are submerged in the water for at least 48 hours at the room temperature. Figure 5-10 shows the oven used to dry the concrete beams. The mass loss and the water absorption capacity are recorded after 10, 20, 30, and 40 cycles of the freeze-thaw weathering.

Figure 5-11 illustrates the mass loss of the plain concrete, and the hybrid fiber-reinforced concrete with phase change material (PCM) dosages varying from 0%, 5%, to 9% over the 40 freeze-thaw cycles. It should be noted that the plain concrete (PC) and the hybrid fiber-reinforced concrete without PCM (HFRC) are significantly damaged after 10 cycles by visual inspections. Therefore, the PC and HFRC specimens are removed from the test program after 10 cycles. The results of mass loss indicate that the hybrid fiber-reinforced concrete with a 9% PCM dosage (M9-HFRC) has the mass reduction less than 1% over the 40 cycles of freezing and thawing. This

suggests that the increase of PCM volume fraction in the concrete has a positive effect on the freeze-thaw damage mitigation.

Figure 5-12 displays the water absorption capacity of the plain concrete and the hybrid fiber-reinforced concrete with phase change material (PCM) dosages varying from 0%, 5%, to 9% over the 40 freeze-thaw cycles. The PCM addition would increase the micro-voids in the concrete, and therefore increase the water absorption capacity of the concrete. It can be observed that the water absorption capacity of the hybrid fiber-reinforced concrete without PCM (HFRC) is higher than that of the hybrid fiber-reinforced concrete with a 5% PCM addition at the onset of freeze-thaw test. This result can be attributed to the undesirable initial damage (or the micro-voids) in the HFRC generated between the manufacturing of the specimens and the moment of the first thermal cycling test. Moreover, the M9-HFRC has the smallest changes in the water absorption capacity, which indicates that the M9-HFRC has the least micro-voids generated over the 40 freeze-thaw cycles. This result is consistent with the mass loss monitored during the freezing and thawing cycles.

Figure 5-10. The oven used to prepare the concrete specimens for the absorption capacity

measurements.
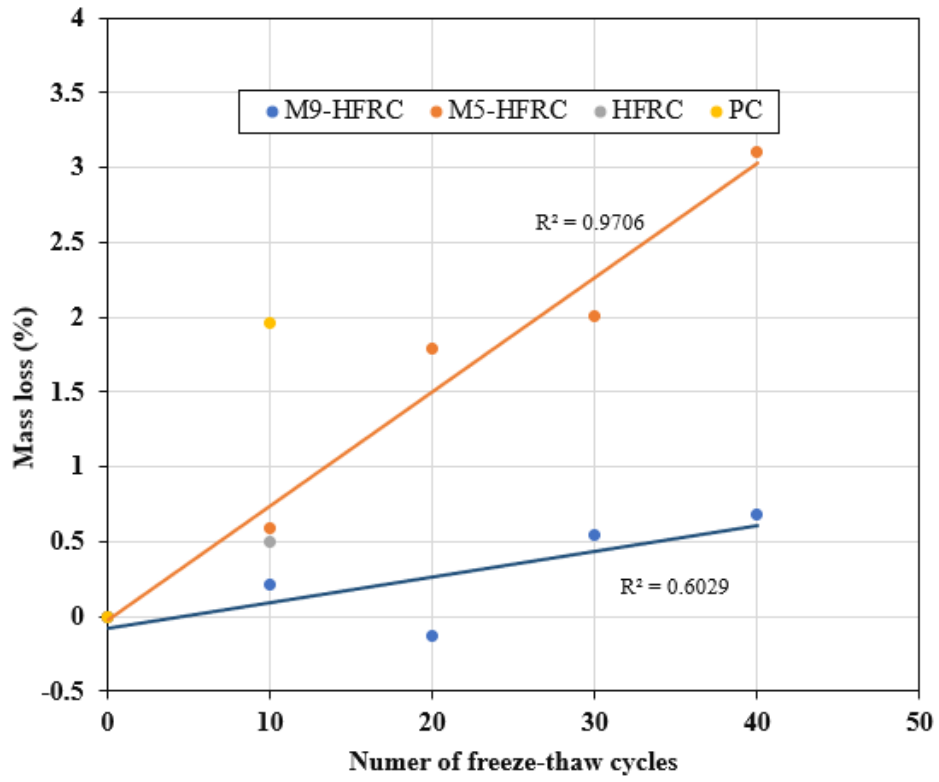
Figure 5-11. The influence of freeze-thaw cycles on the mass loss of concrete.
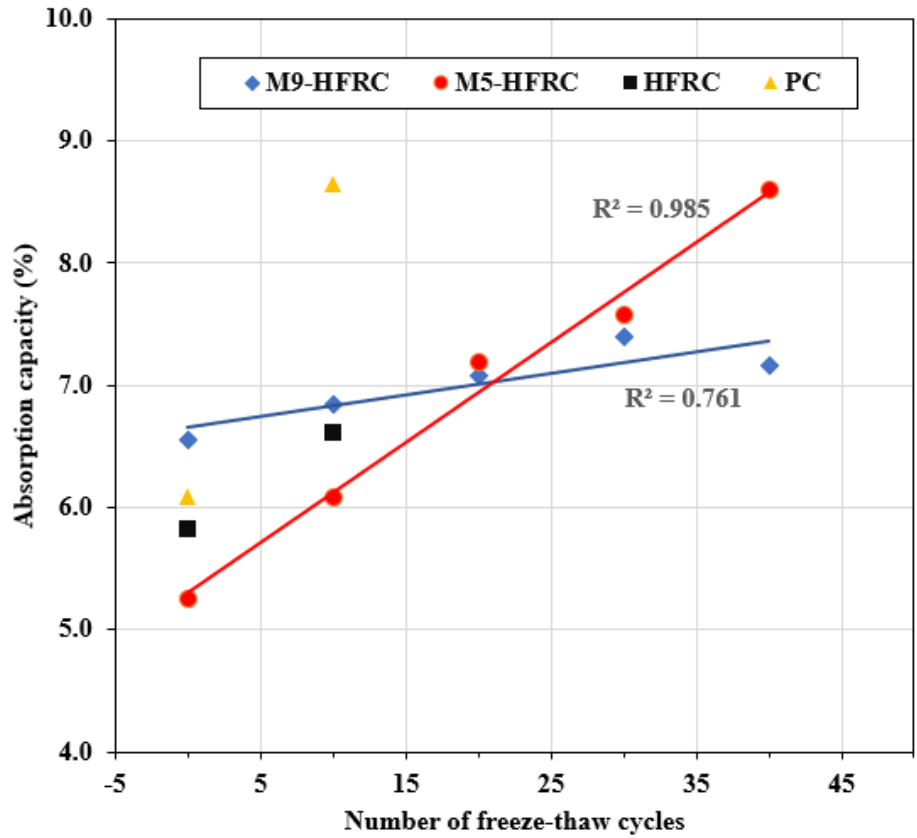
Figure 5-12. The influence of freeze-thaw cycles on the absorption capacity of concrete.

5.3 Ultrasonic Pulse Velocity Test Results

5.3.1 Relative Dynamic Modulus of Elasticity

A grid of designated measurement points was arranged on the concrete beam surfaces. Figure 5-13 illustrates the locations of the measurement points on the side of the beam. At each point, the ultrasonic P-wave transit time through the width of prismatic specimen was measured over the 40 cycles of freezing and thawing. The ultrasonic P-wave velocity, relative dynamic modulus of elasticity, and the damage associated with the relative dynamic modulus of elasticity were determined.

Figure 5-14 reveals the influence of successive freeze-thaw cycles on the relative dynamic modulus of elasticity (RDM) for the fiber-reinforced concrete prismatic specimens with distinct PCM contents, varying from 0, 5, to 9% by total volume. It is not feasible to obtain the result for the damaged fiber-reinforced concrete without PCM (HFRC) due to specimen disintegration after 10 freeze-thaw cycles. Under this damage extent, the receiving ultrasonic signal is highly attenuated. From the result of Figure 5-14, it shows that adding PCM has a significant beneficial effect on the RDM. The concrete with a 9% PCM addition (M9-HFRC) can withstand 40 cycles of freezing and thawing in terms of the negligible changes in the RDM. Since the concrete is undamaged over the freeze-thaw cycling, the adverse effect of adding PCM on the RDM is not observed. The addition of PCM may increase the micro-voids inside the concrete, but it only affects the RDM after the onset of the internal freeze-thaw damage, which has been discussed in Chapter 4.
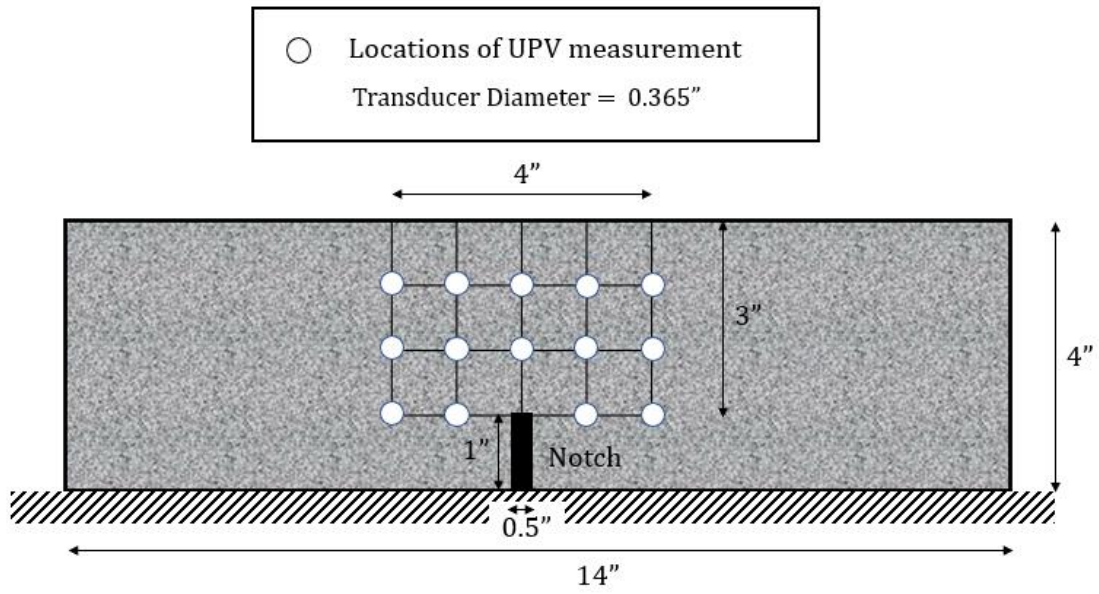
Figure 5-13. The locations of ultrasonic pulse velocity test measurement for the prismatic

specimen.
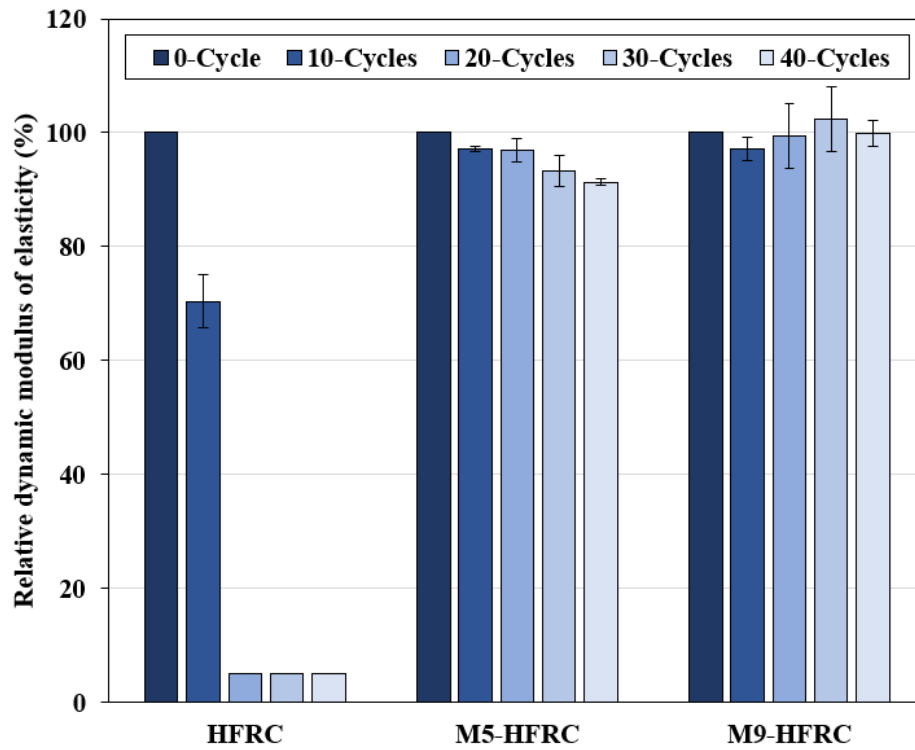
Figure 5-14. Influence of the freeze-thaw cycles on the relative dynamic modulus of the fiber-

reinforced concrete with distinct PCM contents, varying from 0, 5, to 9% by total volume.

5.3.2 Heterogeneous Damage in the Concrete after Freeze-thaw Weathering

To verify that the internal freeze-thaw damage development in the concrete can be heterogeneous, the ultrasonic pulse velocity (UPV) test is performed on the designated measurement points, as illustrated in Figure 5-13. It should be noted that since the most influential volume in a notched prismatic concrete beam for three-point bending test is in the vicinity of the notch tip, the volume of interests in detecting damage is a 4" by 2" projected area on the side of the beam, as shown in Figure 5-15. The contour on the beam shows the distribution of the dynamic modulus of elasticity (RDM) of the fiber-reinforced concrete at 0 cycles. The RDM is symmetric about the centerline and becomes lower as approaching to the notch tip.

To obtain the damage distribution on the projected area, the damage variables associated with the RDM are determined using Eq. (3-4) for the fiber-reinforced concrete specimens with distinct PCM dosages after 20 and 40 cycles of freezing and thawing. The damage variables for the fiber-reinforced concrete without phase change material (PCM) are determined after 10 cycles of thermal cycling since significant deterioration is observed. The measurement taken at such high damage level may cause unreliable testing results of the UPV method. The damage contour plots are constructed by the linear interpolation with the measurement data using MATLAB.

Figure 5-16 shows the damage contour of the fiber-reinforced concrete without PCM addition (HFRC) after 10 cycles of freezing and thawing. It can be observed that the damages are higher at the sides of the interest area because the temperature variation is more volatile at the side of a bulk material. Figure 5-17 through Figure 5-18 show the damage distributions of the fiber-reinforced concrete with a 5% PCM content (M5-HFRC) after 20 and 40 cycles. The results indicate that the damage is subtle for the M5-HFRC. The damage variables are in the range of 0 and 0.17, mostly observed at the sides of the beams. These values are much lower compared with

the damage variables of HFRC after 10 cycles of freezing and thawing. Figure 5-19 and Figure 5-20 display the damage distributions of the fiber-reinforced concrete with a 9% dosage of PCM (M9-HFRC) after 20 and 40 cycles. It can be observed that the damage level is reduced with increasing the dosage of PCM. This result indicates that adding PCM has a beneficial effect on the freeze-thaw damage mitigation, which is consistent to the findings in the analysis of mass loss and absorption capacity of concrete. Overall, the damage distribution contours have demonstrated that the freeze-thaw damage inside the concrete specimens can be heterogeneous, and the damage level is higher at the sides of the concrete beams.
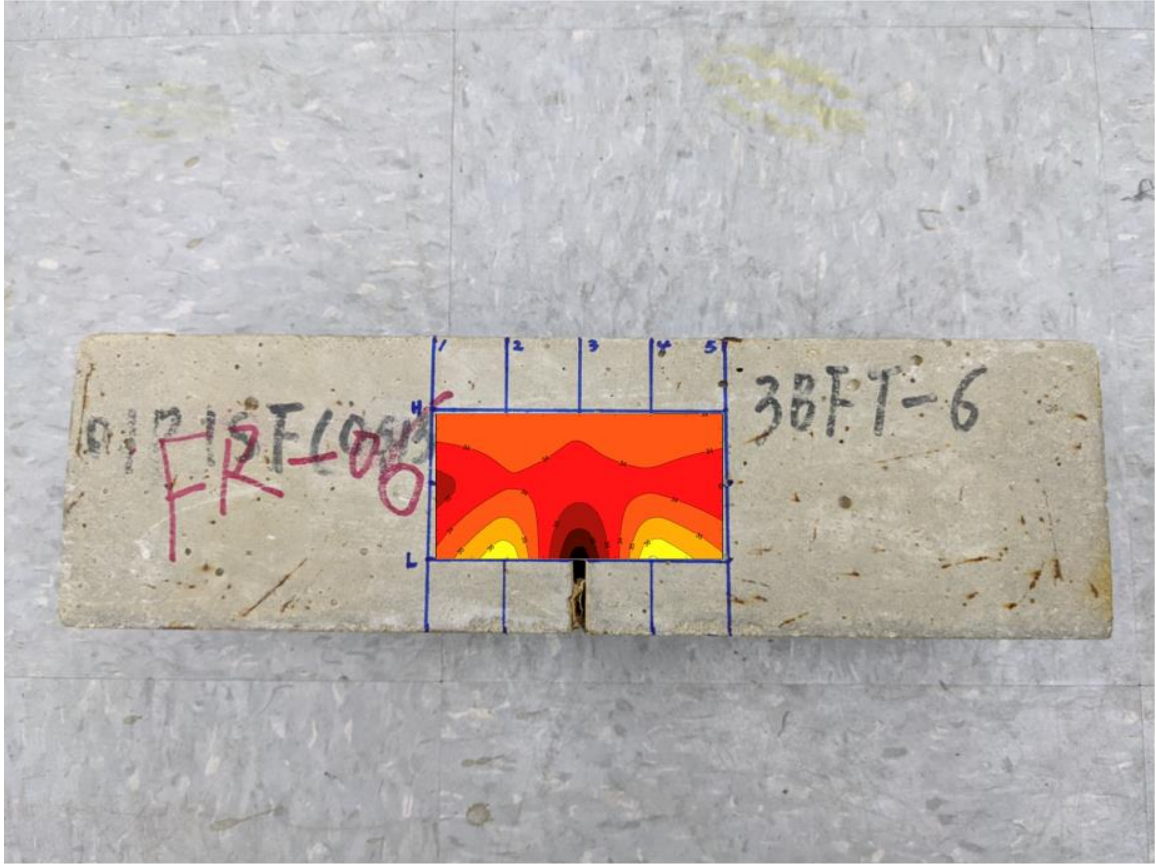
Figure 5-15. The area of interests in detecting the damage is a 5" by 3" rectangle on the side of
the beam specimen. The contour shows the distribution of dynamic modulus of elasticity for
illustration purpose.
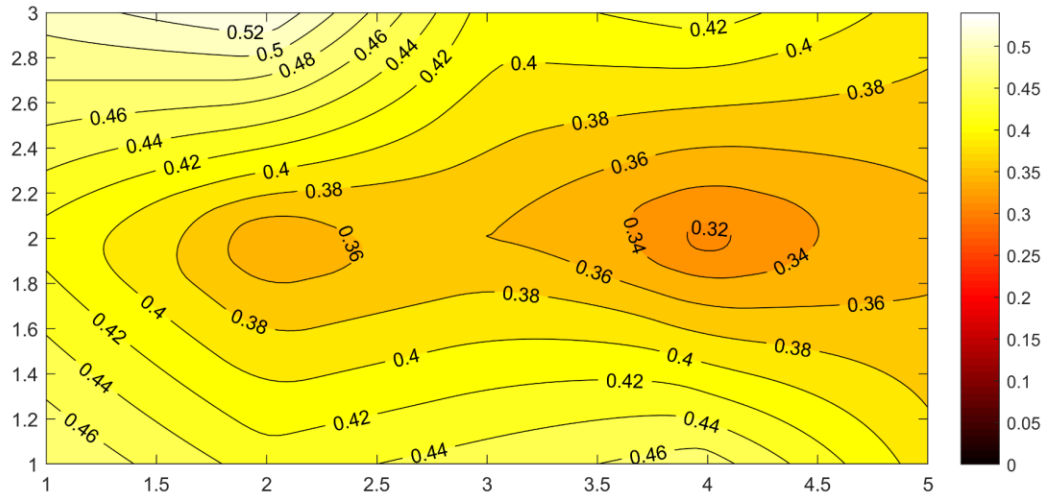
Figure 5-16. The damage contour measured at the 2" by 4" area near the notch tip for the fiber-reinforced concrete (HFRC) after 10 freeze-thaw cycles. The lighter color highlights the damaged area on the side of the beam.
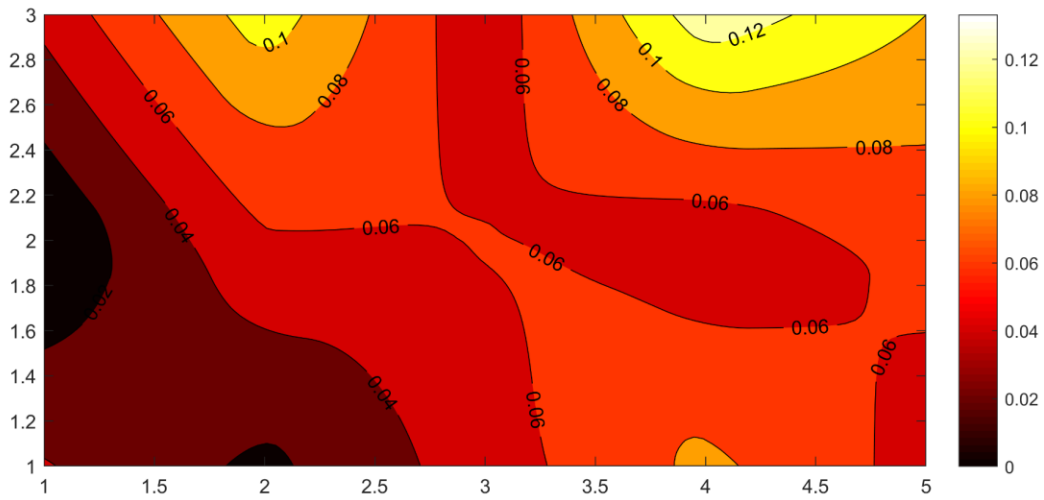
Figure 5-17. The damage contour measured at the 2" by 4" area near the notch tip for the fiber-reinforced concrete with a 5% PCM (M5-HFRC) after 20 freeze-thaw cycles. The lighter color highlights the damaged area on the side of the beam.
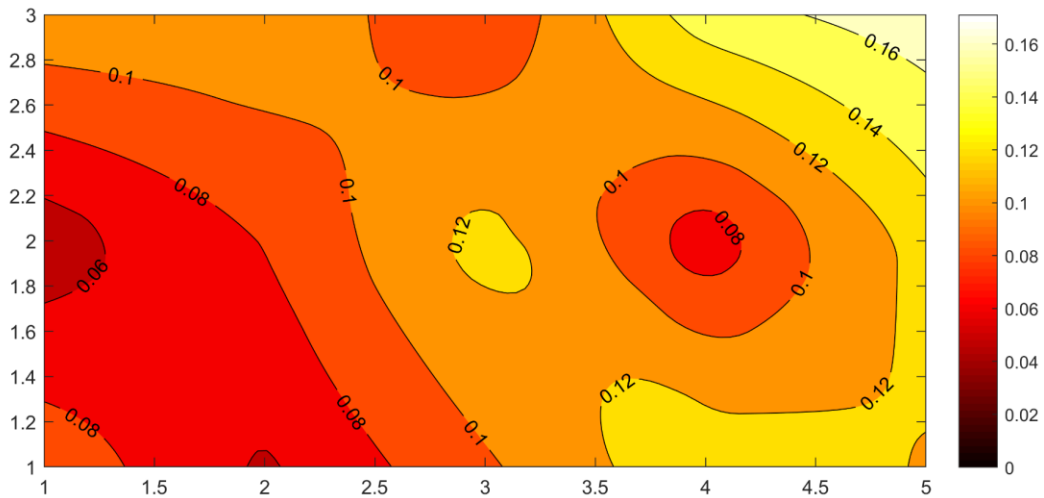
Figure 5-18. The damage contour measured at the 2" by 4" area near the notch tip for the fiber-reinforced concrete with a 5% PCM (M5-HFRC) after 40 freeze-thaw cycles. The lighter color highlights the damaged area on the side of the beam.
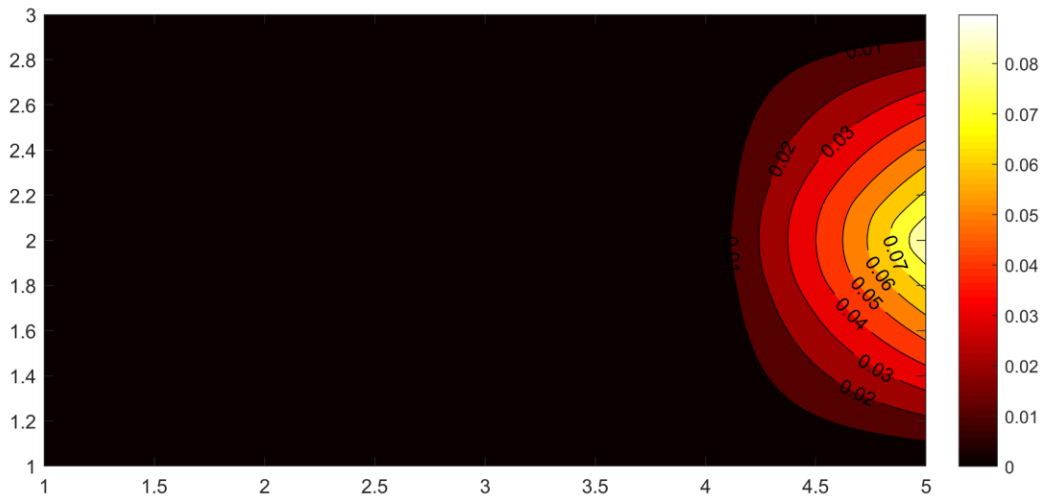
Figure 5-19. The damage contour measured at the 2" by 4" area near the notch tip for the fiber-reinforced concrete with a 9% PCM (M9-HFRC) after 20 freeze-thaw cycles. The lighter color highlights the damaged area on the side of the beam.
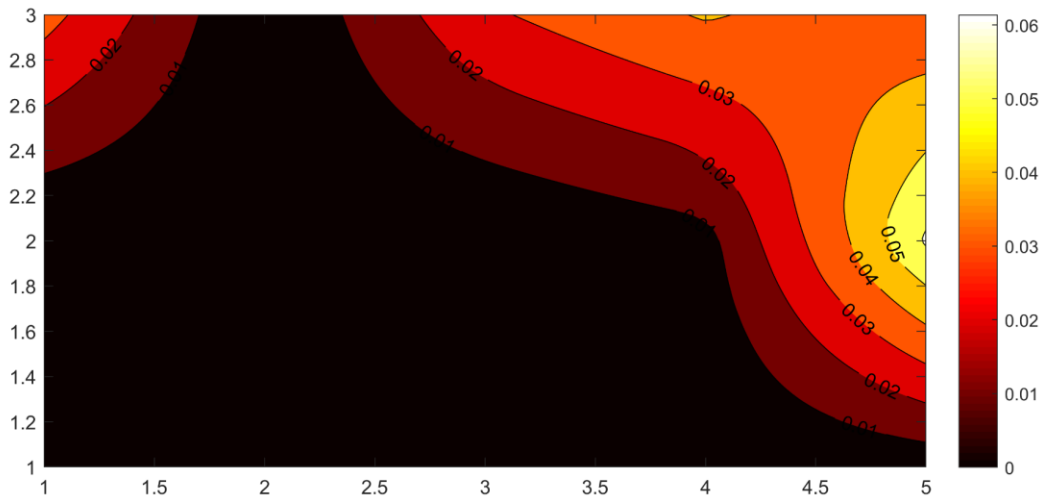
Figure 5-20. The damage contour measured at the 2" by 4" area near the notch tip for the fiber-reinforced concrete with a 9% PCM (M9-HFRC) after 40 freeze-thaw cycles. The lighter color highlights the damaged area on the side of the beam.

5.4 Three-point Bending Test Results

5.4.1 Fracture Energy and Peak Load Assessment

Table 5-1 shows the fracture energy, peak load, and the displacement at the peak load for the damaged and undamaged hybrid fiber-reinforced concrete specimens with PCM dosages varying from 0, 5 to 9%. In each composition, the three specimens labeled 08 to 10 are tested before the freeze-thaw cycles, except two specimens of the hybrid fiber-reinforced concrete (HFRC) are removed from the test program since undesired damage occurs for the beams during storage. The specimens labeled 05 to 07 are subjected to the freeze-thaw cycles with temperatures in the range of +22°C and -20°C before the three-point bending tests. After 10 cycles of thermal weathering, the HFRC specimens exhibit significant damage which is assessed with the ultrasonic pulse velocity test. Therefore, the HFRC specimens are tested with three-point bending after 10 cycles of freezing and thawing. The concrete specimens with 5 and 9% PCM dosages are subjected to 40 freeze-thaw cycles prior to the three-point bending test.

Figure 5-21 exhibits the averaged load-midspan displacement curves for the damaged and undamaged fiber-reinforced concrete with distinct PCM volume fractions. Table 5-2 shows the fracture energy, peak load, and the midspan displacement at the peak load obtained from the averaged load-midspan displacement curves. The fracture energy decreases with increasing PCM dosage or increasing the exposure to the thermal cycles. It can be observed that the undamaged hybrid fiber-reinforced concrete without PCM (FR in the figure) has the highest peak load. This result indicates the added steel fibers and polyvinyl alcohol fibers can substantially increase the flexural tensile strength of the concrete. In addition, the peak load of concrete decreases with the increasing volume fraction of PCM. It is noted that the HFRC (FR in the figure) curve has an

obvious inflection point after the peak load. The stage between the peak load and the inflection point can be characterized by the cracking of the harden cement paste subjected to tensile loading. After the inflection point, the behavior of the concrete represents the fiber debonding and the fiber pull-out process. Figure 5-22 through Figure 5-24 show the failure of the hybrid fiber-reinforced concrete without PCM specimens tested by the three-point bending. From these figures, the steel fibers are mostly pull out from the harden cement paste. The fracture of the steel fibers is not observed.

Table 5-1. Fracture energy, peak load, and the displacement at peak load for each prismatic concrete specimen. The specimens labeled 05 to 07 are subjected to the freeze-thaw cycles before the three-point bending tests.

Specimen	Fracture energy [N/mm]	Peak load [kN]	Displacement at peak load [mm]
5M05 (40FT)	5.564	8.545	1.845
5M06 40FT)	5.946	9.250	1.216
5M07 (40FT)	4.255	6.183	2.001
5M08	4.441	6.661	1.999
5M09	7.206	10.567	2.016
5M10	8.949	15.422	1.766
9M05 (40FT)	4.520	7.314	1.559
9M06 (40FT)	6.009	10.507	1.760
9M07 (40FT)	4.054	6.963	1.518
9M08	6.218	11.448	1.904
9M09	4.059	7.609	1.194
9M10	6.275	10.110	1.954
HFRC05 (10FT)	6.252	11.002	1.344
HFRC06 (10FT)	6.414	10.996	1.438
HFRC07 (10FT)	6.278	12.237	1.860
HFRC08	7.176	14.722	1.143
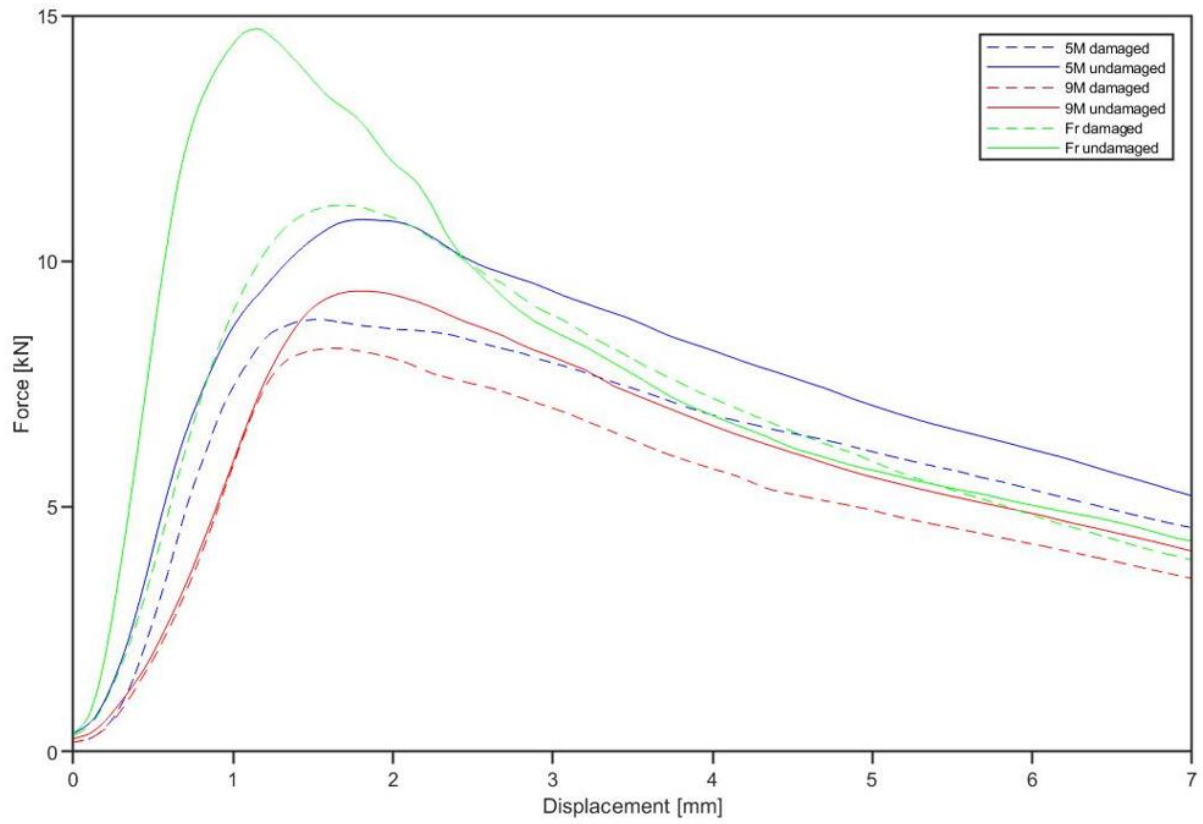
Figure 5-21. The averaged load-displacement curves for damaged and undamaged hybrid fiber-reinforced concrete with distinct volume fractions of PCM.

Table 5-2. The fracture energy, peak load, and the displacement at peak load obtained from average load-displacement curve for each concrete composition.

Specimen	Average fracture energy [N/mm]	SD	Average peak load* [kN]	SD	Average displacement at peak load [mm]	SD
5M Damaged	5.755	0.270	8.897	0.498	1.531	0.445
5M Undamaged	6.865	2.273	10.883	4.389	1.927	0.140
9M Damaged	4.861	1.021	8.262	1.953	1.612	0.130
9M Undamaged	5.517	1.263	9.722	1.949	1.684	0.425
HFRC Damaged	6.315	0.087	11.412	0.715	1.547	0.275
HFRC Undamaged	7.176	0	14.722	0	1.143	0
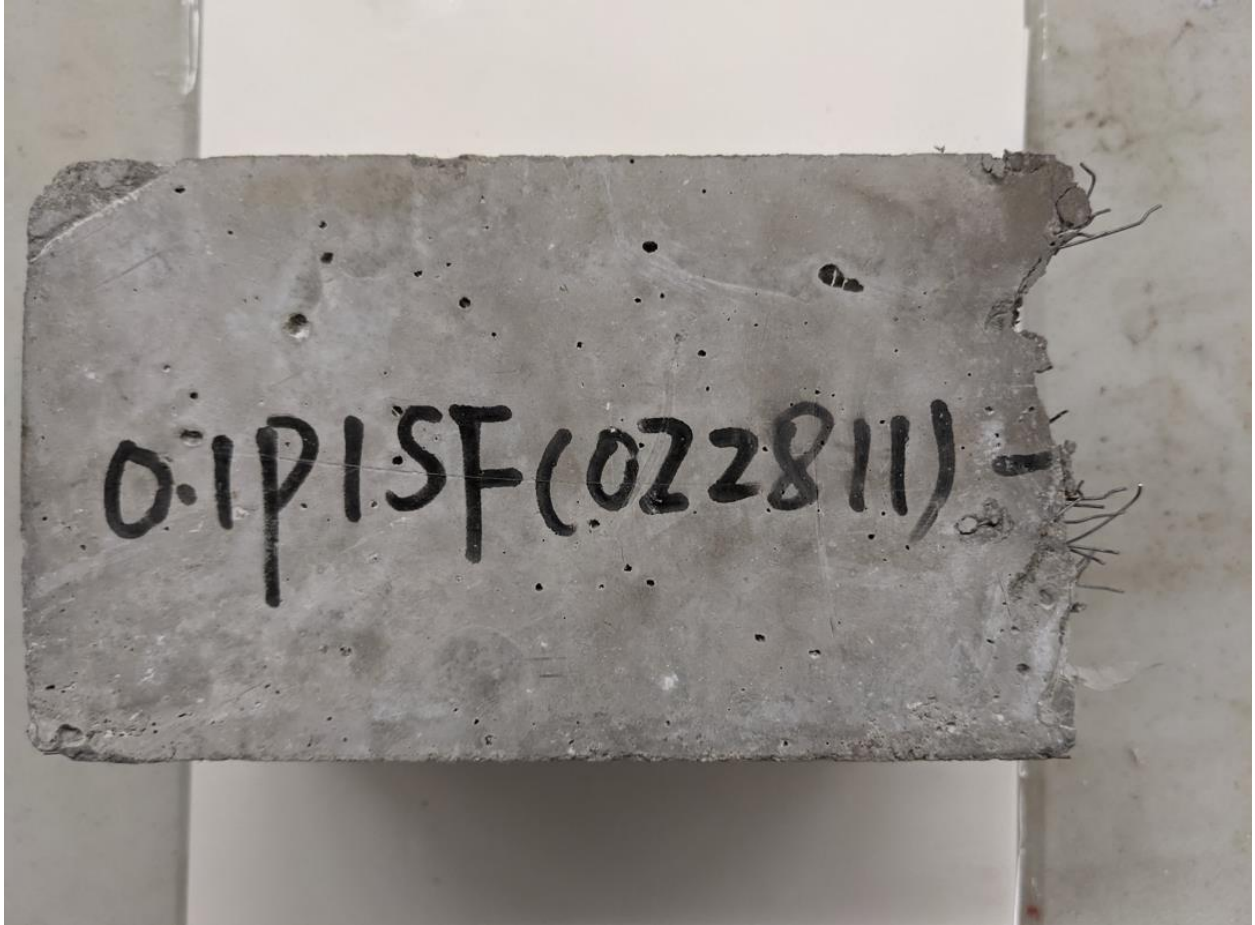
Figure 5-22. The failure of the fiber-reinforced concrete without PCM (HFRC) tested by three-

point bending.
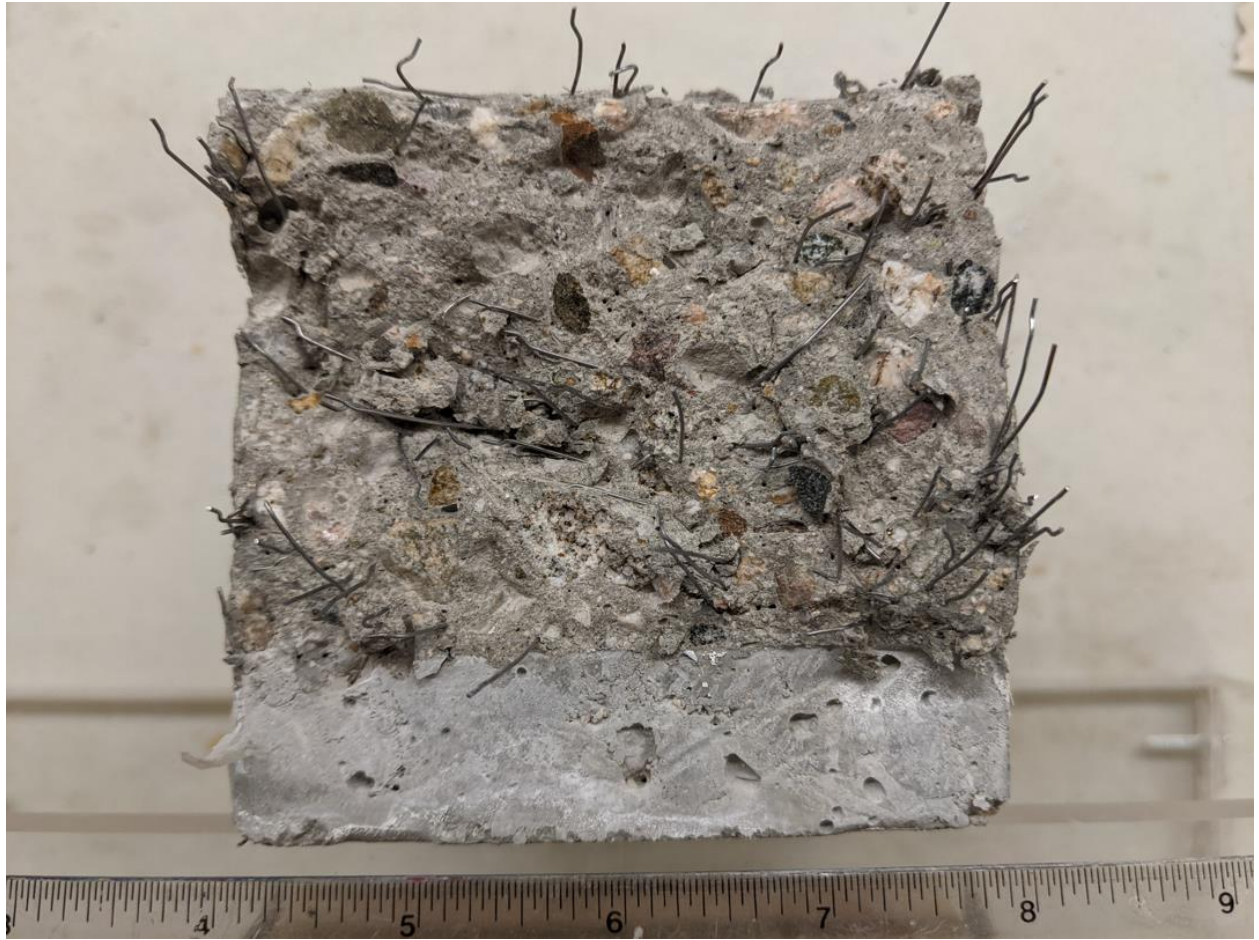
Figure 5-23. The section of failure of the fiber-reinforced concrete without PCM (HFRC) tested

by three-point bending.

Figure 5-24. The top view of failure of the fiber-reinforced concrete without PCM (HFRC) tested

by three-point bending.

5.4.2 Reinforcing Index and Flexural Behaviors of Concrete

The capability of fibers to enhance the flexural tensile behaviors of concrete is dependent on the aspect ratio, fiber content, the tensile strength of the fiber, and the dosage of the PCM addition. The fracture energy, the equivalent flexural tensile strength, and the residual flexural tensile strength are plotted against the proposed reinforcing index, calculated from Eq. (3-13) and Eq. (3-14). The reinforcing index is reduced with the increasing PCM dosage, since the PCM microcapsules would lead to the micro-voids between the fibers and the harden cement paste during the manufacturing process. This negative effect can be explained by the hydrophobic surfaces of the fibers and the shell of the PCM. The hybrid fiber-reinforced concrete without the addition of PCM (HFRC) has the highest reinforcing index of 2.16. The hybrid fiber-reinforced concrete with 5% and 9% PCM has a reinforcing index of 2.06 and 1.97, separately. Table 5-3 provides the displacements used to evaluate the equivalent flexural tensile strength and the residual flexural tensile strength.

Figure 5-25 shows the influences of the reinforcing index on the fracture energy. Figure 5-26 through Figure 5-28 exhibit the influences of the reinforcing index on the equivalent flexural tensile strength. Figure 5-29 through Figure 5-31 display the impacts of reinforcing index on the residual flexural tensile strength. It can be observed that the reinforcing index has a positive effect on the fracture energy, and the equivalent flexural tensile strength for the freeze-thaw damaged concrete and the undamaged concrete specimens. This indicates the addition of PCM into fiber-reinforced concrete would decrease the fracture energy and the equivalent tensile strength of the concrete. However, a positive effect of adding PCM can be seen in the relations between the reinforcing index and the residual flexural tensile strength. The PCM microcapsules can increase the packing density of the concrete, since the feature size of the PCM particles is much smaller

147

than the fine aggregates replaced in the concrete mixtures. The increased packing density may increase the resisting force during the fiber pull out process and therefore increases the residual flexural tensile strength for the concrete.

Table 5-3. The loads and displacements used to evaluate the equivalent flexural tensile strength and the residual flexural tensile strength.

Specimen	Peak load* [kN]	δp [mm]	Turning point load [kN]	δt [mm]	δt - δp	δe - δt
Damaged M5-HFRC	8.809	1.531	6.956	3.900	2.369	3.1
M5-HFRC	10.84	1.827	9.250	3.100	1.273	3.9
Damaged M9-HFRC	8.221	1.624	8.221	1.624	0	5.376
M9-HFRC	9.381	1.803	9.381	1.803	0	5.197
Damaged HFRC	11.129	1.643	7.349	3.900	2.257	3.1
HFRC	14.722	1.143	8.164	3.250	2.107	3.75
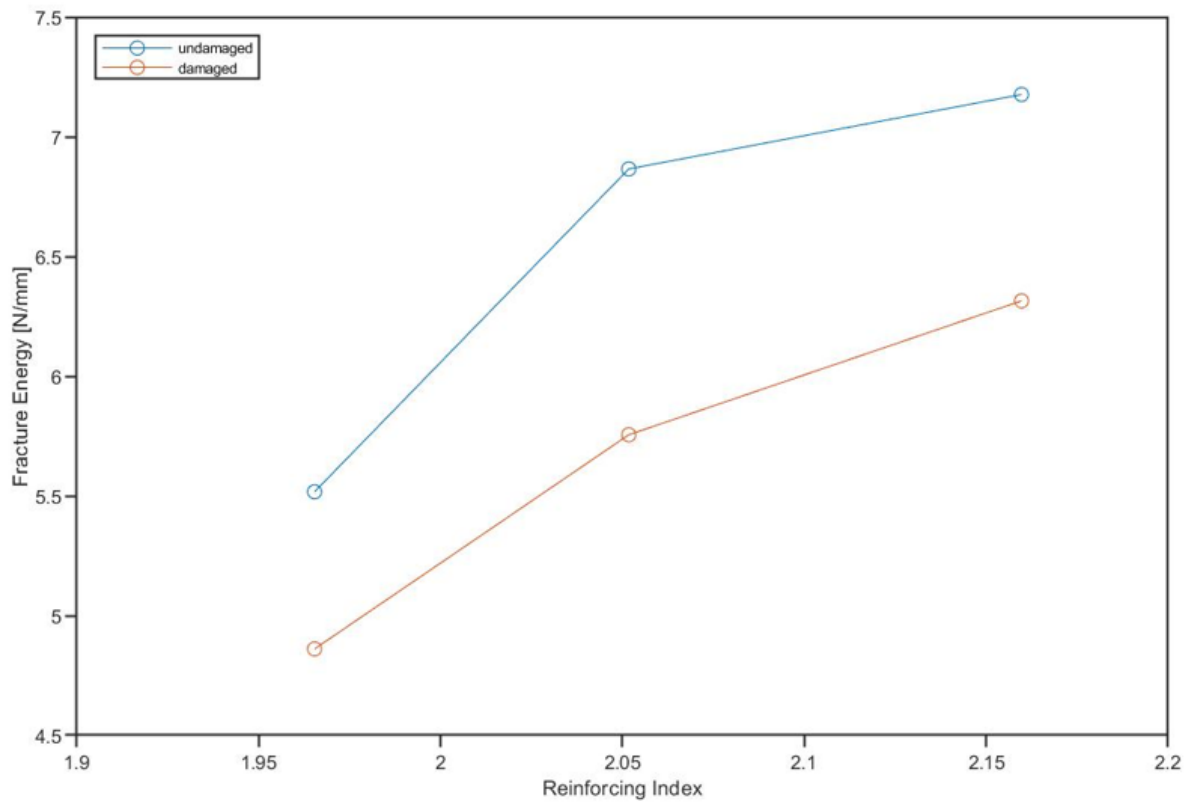
Figure 5-25. The relations between the fracture energy and the reinforcing index.
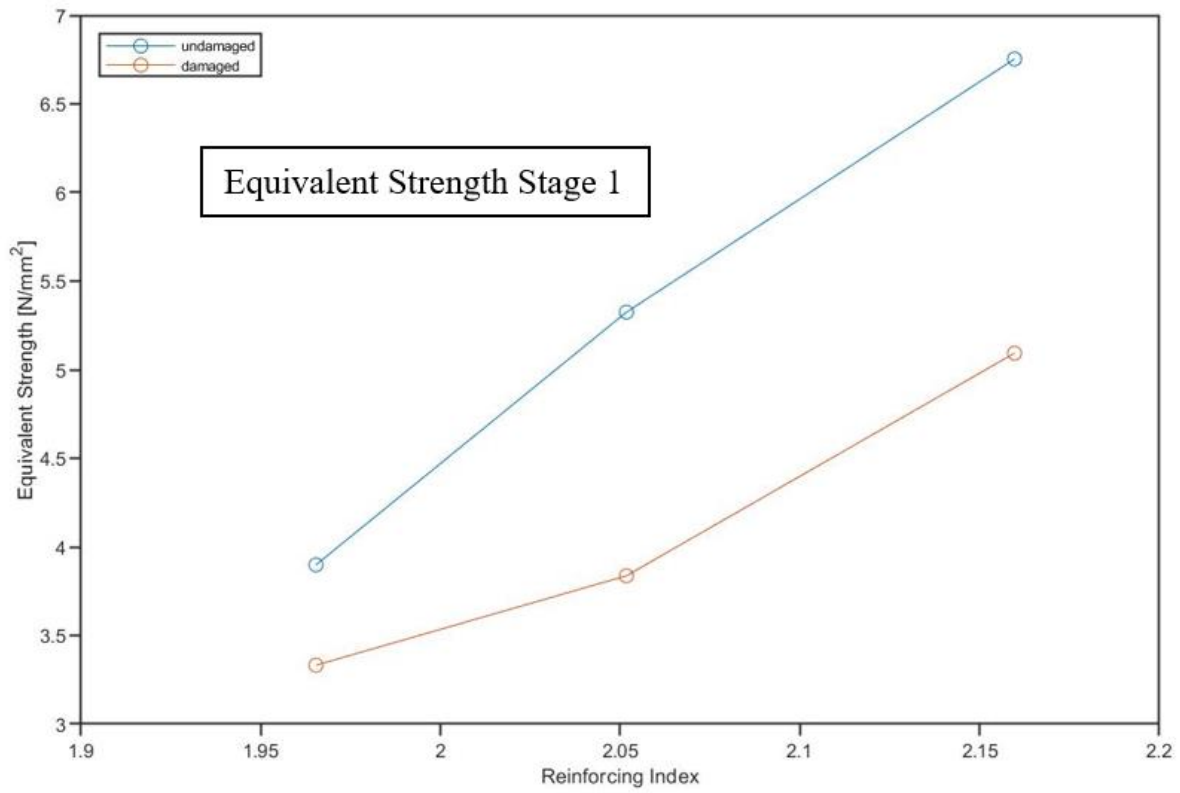
Figure 5-26. The relations between the equivalent flexural tensile strength up to the displacement
at the peak load, δp, and the reinforcing index.
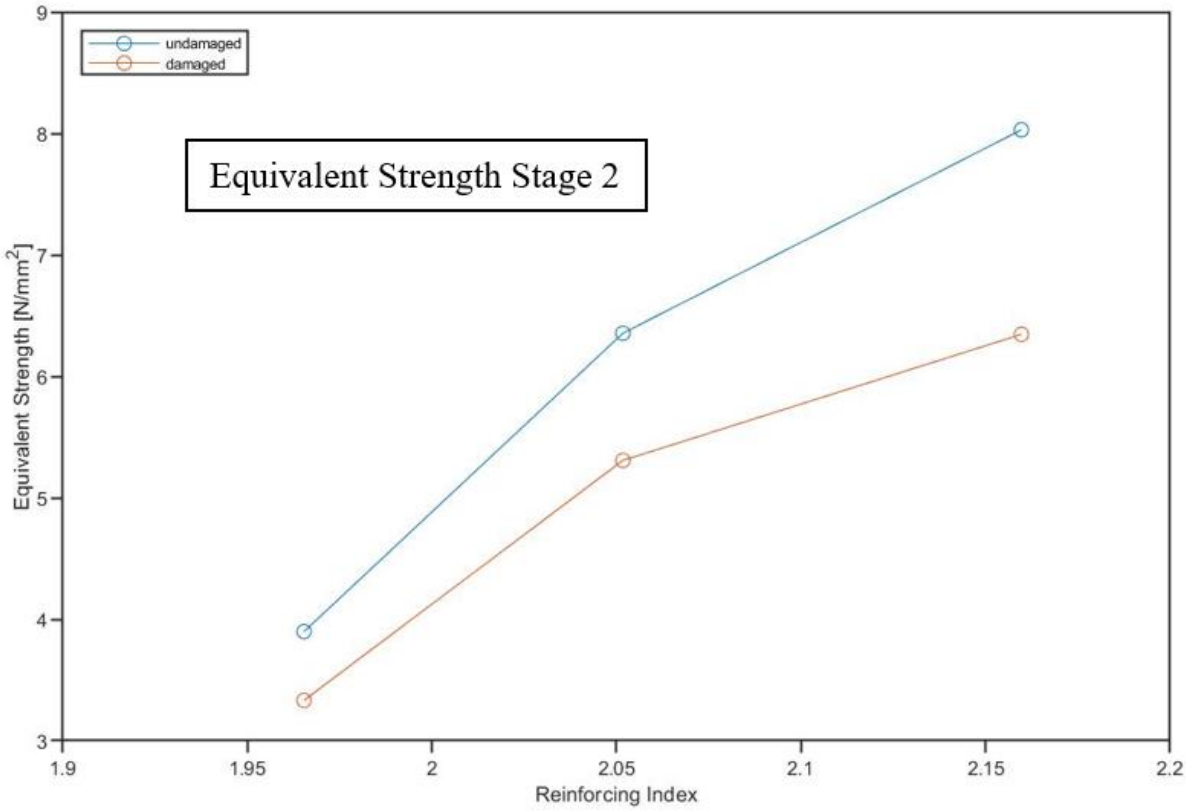
Figure 5-27. The relations between the equivalent flexural tensile strength up to the displacement at the turning point, δt, and reinforcing index at stage 2 displacement interval.
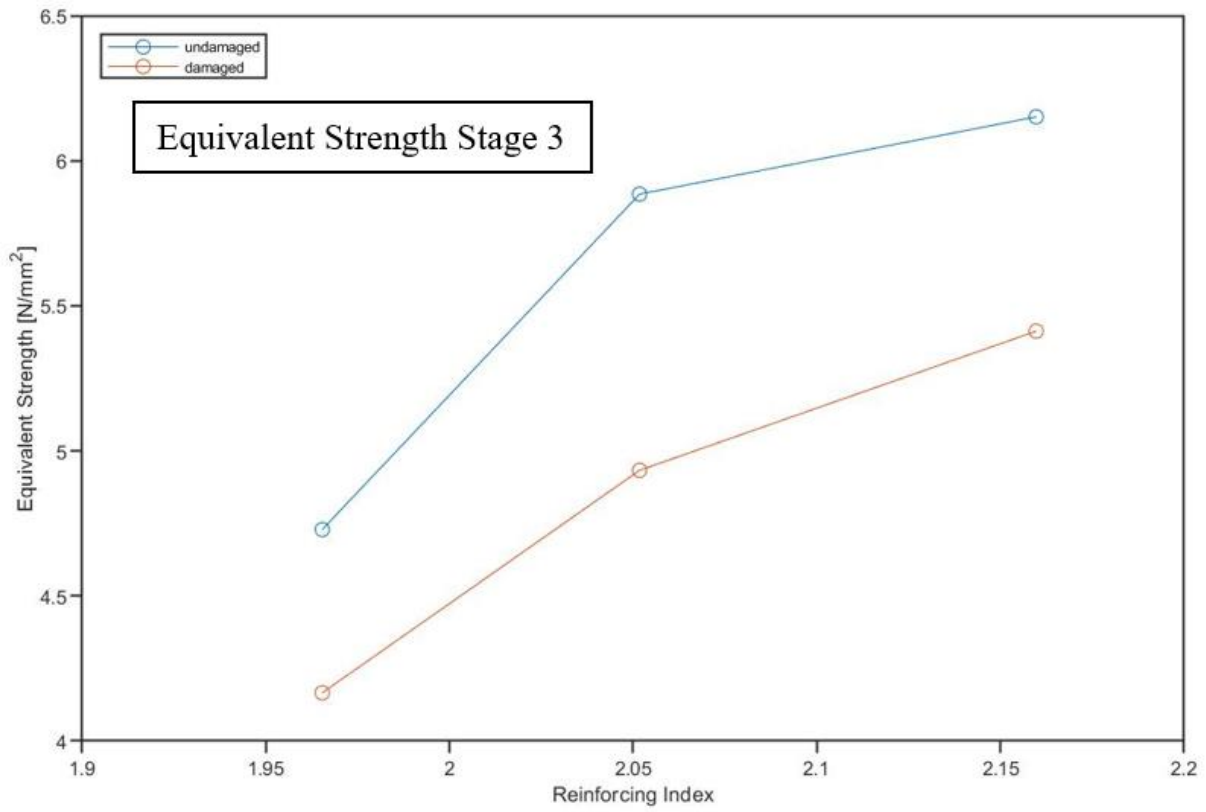
Figure 5-28.The relations between the equivalent flexural tensile strength up to the displacement

at the fracture, δe, and the reinforcing index.
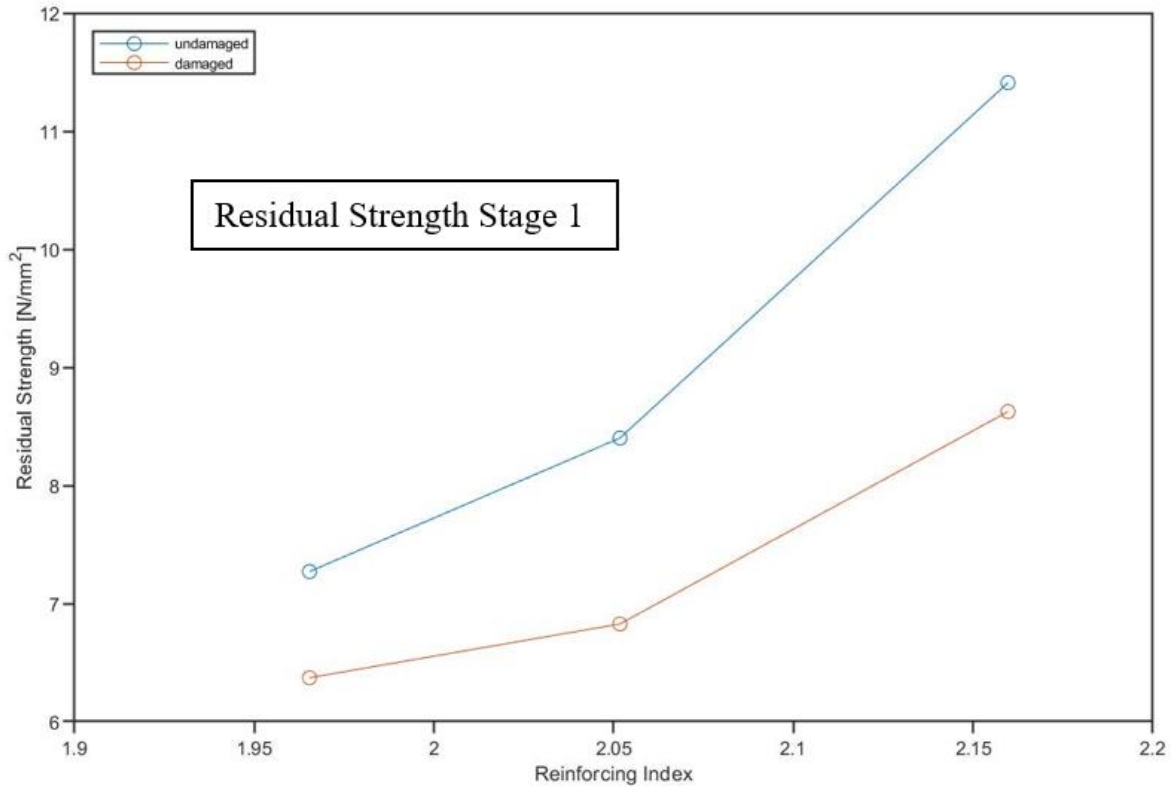
Figure 5-29. The relations between the residual flexural tensile strength at the displacement at

the peak load, δp, and reinforcing index.
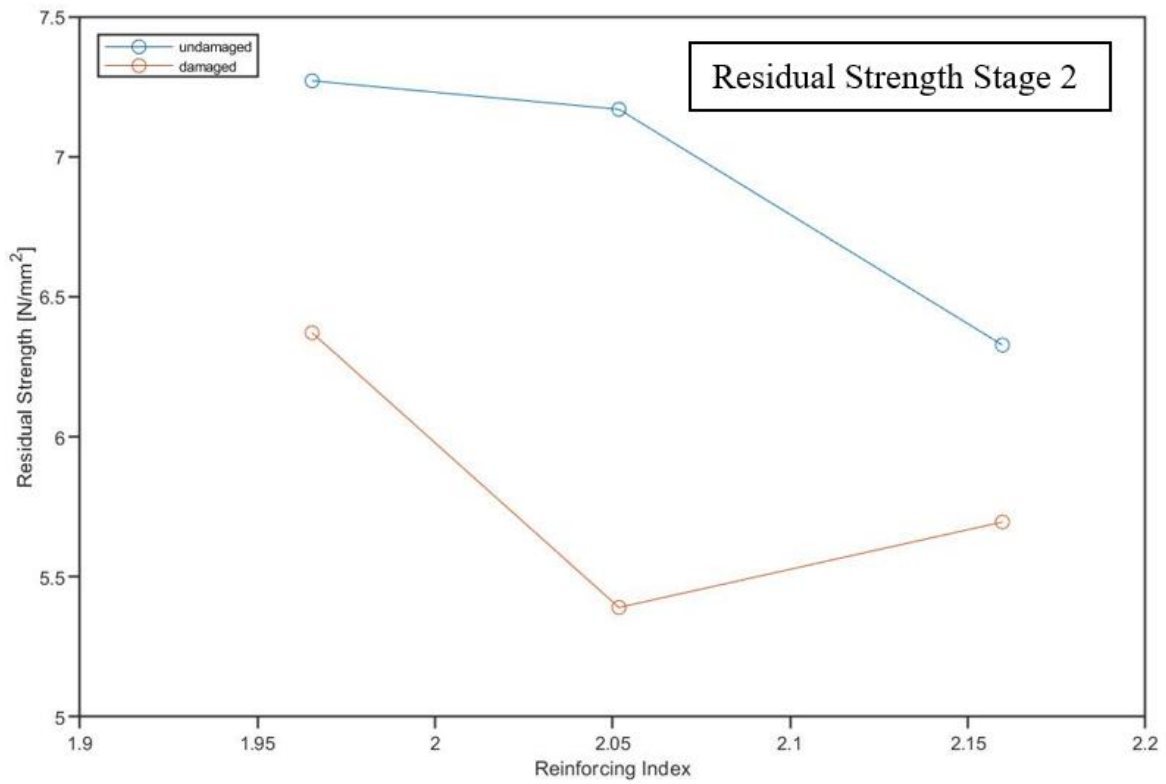
Figure 5-30. The relation between the residual flexural tensile strength at the displacement at the

turning point, δt, and the reinforcing index.
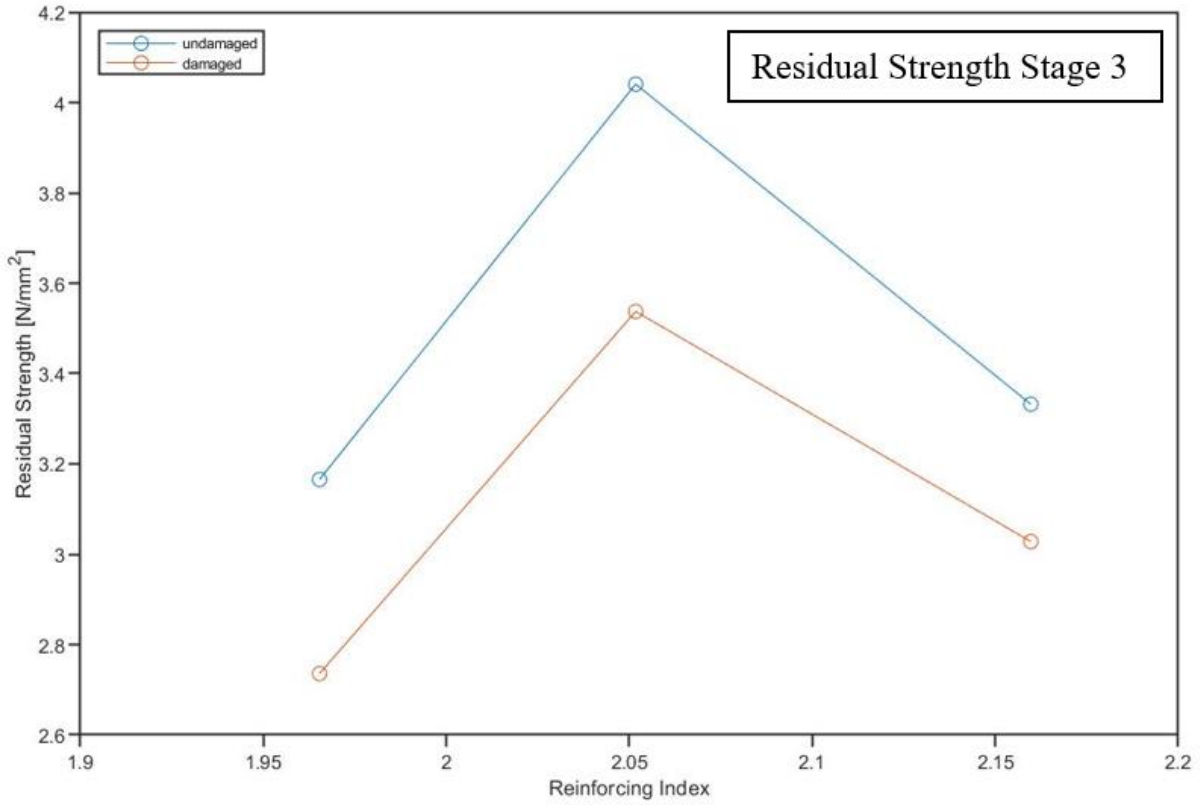
Figure 5-31. The relations between the residual flexural tensile strength at the displacement at

the fracture, δe, and the reinforcing index.

5.4.3 Digital Image Correlation Results

Figure 5-32 exhibits the parameters controlling the speckle pattern deployed on the concrete specimens. Figure 5-33 through Figure 5-35 show the crack development on the hybrid fiber-reinforced concrete with a 5% PCM dosage (5M06) during the three-point bending test. The crack initiation is from the edge of the notch since the beam may be internally damaged near the edge during the thermal cycling. Hence, the crack propagates through the path requiring the least energy and is stopped at the locations with steel or PVA micro-fibers.

Figure 5-36 through Figure 5-38 display the DIC displacements in the x-direction for the 5M06 beam. The color illustrates the magnitude and direction of the displacements on the surface of the beam. It can be seen that the DIC results can quantitatively describe the movement of the prismatic specimen under three-point bending. The accuracy of the DIC results is to be verified with the crack tip opening distance (CTOD) measured by the LVDT on the other surface of the beam.
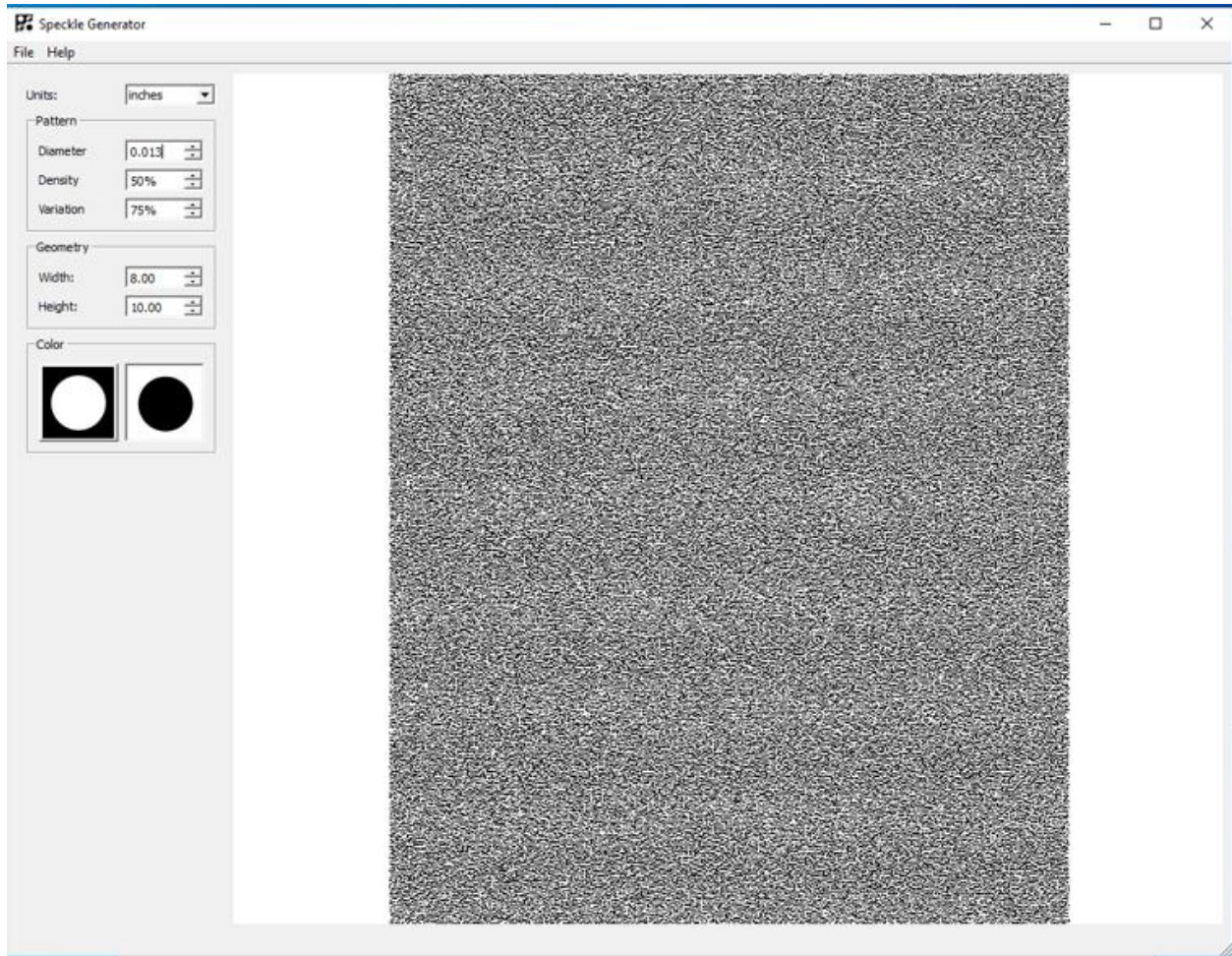
Figure 5-32. The DIC speckle pattern parameters.
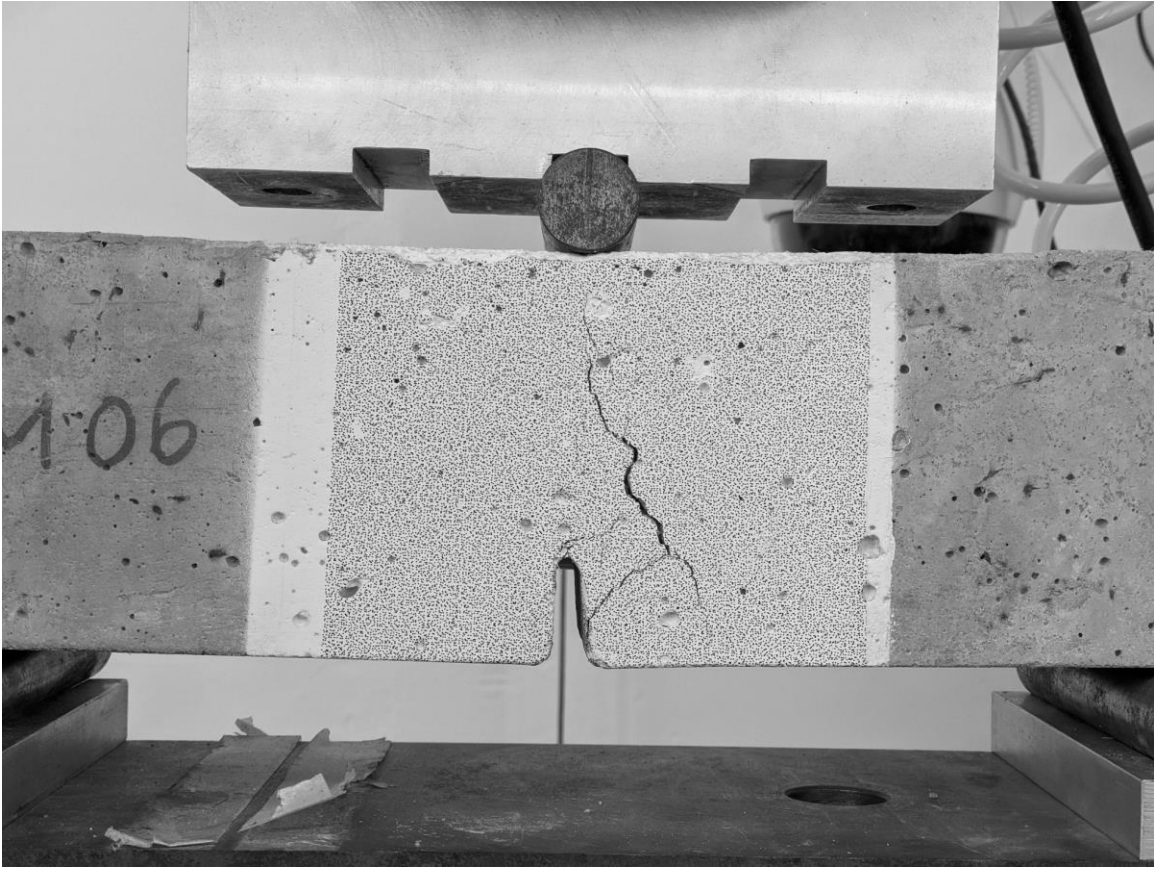
Figure 5-33. The crack initiation on the 5M06 beam.
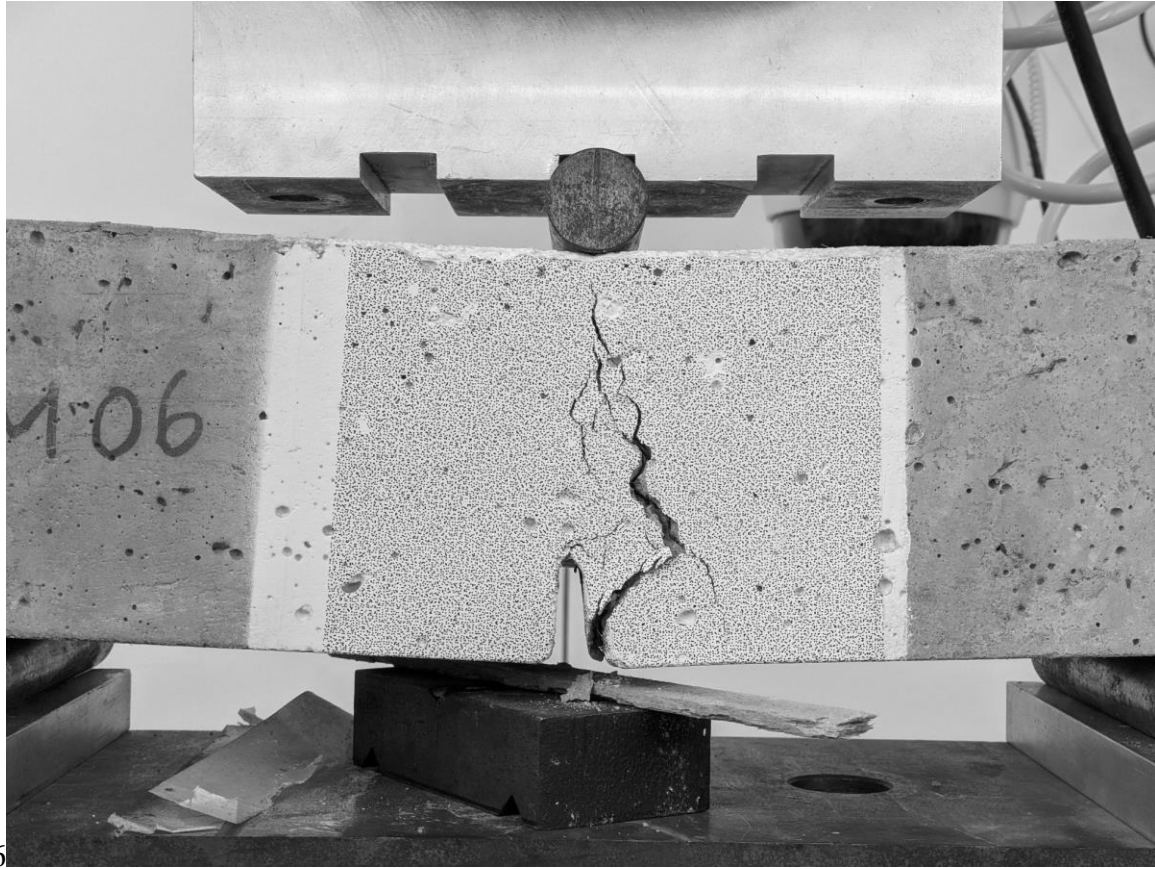
Figure 5-34. The crack propagation on the 5M06 beam.
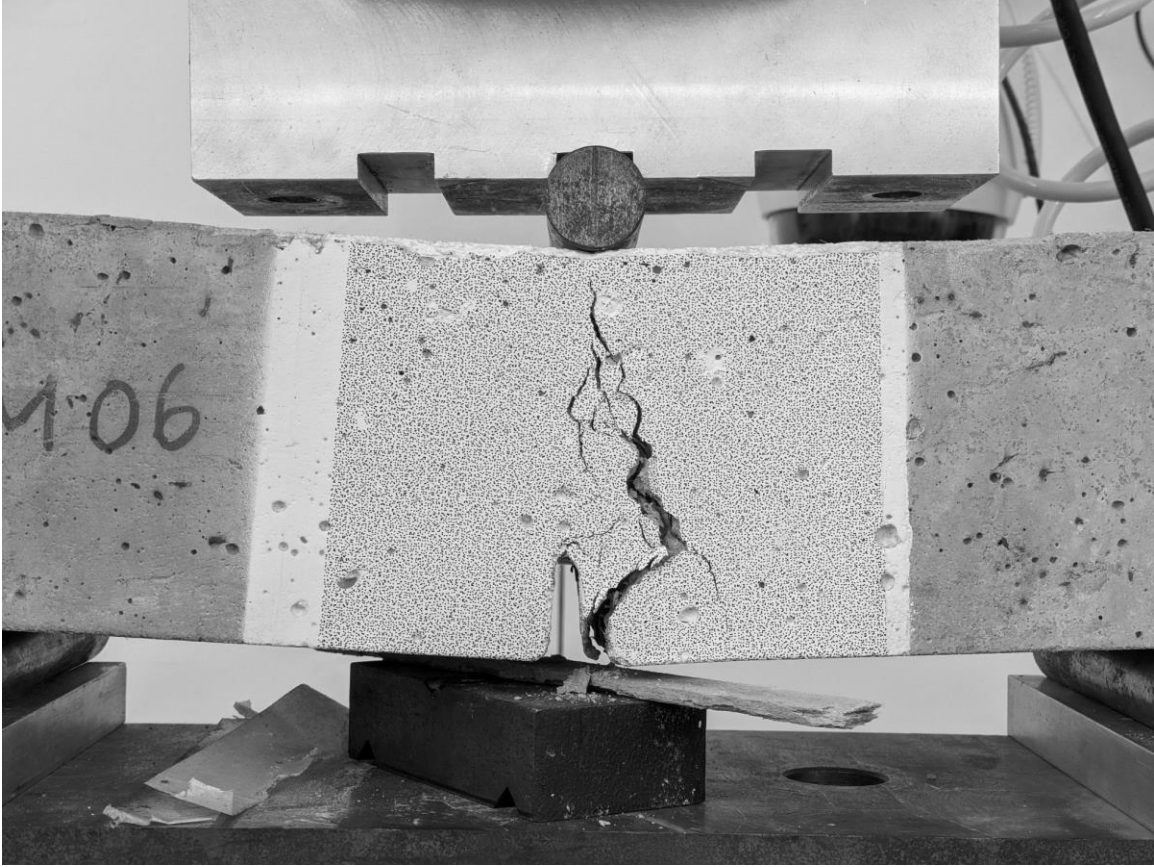
Figure 5-35. The end of three-point bending test on the 5M06 beam.
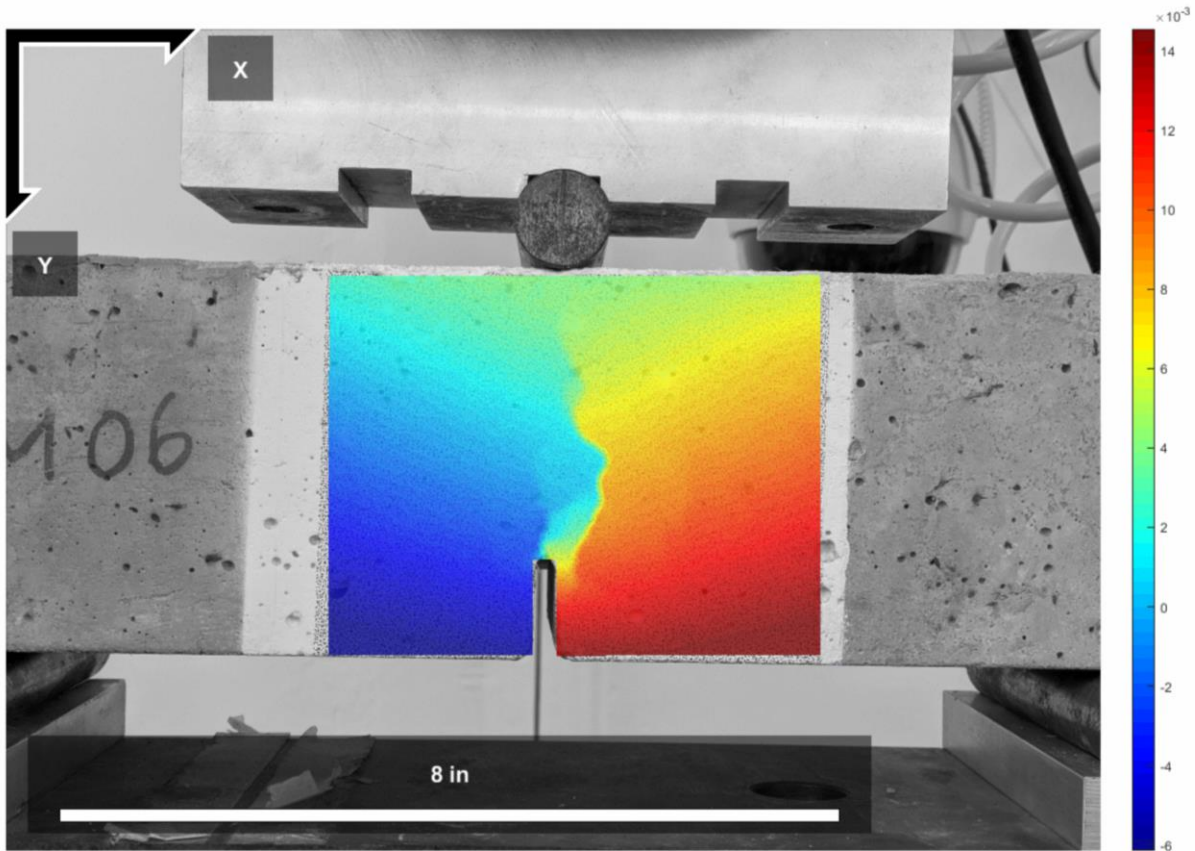
Figure 5-36. The DIC displacement in the x-direction at the crack initiation on the 5M06 beam.
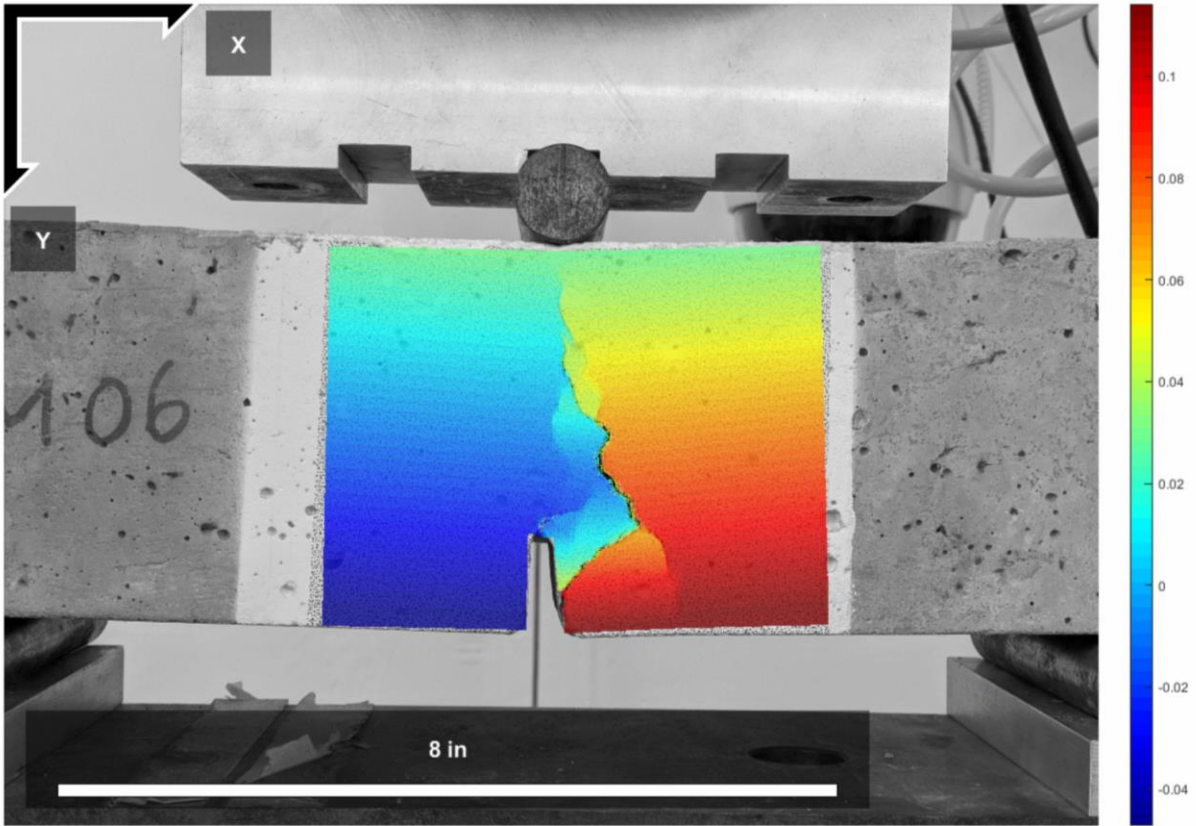
Figure 5-37. The DIC displacement in the x-direction at the crack propagation on the 5M06 beam.
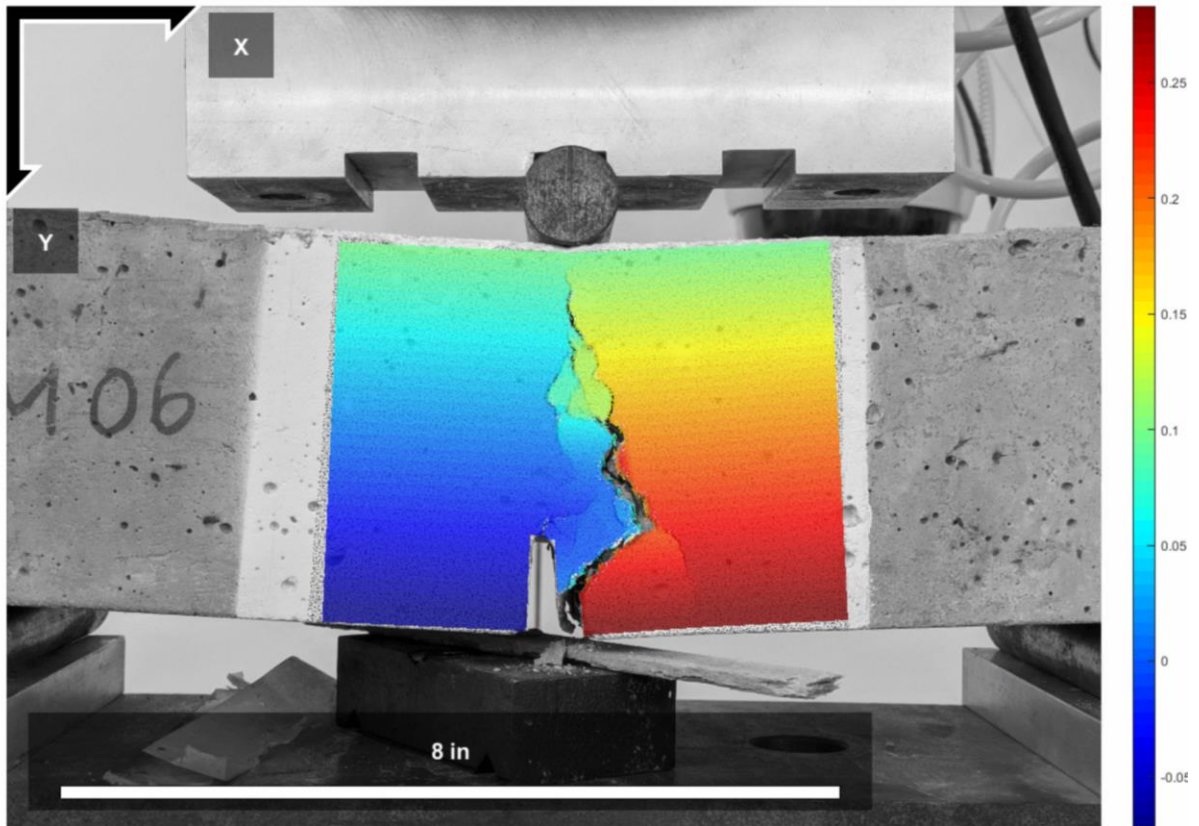
Figure 5-38. The DIC displacement in the x-direction at the end of three-point bending test on the 5M06 beam.

5.5 Concluding Remarks

The three-point bending test is performed on the hybrid-fiber-reinforced concrete with distinct volume fractions of PCM, varying from 0, 5, to 9%. The mass loss and the change in water absorption capacity are obtained for concrete subjected to freeze-thaw cycles. The focus has been put on the influences of adding PCM on post-peak behaviors of concrete. The most important findings are summarized as follows:

1) Since the freezing temperature is not as low as the setup in Chapter 4, the adverse effect of adding PCM on the freeze-thaw durability is not observed. This is also contributed by the increased PCM content in the concrete to provide sufficient heat energy upon freezing temperatures.

2) It has been verified that the freeze-thaw damage of concrete is heterogeneous using the UPV tests.

3) The flexural behaviors of concrete are considerably affected by the addition of PCM microcapsules. The fracture energy and the peak load are decreased with the increase of PCM content.

4) To study the effect of adding PCM on the post-peak behaviors of concrete under three-point bending loading, a new expression of reinforcing index is proposed with the consideration of PCM volume fraction.

5) The addition of PCM microcapsules may increase the packing density of the concrete and therefore increase the residual flexural tensile strength of the concrete.

Chapter 6 Temperature-Dependent Damage Model of

Hybrid Fiber-reinforced Concrete Containing Phase Change

Material

6.1 Quantification of Stress Exerted on Concrete at a Freezing Temperature

Considering an ice crystal in a pure water bath, the crystal is at equilibrium so that on the interface the crystal neither grows nor melts. The variation of the melting point of the crystal can be related to the crystal curvature by

$$T = T_m - \frac{\gamma_{cl} \, \kappa_{cl}}{\Delta S_{fv}} \qquad (6\text{-}1)$$

where T_m is the melting point of a large flat crystal, γ_{cl} is the specific energy of the crystal/liquid interface, κ_{cl} is the mean curvature of the interface, and ΔS_{fv} is the molar entropy of fusion per unit volume. Eq. (6-5) is usually called the **Gibbs-Thomson equation**. This equation indicates that a curved crystal has a greater depression in the melting point. The application of this equation can be useful in the explanation of crystallization site of concrete with a wide variety of pore size. In a cylindrical or spherical pore, if the temperature gradually decreases from the T_m, the ice is more likely to form at the wall rather than the center of the pore, considering the curvature is smaller at the wall and the melting temperature is closer to the T_m. Moreover, the water would solidify in larger pores first rather than smaller pores, because ice in the larger pores has higher melting point. As a result, the role of large pores, such as air voids, is to provide sites for first nucleation of ice. As the temperature decreases further, the ice crystal would penetrate the

connected smaller pores, such as capillaries, and exert stress of significant magnitude to break the wall of capillaries.

To estimate the stress that would generate over the wall of a tiny pore upon freezing temperature, a force equilibrium can be taken on the ice crystal. For a crystal in the capillary pore, it is reasonable to assume cylindrical sides and hemispherical ends of the crystal. Since the crystal is extremely small, there must be no thermal gradient on the crystal. At the hemispherical end and the cylindrical sides, the melting points can be calculated from Eq. (6-1). It is found that an additional pressure, P_A, must be applied to the cylindrical sides to reach equilibrium state. To verify this notion, considering the equilibrium condition for a crystal of ice merged in pure water as depicted in [21],

$$v_c \left(P_A + \gamma_{cl} \kappa_{cl} \right) = (v_l - v_c)(P_l - P_e) + (S_l - S_c)(T_m - T) \qquad (6\text{-}2)$$

where v_c is the molar volume of ice, P_A the additional pressure acting on the crystal, v_l the molar volume of water, P_l the water pressure, P_e the water vapor pressure, S_l the entropy of water, and S_c the entropy of ice.

At equilibrium state, there is no tendency either to form crystal nor liquid on the L/S interface. The right side of the equilibrium equation should be identical to any point at the end of ice crystal and at the side of ice crystal since they share the same water pressure and the thermal gradient in between is zero. Because of that, the following relation is arrived,

$$P_A + \gamma_{cl} \, \kappa_{cl}^S = \gamma_{cl} \, \kappa_{cl}^E \qquad (6\text{-}3)$$

$$P_A = \gamma_{cl} \left(\kappa_{cl}^E - \kappa_{cl}^S \right) \tag{6-4}$$

where κ_{cl}^E is the mean curvature at the end of the crystal and κ_{cl}^S is the mean curvature at the sides of the crystal.

6.2 Volume-Averaged Crystallization Pressure Exerted on the Concrete

To study the build-up stress acting on the concrete skeleton due to freezing events, the first step is to characterize the pore structure of concrete. However, it is computationally expensive to model the real pore system with the constituent materials of concrete. By contrast, a homogenization approach using micro-scale properties of concrete requires lower computational cost. Porosity, pore size distribution and connectivity are common micro-scale properties to determine the pore structure of concrete. In the study of freeze-thaw damage of concrete, these micro-scale properties were shown to have strong correlations to the macro-scale damage behaviors of concrete [56]–[58].

The method typically used, mercury intrusion <u>porosimetry</u> (MIP), can measure the total porosity and pore size distribution of concrete. This method employs an external pressurized chamber to force mercury into the pores on the surface of concrete. The general assumptions are that the pores are interconnected, and their sizes are not affected by the loss of water in the pores upon drying [59]. Figure 6-1 illustrates a cumulative pore size distribution curve that can be obtained by the MP technique. It should be emphasized that the measured pore size refers to breakthrough radius (also called percolated, threshold or critical radius in other articles), which represents the narrowest pores giving access to the pore network. The MIP technique, therefore, cannot provide a true pore size distribution. Moreover, this technique usually underestimates the actual porosity of concrete, since a portion of the pores can be either lake of connectivity to the major pore system or too small to be intruded by mercury.

The estimation of ice content in a porous media can be realized by knowing the cumulative pore size distribution, *V(r)*, and the temperature history of a freezing event. According to (6-1),

the breakthrough radius of freezing, which means at the thermodynamic equilibrium state the radius of the finest pore infiltrated by ice at current temperature T, can be expressed as:

$$r_f = \delta + \frac{\gamma_{CL}}{\Sigma_m (T_m - T)} \tag{6-5}$$

Considering the pore system is occupied by two phases, namely, water and ice, along with the facts that $V(0) = \phi_0$ and $V(\infty) = 0$, the averaged crystallization pressure can be expressed as:

$$\overline{P^A} = \frac{\int_{\infty}^{r_f} P^A \frac{dV}{dr} dr}{\int_{\infty}^{0} \frac{dV}{dr} dr} \tag{6-6}$$

where dV/dr is the volume fraction of the pores with size r, and P^A represents the crystallization pressure in a pore with radius r. In Figure 6-2, it is demonstrated that the volume-averaged stress exerted on concrete can be estimated by using Eq. (6-6) with a measured pore size distribution curve of the concrete.
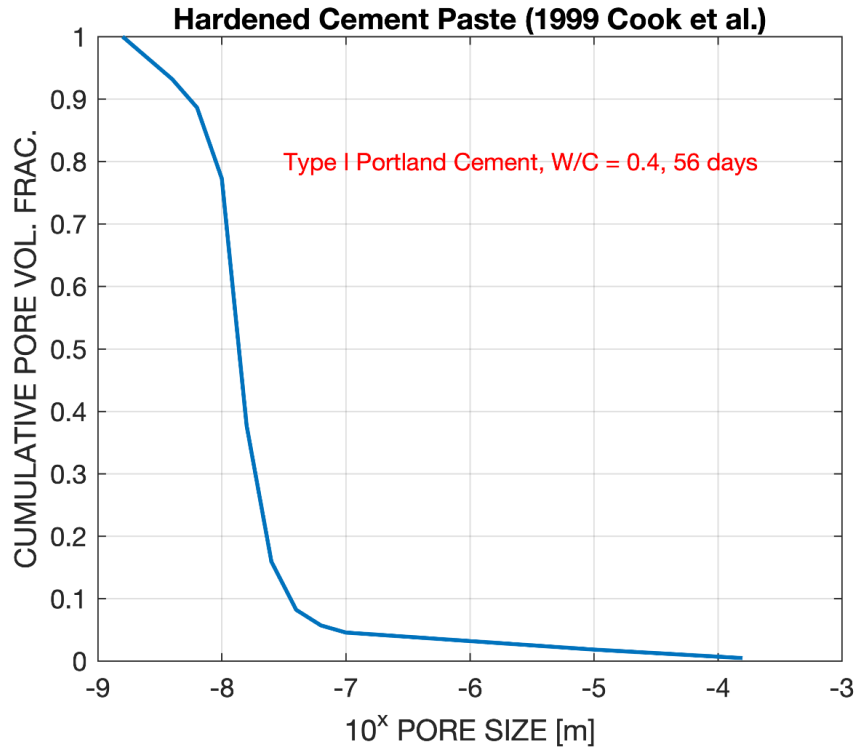
Figure 6-1. Cumulative pore size distribution curve adapted from [59]
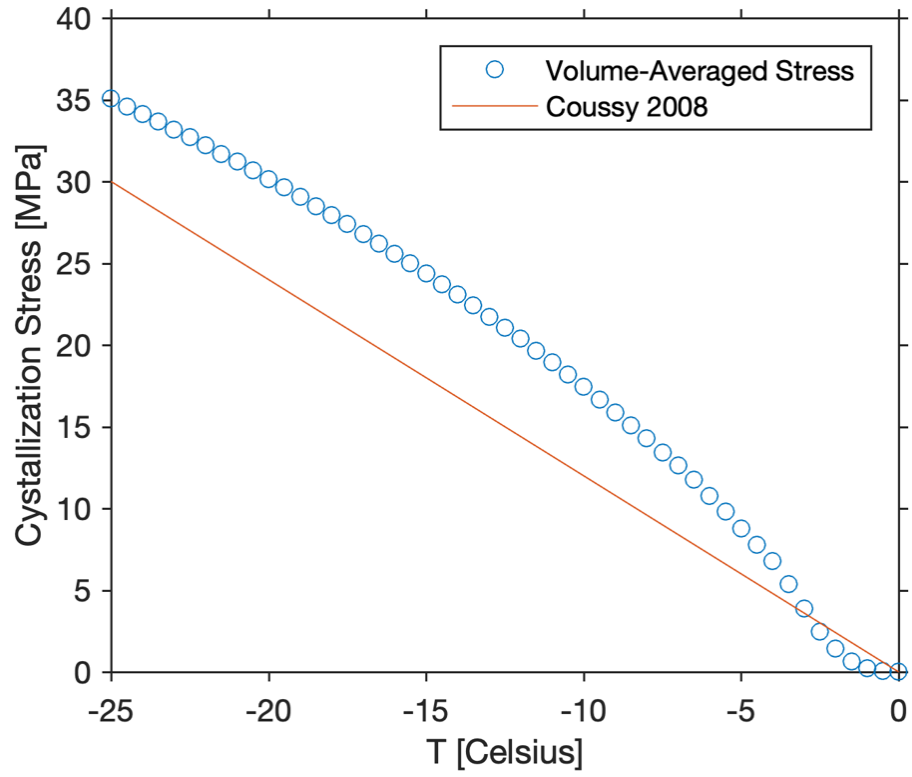
Figure 6-2. Volume-averaged crystallization pressure exerted on concrete at freezing temperatures.

6.3 Concluding Remarks

This chapter provides a volume-averaged methodology to estimate the stress exerted by ice crystal on the wall of concrete pore structure at a specific temperature below 0°C. The ice content in the pore structure can be estimated by Gibbs-Thomson equation. With the pore size distribution curves obtained from computed tomography or mercury intrusion porosimetry, the crystallization stress can be estimated by the averaged crystallization pressure expression. The change in stress at a specific temperature can then be used to define a damage variable to quantify the frost damage of the concrete.

Chapter 7 Conclusions and Future Work

7.1 Summary of innovations and key findings

This dissertation is developed to investigate the influence of phase change material (PCM) dosage on the freeze-thaw durability, compressive behaviors, and flexural behaviors of fiber-reinforced concrete. The surface damage and internal damage of concrete due to successive freeze-thaw cycles are systematically evaluated by freeze-thaw test, ultrasonic P-wave velocity test, uniaxial compression test, and three-point bending test.

1) An Arduino-based computer-automated freeze-thaw machine is custom designed to weather specimens with cylindrical shape. Freeze-thaw damage occurs on concrete specimens within 50 freeze-thaw cycles. This machine design and machine fabrication largely improve the reliability of the freeze-thaw test conducted by previous students, who tested the concrete for over 300 freeze-thaw cycles and observed no freeze-thaw damages in the concrete specimens.

2) The steel fibers and polyvinyl alcohol microfibers retain their individual capacities in the hybrid form.

3) The hybridization of fibers improves the compressive strength by approximately 30% compared with the plain concrete.

4) Based on the compression test results, the hybrid fiber reinforcement used in this study can provide a 40 MPa compressive strength at 28 days for the concrete with an 4.5% by volume of added PCM.

5) The hybridization of fibers improves the surface freeze-thaw durability of concrete subjected to 50 cycles of freeze-thaw action with the temperature range of -30°C to +20°C.

174

6) An adverse effect of adding PCM on the freeze-thaw durability of hybrid fiber-reinforced concrete is observed in the results of freeze-thaw test, ultrasonic pulse velocity test, and uniaxial compression test.

7) A damage model, considering the thermal buffering effect and the initial damage effect of adding PCM microcapsules, is developed for predicting the optimum PCM dosage in hybrid fiber-reinforced concrete. The confinements for the coefficients of this damage model are also derived.

8) A novel reinforcing index, considering the effect of adding PCM, is proposed and used in the characterization of flexural behaviors of the hybrid fiber-reinforced concrete with distinct PCM volume fractions under three-point bending tests.

7.2 Future work

The following research work should be pursued in the future,

1) For the derived damage model in Chapter 4, the effects of temperature and the number of freeze-thaw cycles are not independently shown as variables. To improve the damage model, a test program considering the freeze-thaw temperature and the number of freeze-thaw cycles as variables must be performed.

2) The size effect of the PCM microcapsules is not investigated in this study. As guided by micromechanics, the PCM in a different size can affect the compressive and flexural behaviors of concrete to a different extent.

3) The thermal performance of concrete with PCM microcapsules is indirectly evaluated by mechanical tests in this study. A transient thermal analysis using finite element modeling should be carried out to directly assess the thermal robustness of the PCM concrete. The homogenized thermal properties of the components and the measured specimen temperature and the ambient temperatures during the freeze-thaw tests should provide sufficient information for the study of temperature gradient in the PCM concrete.

Appendix I. Cycle-Based Tangent Moduli Tensor

In this section, the elastic-damage tangent modulus is revised to illustrate the stress-strain behavior of a concrete after hundreds of freezing and thawing actions. This attempt is an alternative to illustrate the damage evolution function through the idea that the deterioration of stiffness is directly linked to the numbers of freeze-thaw actions instead of the strain history. It is observed in experiments that the permanent strains developed on the surface of a concrete cylinder are functions of numbers of freeze-thaw actions [60], based on this observation we rewrite the damage evolution function and the damage criterion to account for the progressive increase of damage in the consideration of linear and nonlinear elasticity.

The damage evolution takes the form of

$$\dot{d} = \dot{N}H(N)$$

Here we assume the phenomenological function H is not dependent of d. In the permanent strains in axial and hook directions are measured and plotted versus the numbers of freeze-thaw cycles. The series A is air-entrained concrete and therefore there is no significant increments of plastic strains. Based on this figure we can write that the permanent strain, ϵ^d, is a function of numbers of freeze-thaw cycles, N.

$$\epsilon^d = M^{-1}(N)$$

$$N = M(\epsilon^d)$$

$$= \mathrm{M}(\epsilon - \epsilon^e)$$

Here we assume that M^{-1} is a monotonically increasing function so the inverse function M exists.

$$\dot{N} = \frac{\partial M}{\partial \epsilon} : \dot{\epsilon} + \frac{\partial M}{\partial \epsilon^e} : \dot{\epsilon}^e$$

In the next step we derive the relationship between stress rate and strain rate. To this end, taking the constitutive law of elasticity as the starting point,

$$\boldsymbol{\sigma} = \boldsymbol{C} : \boldsymbol{\epsilon}$$

$$\dot{\sigma} = \dot{C} : \epsilon + C : \dot{\epsilon}$$

In the case of isotropic damage, we can write

$$C = (1 - d)C^o$$

Therefore, we arrive at the elastic-damage tangent modulus as follows.

$$\dot{\sigma} = \left[(1 - d)C^o - H(N)C^o : \epsilon \otimes \frac{\partial M}{\partial \epsilon} \right] : \dot{\epsilon}$$
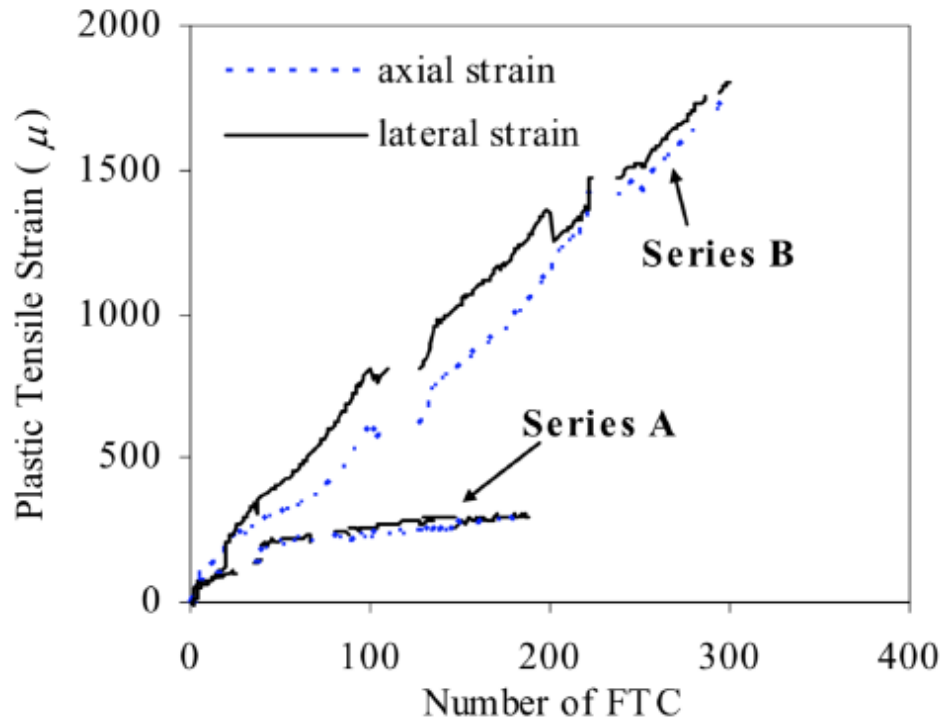
Figure A-1. The residual strain on the surface of concrete cylinder due to freeze-thaw actions.

Series A is the strain for the air-entrained concrete and Series B is the stain for the plain concrete

in [60]

References

[1]   N. Jackson and J. Puccinelli, "Long-Term Pavement Performance (LTPP) data analysis support: National pooled fund study TPF-5 (013)-effects of multiple freeze cycles and deep frost penetration on pavement performance and cost," FHWA-HRT-06-121, 2006.

[2]   J. J. Valenza and G. W. Scherer, "Mechanism for Salt Scaling," *J. Am. Ceram. Soc.*, vol. 89, no. 4, pp. 1161–1179, Apr. 2006, doi: 10.1111/j.1551-2916.2006.00913.x.

[3]   G. W. Scherer, "Crystallization in pores," *Cem. Concr. Res.*, vol. 29, no. 8, pp. 1347–1358, Aug. 1999, doi: 10.1016/S0008-8846(99)00002-2.

[4]   R. Baetens, B. P. Jelle, and A. Gustavsen, "Phase change materials for building applications: A state-of-the-art review," *Energy Build.*, vol. 42, no. 9, pp. 1361–1368, Sep. 2010, doi: 10.1016/j.enbuild.2010.03.026.

[5]   A. R. Sakulich and D. P. Bentz, "Increasing the Service Life of Bridge Decks by Incorporating Phase-Change Materials to Reduce Freeze-Thaw Cycles," *J. Mater. Civ. Eng.*, vol. 24, no. 8, pp. 1034–1042, Aug. 2012, doi: 10.1061/(ASCE)MT.1943-5533.0000381.

[6]   Y. Farnam, H. S. Esmaeeli, P. D. Zavattieri, J. Haddock, and J. Weiss, "Incorporating phase change materials in concrete pavement to melt snow and ice," *Cem. Concr. Compos.*, vol. 84, pp. 134–145, Nov. 2017, doi: 10.1016/j.cemconcomp.2017.09.002.

[7]   A. Jayalath *et al.*, "Properties of cementitious mortar and concrete containing micro-encapsulated phase change materials," *Constr. Build. Mater.*, vol. 120, pp. 408–417, Sep. 2016, doi: 10.1016/j.conbuildmat.2016.05.116.

[8]   S. Pilehvar *et al.*, "Effect of freeze-thaw cycles on the mechanical behavior of geopolymer concrete and Portland cement concrete containing micro-encapsulated phase change materials," *Constr. Build. Mater.*, vol. 200, pp. 94–103, Mar. 2019, doi: 10.1016/j.conbuildmat.2018.12.057.

[9]   M. C. Nataraja, N. Dhang, and A. P. Gupta, "Stress-strain curves for steel-fiber reinforced concrete under compression," p. 8, 1999.

[10]   Y. Zhang, J. W. Ju, H. Zhu, Q. Chen, Q. Guo, and Z. Yan, "A novel damage model based on micromechanics for hybrid fiber reinforced cementitious composites under uniaxial compression," *Int. J. Damage Mech.*, vol. 28, no. 7, pp. 1095–1132, Jul. 2019, doi: 10.1177/1056789518813270.

[11]   M. Moradi, A. R. Bagherieh, and M. R. Esfahani, "Constitutive modeling of steel fiber-reinforced concrete," *Int. J. Damage Mech.*, vol. 29, no. 3, pp. 388–412, Mar. 2020, doi: 10.1177/1056789519851159.

[12]   M. Şahmaran and V. C. Li, "De-icing salt scaling resistance of mechanically loaded engineered cementitious composites," *Cem. Concr. Res.*, vol. 37, no. 7, pp. 1035–1046, Jul. 2007, doi: 10.1016/j.cemconres.2007.04.001.

[13]   O. Karahan and C. D. Atiş, "The durability properties of polypropylene fiber reinforced fly ash concrete," *Mater. Des.*, vol. 32, no. 2, pp. 1044–1049, Feb. 2011, doi: 10.1016/j.matdes.2010.07.011.

[14]   I. Galan, A. Baldermann, W. Kusterle, M. Dietzel, and F. Mittermayr, "Durability of shotcrete for underground support– Review and update," *Constr. Build. Mater.*, vol. 202, pp. 465–493, Mar. 2019, doi: 10.1016/j.conbuildmat.2018.12.151.

[15] Z. Sun and G. W. Scherer, "Effect of air voids on salt scaling and internal freezing," *Cem. Concr. Res.*, vol. 40, no. 2, pp. 260–270, Feb. 2010, doi: 10.1016/j.cemconres.2009.09.027.

[16] M. Pigeon, J. Marchand, and R. Pleau, "Frost Resistant Concrete," *Constr. Build. Mater.*, vol. 10, no. 5, pp. 339–348, 1996.

[17] M. Pigeon and R. Pleau, *Durability of Concrete in Cold Climates.* 2011. Accessed: Aug. 28, 2021. [Online]. Available: http://public.ebookcentral.proquest.com/choice/publicfullrecord.aspx?p=487999

[18] O. Coussy, "Mechanics and Physics of Porous Solids," p. 297.

[19] D. H. Everett, "The thermodynamics of frost damage to porous solids," *Trans. Faraday Soc.*, vol. 57, p. 1541, 1961, doi: 10.1039/tf9615701541.

[20] J. J. Beaudoin and C. MacInnis, "The mechanism of frost damage in hardened cement paste," *Cem. Concr. Res.*, vol. 4, no. 2, pp. 139–147, Mar. 1974, doi: 10.1016/0008-8846(74)90128-8.

[21] G. W. Scherer, "Crystallization in pores," *Cem. Concr. Res.*, vol. 29, no. 8, pp. 1347–1358, Aug. 1999, doi: 10.1016/S0008-8846(99)00002-2.

[22] L. Petersen, L. Lohaus, and M. Polak, "Influence of Freezing-and-Thawing Damage on Behavior of Reinforced Concrete Elements," *ACI Mater. J.*, vol. 104, no. 4, 2007, doi: 10.14359/18826.

[23] K. Z. Hanjari, P. Utgenannt, and K. Lundgren, "Experimental study of the material and bond properties of frost-damaged concrete," *Cem. Concr. Res.*, vol. 41, no. 3, pp. 244–254, Mar. 2011, doi: 10.1016/j.cemconres.2010.11.007.

[24] L. Du and K. J. Folliard, "Mechanisms of air entrainment in concrete," *Cem. Concr. Res.*, vol. 35, no. 8, pp. 1463–1471, Aug. 2005, doi: 10.1016/j.cemconres.2004.07.026.

[25] P. K. Mehta and P. J. M. Monteiro, *Concrete: microstructure, properties, and materials*. New York: McGraw-Hill, 2006. Accessed: Nov. 29, 2021. [Online]. Available: http://www.dawsonera.com/depp/reader/protected/external/AbstractView/S9780071589192

[26] D. P. Bentz and R. Turpin, "Potential applications of phase change materials in concrete technology," *Cem. Concr. Compos.*, vol. 29, no. 7, pp. 527–532, Aug. 2007, doi: 10.1016/j.cemconcomp.2007.04.007.

[27] J. H. Yeon and K.-K. Kim, "Potential applications of phase change materials to mitigate freeze-thaw deteriorations in concrete pavement," *Constr. Build. Mater.*, vol. 177, pp. 202–209, Jul. 2018, doi: 10.1016/j.conbuildmat.2018.05.113.

[28] S. Nayak, N. M. A. Krishnan, and S. Das, "Microstructure-guided numerical simulation to evaluate the influence of phase change materials (PCMs) on the freeze-thaw response of concrete pavements," *Constr. Build. Mater.*, vol. 201, pp. 246–256, Mar. 2019, doi: 10.1016/j.conbuildmat.2018.12.199.

[29] B. Šavija and E. Schlangen, "Use of phase change materials (PCMs) to mitigate early age thermal cracking in concrete: Theoretical considerations," *Constr. Build. Mater.*, vol. 126, pp. 332–344, Nov. 2016, doi: 10.1016/j.conbuildmat.2016.09.046.

[30] Z. Wei *et al.*, "The durability of cementitious composites containing microencapsulated phase change materials," *Cem. Concr. Compos.*, vol. 81, pp. 66–76, Aug. 2017, doi: 10.1016/j.cemconcomp.2017.04.010.

[31] C. Norvell, D. J. Sailor, and P. Dusicka, "THE EFFECT OF MICROENCAPSULATED PHASE-CHANGE MATERIAL ON THE COMPRESSIVE STRENGTH OF STRUCTURAL CONCRETE," *J. Green Build.*, vol. 8, no. 3, pp. 116–124, Jul. 2013, doi: 10.3992/jgb.8.3.116.

[32] Y. Farnam *et al.*, "Evaluating the Use of Phase Change Materials in Concrete Pavement to Melt Ice and Snow," *J. Mater. Civ. Eng.*, vol. 28, no. 4, p. 04015161, Apr. 2016, doi: 10.1061/(ASCE)MT.1943-5533.0001439.

[33] P. S. Song and S. Hwang, "Mechanical properties of high-strength steel fiber-reinforced concrete," *Constr. Build. Mater.*, vol. 18, no. 9, pp. 669–673, Nov. 2004, doi: 10.1016/j.conbuildmat.2004.04.027.

[34] R. S. Olivito and F. A. Zuccarello, "An experimental study on the tensile strength of steel fiber reinforced concrete," *Compos. Part B Eng.*, vol. 41, no. 3, pp. 246–255, Apr. 2010, doi: 10.1016/j.compositesb.2009.12.003.

[35] W. Sun, Y. M. Zhang, H. D. Yan, and R. Mu, "Damage and damage resistance of high strength concrete under the action of load and freeze-thaw cycles," *Cem. Concr. Res.*, vol. 29, no. 9, pp. 1519–1523, Sep. 1999, doi: 10.1016/S0008-8846(99)00097-6.

[36] R. Mu, C. Miao, X. Luo, and W. Sun, "Interaction between loading, freeze–thaw cycles, and chloride salt attack of concrete with and without steel fiber reinforcement," *Cem. Concr. Res.*, vol. 32, no. 7, pp. 1061–1066, Jul. 2002, doi: 10.1016/S0008-8846(02)00746-9.

[37] D. Niu, L. Jiang, M. Bai, and Y. Miao, "Study of the performance of steel fiber reinforced concrete to water and salt freezing condition," *Mater. Des.*, vol. 44, pp. 267–273, Feb. 2013, doi: 10.1016/j.matdes.2012.07.074.

[38] P. Berkowski and M. Kosior-Kazberuk, "Effect of Fiber on the Concrete Resistance to Surface Scaling Due to Cyclic Freezing and Thawing," *Procedia Eng.*, vol. 111, pp. 121–127, 2015, doi: 10.1016/j.proeng.2015.07.065.

[39] A. Alsaif, S. A. Bernal, M. Guadagnini, and K. Pilakoutas, "Freeze-thaw resistance of steel fibre reinforced rubberised concrete," *Constr. Build. Mater.*, vol. 195, pp. 450–458, Jan. 2019, doi: 10.1016/j.conbuildmat.2018.11.103.

[40] C.-S. Chuang, "Hybrid Fiber Reinforced Concrete Incorporated With Phase Change Material," Doctoral dissertation, UCLA, 2015.

[41] Z. P. Bazant, J.-C. Chern, A. M. Rosenberg, and J. M. Gaidis, "Mathematical Model for Freeze-Thaw Durability of Concrete," *J. Am. Ceram. Soc.*, vol. 71, no. 9, pp. 776–783, Sep. 1988, doi: 10.1111/j.1151-2916.1988.tb06413.x.

[42] L. S. Weng, "On the investigation of the effects of grain size, damage, and exciting frequency upon P-wave characteristics in the ultrasonic NDE of concrete," Doctoral dissertation, University of California, Los Angeles, 2000.

[43] E. Ohdaira and N. Masuzawa, "Water content and its effect on ultrasound propagation in concrete — the possibility of NDE," *Ultrasonics*, vol. 38, no. 1–8, pp. 546–552, Mar. 2000, doi: 10.1016/S0041-624X(99)00158-4.

[44] S. Popovics, J. L. Rose, and J. S. Popovics, "THE BEHAVIOR OF ULTRASONIC PULSES IN CONCRETE," vol. 20, no. 2, p. 12, 1990.

[45] J. W. Ju and X. Lee, "Micromechanical Damage Models for Brittle Solids. Part I: Tensile Loadings," *J. Eng. Mech.*, vol. 117, no. 7, pp. 1495–1514, Jul. 1991, doi: 10.1061/(ASCE)0733-9399(1991)117:7(1495).

[46] Q. Luo, D. Liu, P. Qiao, Q. Feng, and L. Sun, "Microstructural damage characterization of concrete under freeze-thaw action," *Int. J. Damage Mech.*, vol. 27, no. 10, pp. 1551–1568, Nov. 2018, doi: 10.1177/1056789517736573.

[47] C. L. Nogueira, "Wavelet-based analysis of ultrasonic longitudinal and transverse pulses in cement-based materials," *Cem. Concr. Res.*, vol. 41, no. 11, pp. 1185–1195, Nov. 2011, doi: 10.1016/j.cemconres.2011.07.008.

[48] L. J. Malvar and G. E. Warren, "Fracture energy for three-point-bend tests on single-edge-notched beams," *Exp. Mech.*, vol. 28, no. 3, pp. 266–272, Sep. 1988, doi: 10.1007/BF02329022.

[49] T. Almusallam, S. M. Ibrahim, Y. Al-Salloum, A. Abadel, and H. Abbas, "Analytical and experimental investigations on the fracture behavior of hybrid fiber reinforced concrete," *Cem. Concr. Compos.*, vol. 74, pp. 201–217, Nov. 2016, doi: 10.1016/j.cemconcomp.2016.10.002.

[50] J. Blaber, B. Adair, and A. Antoniou, "Ncorr: Open-Source 2D Digital Image Correlation Matlab Software," *Exp. Mech.*, vol. 55, no. 6, pp. 1105–1122, Jul. 2015, doi: 10.1007/s11340-015-0009-1.

[51] A. Çavdar, "Investigation of freeze–thaw effects on mechanical properties of fiber reinforced cement mortars," *Compos. Part B Eng.*, vol. 58, pp. 463–472, Mar. 2014, doi: 10.1016/j.compositesb.2013.11.013.

[52] M. Hunger, A. G. Entrop, I. Mandilaras, H. J. H. Brouwers, and M. Founti, "The behavior of self-compacting concrete containing micro-encapsulated Phase Change Materials," *Cem.*

Concr. Compos., vol. 31, no. 10, pp. 731–743, Nov. 2009, doi: 10.1016/j.cemconcomp.2009.08.002.

[53] M. Pigeon, C. Talbot, J. Marchand, and H. Hornain, "Surface microstructure and scaling resistance of concrete," *Cem. Concr. Res.*, vol. 26, no. 10, pp. 1555–1566, Oct. 1996, doi: 10.1016/0008-8846(96)00138-X.

[54] M. J. Setzer, R. Auberg, S. Kasparek, S. Palecki, and P. Heine, "CIF-Test-Capillary suction, internal damage and freeze thaw test: Reference method and alternative methods A and B," *Mater. Struct.*, vol. 34, no. 9, pp. 515–525, Nov. 2001, doi: 10.1007/BF02482179.

[55] E. Gürbüz and S. Erdem, "Development and thermo-mechanical analysis of high-performance hybrid fibre engineered cementitious composites with microencapsulated phase change materials," *Constr. Build. Mater.*, vol. 263, p. 120139, Dec. 2020, doi: 10.1016/j.conbuildmat.2020.120139.

[56] R. Kumar and B. Bhattacharjee, "Porosity, pore size distribution and in situ strength of concrete," *Cem. Concr. Res.*, vol. 33, no. 1, pp. 155–164, Jan. 2003, doi: 10.1016/S0008-8846(02)00942-0.

[57] T. C. Powers, "Structure and Physical Properties of Hardened Portland Cement Paste," *J. Am. Ceram. Soc.*, vol. 41, no. 1, pp. 1–6, Jan. 1958, doi: 10.1111/j.1151-2916.1958.tb13494.x.

[58] I. O. Yaman, N. Hearn, and H. M. Aktan, "Active and non-active porosity in concrete Part I: Experimental evidence," *Mater. Struct.*, vol. 35, no. 2, pp. 102–109, Mar. 2002, doi: 10.1007/BF02482109.

[59] R. A. Cook and K. C. Hover, "Mercury porosimetry of hardened cement pastes," *Cem. Concr. Res.*, vol. 29, no. 6, pp. 933–943, Jun. 1999, doi: 10.1016/S0008-8846(99)00083-6.

[60] M. Hasan, H. Okuyama, Y. Sato, and T. Ueda, "Stress-Strain Model of Concrete Damaged by Freezing and Thawing Cycles," *J. Adv. Concr. Technol.*, vol. 2, no. 1, pp. 89–99, 2004, doi: 10.3151/jact.2.89.